

Effect of Field Bending and Girth Weld on the Initiation and Early Growth of Near-Neutral pH Circumferential Stress Corrosion Cracking (NNpHCSCC) in Thin-walled Pipeline

by

Hiroyuki Tanaka

A thesis submitted in partial fulfillment of the requirements for the degree of

Master of Science

in

Materials Engineering

Department of Chemical and Materials Engineering

University of Alberta

© Hiroyuki Tanaka, 2023

Abstract

Pipeline failure because of near-neutral pH stress corrosion cracking (NNpHSCC) has been a concern in Canada for over 30 years. Previous studies focused on axial NNpHSCC, which has happened more frequently than circumferential NNpHSCC (C-NNpHSCC). This study focuses on the significance of residual stress caused by the combination of girth weld and field bending on initiation and early-stage growth of C-NNpHSCC. To examine the effect of those factors, corrosion samples with and without girth welds were manually bent inwardly and outwardly to apply tensile or compressive bending residual stress on the outer surface of the pipeline steel. Based on the axial welding residual stress distribution induced by the girth weld from previous studies, the distances between the bend's center and the girth weld's center were selected from 0 mm to 30 mm to investigate the welding residual stress distribution. The distribution and depth profiles of corrosion pits and microcracks on those samples revealed that a higher density of microcracks and corrosion pits was observed on the samples with girth welds than on those without girth welds. Furthermore, it was found that the higher frequencies of deep pits and cracks ($> 80 \mu\text{m}$) were observed as the distance between the center of bend and weld centerline decreased. The interaction between welding residual stress and bending residual stress increased or decreased the significance of C-NNpHSCC, depending on the applied bending residual stress type. The mill scale on the metal substrate significantly impeded or enhanced the localized corrosion in the NNpH environment, significantly affecting the morphologies of pits and cracks on the samples. The future study requires the removal of the mill scale to rule out the effect of galvanic corrosion.

Keywords: Circumferential Near Neutral pH Stress Corrosion Cracking, Initiation and Stage I Growth, Field Bending, Girth Weld, Residual Stress Profile, Mill scale

Preface

The experimental setup presented in section 3.2 was originally designed by Dr. Zhezhu Xu, a Postdoctoral Fellow in the Department of Chemical and Materials Engineering, University of Alberta, under the supervision of Dr. Weixing Chen in the Department of Chemical and Materials Engineering, University of Alberta.

Acknowledgement

First, I would like to thank my supervisors, Dr. Weixing Chen and Dr. Reg Eadie, for guiding me through the research by providing feedback on my study and critical knowledge for the research.

I also thank the members of the examining committee, Dr. Weixing Chen, Dr. Reg Eadie, Dr. Kevin Hodder, and the examining committee chair, Dr. Jing Liu, for attending my thesis defence and giving me proper feedback to strengthen my thesis.

Special thanks to Dr. Zhezhu X, Dr. Shiong Wang, and Greg Nelson for their mentorship and for being good friends for me.

I thank my colleagues, Christine Vo and Hamed Shirazi, for helping me with several processes in my research and both technically and emotionally supporting me.

Finally, I sincerely thank my landlord, Shelagh Wildsmith, for providing me with a place to live and constantly supporting me throughout this journey, especially during the COVID-19 pandemic. I would not have been able to finish my studies without you.

Finally, thank you to CEFA for their financial support and for sharing their knowledge.

Table of Contents

Abstract.....	ii
Preface	iv
Acknowledgement	v
Chapter 1 : Introduction.....	1
Chapter 2 : Literature Review	4
2.1 Circumferential Near-Neutral pH SCC (C-NNpHSCC).....	4
2.2 Environment.....	5
2.2.1 Solutions.....	6
2.2.2 Temperature	8
2.2.3 Coating	9
2.2.4 Soil	17
2.2.5 Cathodic Protection (CP)	18
2.3 Axial Stresses.....	19
2.3.1 Axial Residual Stress	20
2.3.2 Applied Axial Stress.....	37
2.4 Materials	40
2.5 Mechanisms of NNpHSCC.....	41
2.5.1 Initiation and Stage I Growth of NNpHSCC	42
2.5.2 Stage II growth.....	48
Chapter 3 : Experimental Methods.....	56
3.1 Material and Specimen	56
3.1.1 Material	56
3.1.2 Lab-Scale Specimen.....	57
3.2 Static Corrosion Tests.....	61
3.3 Characterization Processes.....	64

3.3.1 Post-Test Processes	64
Chapter 4 : Results.....	68
4.1 Mill scale characterization	68
4.1.1 Distribution and frequency of corrosion pits.....	74
4.2 Characterization of Corroded Samples and Comparisons in Terms of Durations.....	80
4.2.1 Samples bent in compression with tensile residual stress on the surface (d = 30 mm)	81
4.2.2 Samples bent in compression with tensile residual stress on the surface (d = 15 mm)	87
4.2.3 Samples bent in tension with compressive residual stress on the surface (d = 30 mm)	92
4.2.4 Samples bent in tension with compressive residual stress on the surface (d = 15 mm)	97
4.2.5 Samples bent in compression with tensile residual stress on the surface (d = 0 mm)	103
4.2.6 Samples bent in compression with tensile residual stress on the surface (d = N/A)	108
4.2.7 Samples bent in tension with compressive residual stress on the surface (d = 0 mm)	113
4.2.8 Samples bent in tension with compressive residual stress on the surface (d = N/A)	118
Chapter 5 : Discussion.....	124
5.1 Effect of Welding Residual Stress on Pits & Cracks Morphologies and Distributions	125
5.2 Effect of Bending Residual Stress on Pits & Cracks Morphologies and Distributions	133
5.3 Effect of Static Corrosion Durations on Pits & Cracks Morphologies and Distributions.....	138
Chapter 6 : Conclusions.....	141
6.1 Recommendations for Future Work.....	142
Bibliography	144

List of Tables

Table 3.1 Chemical compositions of near-neutral pH C2 solution	63
Table 3.2 Schematics of the samples corroded for 90 days (Sample 1 to 8) and 150 days (Sample 9 to 16).	64

List of Figures

Figure 2.1 Three factors that cause C-NNpHSCC [10].....	5
Figure 2.2 Pourbaix diagrams of Fe-H ₂ O-CO ₂ system 25 °C and 1 bar [9]. (a) [Fe ²⁺] = 10 ⁻⁶ to 10 ⁻³ mol/l with anions at 10 ⁻² mol/l, (b) [Fe ²⁺] = 10 ⁻⁶ mol/l and [anions] = 10 ⁻³ to 10 ⁻¹ mol/l. Red/blue triangles show OCP values of mill-scaled and primer-pre-coated samples at different immersion times.....	7
Figure 2.3 Pit depth distribution per 1 cm at the cross-sectional surface of corroded samples with and without primer for 90 days [9].....	14
Figure 2.4 Cross-sectional morphology of mill scale and corrosion pits on the samples a) without primer and b) with primer corroded for 90 days [9].....	15
Figure 2.5 Schematics of the effect of mill scale on localized corrosion a), c), e) g): without primer and b), d), f), h): with primer [9].....	17
Figure 2.6 Schematics of cathodic protection [20].....	19
Figure 2.7 The relationship between predicted surface residual stress, number of cracks, and residual stress gradient, k (MPa/mm) [22].....	21
Figure 2.8 Axial residual stress distribution from the weld centerline of girth weld on a) outer diameter (OD) and b) inner diameter [31].....	23
Figure 2.9 Stress profile from the concave side to the convex side a) for original bend and b) after springback [17]	25
Figure 2.10 Change in axial residual stress distribution from WCL after applying a bending force of a) $\sigma_a^{LS} = 182$ MPa and b) $\sigma_a^{LS} = 337$ MPa [35]	27

Figure 2.11 Axial residual stress gradient over the length and depth of a pipe from WCL of girth weld a) before applying bending force, b) after applying $\sigma_a^{LS} = 154$ MPa and c) $\sigma_a^{LS} = 337$ MPa on the OD [35]	28
Figure 2.12 Von Mises equivalent stress on the outer surface a) before and after applying $\sigma_a^{LS} = 182$ MPa, b) before and after applying $\sigma_a^{LS} = 337$ MPa [35]	29
Figure 2.13 Axial residual stress distribution from WCL on whole pipe, quarterly sectioned pipe, and 6 mm width strip sectioned from a quarter pipe [31].....	31
Figure 2.14 Surface profiles at $\varphi = 90^\circ$ on the outer surface of a girth welded pipe before and after sectioning [31].....	32
Figure 2.15 Three components of welding residual stress derived by residual stress decomposition technique [26]	33
Figure 2.16 Change in bending component of the hoop and axial residual stress with an increase in r/t ratio [30]	34
Figure 2.17 Residual stress distribution measure by ND on a tensile specimen a) before and b) after tensile cyclic loadings [22]. Distances from the outer surface are shown in legends.	35
Figure 2.18 Residual stress distribution toward the inner surface of pipeline steel at and away from SCC colonies, measured with hole drilling method [36]	36
Figure 2.19 Change in axial stress in various pipeline steels by temperature change [17]..	38
Figure 2.20 Bathtub model for NNpH stress cracking [43]	42
Figure 2.21 Schematic of NNpHSCC initiation from coating disbondment [15]	44
Figure 2.22 Crack length-depth profiles of near-neutral pH SCC and high pH SCC [4].....	45

Figure 2.23 Blunted, the balloon-shaped crack propagated in the NNpH environment [45]	47
.....	47
Figure 2.24 The increase in crack length over time in two NNpH solutions with cyclic loadings [46]	48
.....	48
Figure 2.25 The effect of stress on the growth and dormancy of cracks [4]	49
.....	49
Figure 2.26 The mechanism of discontinuous crack growth: (a) Stress distribution ahead of the blunt crack tip, b) Triaxial zone at which HE and facilitated crack growth occurs, c) The crack becomes blunted again and reinitiated [47]	51
.....	51
Figure 2.27 Crack growth rate (da/dN) as a function of combined factor in C2 and NOVATW solutions [48]	53
.....	53
Figure 2.28 Crack growth rate and change in the mechanism of crack growth at different loading frequencies [49]	54
.....	54
Figure 3.1 X52 pipeline steel used for the experiment	56
.....	56
Figure 3.2 a) Geometry of single-V girth weld on the selected specimen and b) picture of weld metal and heat affected zone on the specimen	57
.....	57
Figure 3.3 Schematic of a stick-shaped specimen	58
.....	58
Figure 3.4 Brief schematic of X52 pipeline steel and the specimens cut from it	59
.....	59
Figure 3.5 Picture of a specimen subjected to the mechanical bending process	59
.....	59
Figure 3.6 Front of a fabricated specimen ($d = 0$ mm) with the locations at which bending force was applied	60
.....	60
Figure 3.7 Schematics of control samples	61
.....	61

Figure 3.8 Static corrosion cells filled with C2 solution and the specimens, connected to 5% CO ₂ + balanced N ₂ gas cylinders.....	62
Figure 3.9 Cross-sectional surfaces of sectioned samples mounted in epoxy resin.	65
Figure 3.10 a) Distribution of pits and cracks over the length of a corroded sample and b) frequencies of pits and cracks in varying depths derived from characterization processes.	67
Figure 4.1 Schematics of control sample A and a)-d) surface morphologies of mill scale layer at corresponding locations	69
Figure 4.2 Atomic concentration (%) of a) white layer and b) dark layer of oxide in Figure 4.1 d).....	70
Figure 4.3 Schematics of control samples B&C and a)-e) surface morphologies of mill scale layer at corresponding locations	72
Figure 4.4 Surface morphologies of control samples A, B, and C at the center of the bend	74
Figure 4.5 BSD images of typical countable/uncountable pits and cracks observed on sample surfaces.....	75
Figure 4.6 a) Distribution and b) Total frequency of pits and cracks in the control samples vs. depth of pits and cracks.....	78
Figure 4.7 Cross-sectional morphology of a corroded sample at the weld toe	81
Figure 4.8 Schematics of Sample 1 & 9 as well as the cross-sectional surface morphologies of the samples; a) BSD image of sample 1 surface covered with thick mill scale layer a) near and b) away from the center of the bend, c) magnified MDS image of a crevice corrosion site with cracked mill scale layer in the area away from the center of the bend of sample 1, d) OM image of a crevice corrosion site with dissolved mill scale near the center	

of the bend of sample 9, e) a magnified BSD image of transgranular crack observed near the center of the bend of sample 9, and f) BSD image of a colony of shallow pits near the girth weld of sample 9.	83
Figure 4.9 a) Distribution and b) frequency of pits and cracks in samples 1 (90 days) & 9 (150 days) and control samples.	86
Figure 4.10 Schematics of Sample 2 & 10 as well as the cross-sectional surface morphologies of the samples; a) BSD image of sample 2 surface covered with mill scale near the center of the bend, b) magnified BSD image of a crack-like feature propagated from a pre-existing pit covered with mill scale near the center of the bend of sample 2, c) magnified BSD image of a crevice corrosion site covered with partially dissolved mill scale layer near the center of the bend of sample 10, d) magnified BSD image of a microcrack propagated from a corrosion pit near the center of the bend of sample 10, e) magnified BSD image of a crack-like feature with coarsened tip near the center of the bend of sample 10, and f) a short crack-like feature with coarsened tip propagated from a corrosion pit near the center of the bend of sample 10.	88
Figure 4.11 a) Distribution and b) frequency of pits and cracks in Sample 2 (90 days) & 10 (150 days) and control samples.	91
Figure 4.12 Schematics of Sample 3 & 11 as well as the cross-sectional surface morphologies of the samples; a) BSD image of sample 3 surface covered with cracked mill scale layer near the center of the bend, b) magnified BSD image of a crack-like feature propagated under mill scale layer near the area away from the center of the bend of sample 3, c) BSD image of sample 11 surface with dissolved mill scale near the center of the bend,	

and d) OM image of crevice corrosion sites partially covered with dissolved mill scale layer in the region away from the center of the bend of sample 11. 93

Figure 4.13 a) Distribution and b) frequency of pits and cracks in Sample 3 (90 days) & 11 (150 days) and control samples. 96

Figure 4.14 Schematics of Sample 4 & 12 as well as the cross-sectional surface morphologies of the samples. a) BSD image of sample 4 near the center of the bend, b) magnified BSD image of corrosion pit with a crack-like feature near the center of the bend of sample 4, c) OM image of a colony of shallow pits found in the area way from the center of the bend of sample 4, d) BSD image of remaining mill scale covering the surface of sample 12 near the center of the ben, e)BSD image of a coarsened corrosion pit with sharp tips near the center of the bend of sample 12, and f) BSD image of a widened corrosion pit in the area away from the center of the bend of sample 12. 98

Figure 4.15 a) Distribution and b) frequency of pits and cracks in samples 4 (90 days) & 12(150 days) and control samples. 101

Figure 4.16 Schematics of Sample 5 & 13 as well as the cross-sectional surface morphologies of the samples; a) OM image of corrosion pits with exfoliated mill scale layer near the center of the bend of sample 5, b) BSD image of cracks coalesced into a balloon-like pits near the center of the bend of sample 5, c) magnified BSD image of a large corrosion pit with sharp tip near the center of the bend of sample 13, d) magnified BSD image of a branched crack near the center of the bend of sample 13, and e) magnified BSD image of a crack-like feature propagated from a sharp corrosion pit in the area away from the center of the bend of sample 13. 104

Figure 4.17 a) Distribution and b) frequency of pits and cracks in Sample 5 (90 days) & 13 (150 days) and control samples 107

Figure 4.18 Schematics of Sample 6 & 14 as well as the cross-sectional surface morphologies of the samples; a) BSD image of sample 6 surface with partially exfoliated mill scale layer near the center of the bend and b) in the area away from the center of the bend, c) BSD image of thick mill scale layer covering the surface of sample 14 near the center of the bend, and d) OM image of partially dissolved mill scale covering the surface of sample 14 in the area away from the center of the bend. 109

Figure 4.19 a) Distribution and b) frequency of pits and cracks in samples 6 (90 days) & 14 (150 days) and control samples. 112

Figure 4.20 Schematics of Sample 7 & 15 as well as the cross-sectional surface morphologies of the samples; a) BSD image of a colony of corrosion pits with exfoliated mill scale layer on the surface of sample 7 near the center of the bend, b) OM image of the surface of sample 7 with largely exfoliated mill scale layer in the area away from the center of the bend, c) BSD image of the surface of sample 15 covered with mill scale layer near the center of the bend, and d) OM image of the surface of sample 15 with largely remaining mill scale in the area away from the center of the bend. 114

Figure 4.21 Distribution and frequency of pits and cracks in Samples 7 (90 days) & 15 (150 days) and control samples..... 117

Figure 4.22 Schematics of Sample 8 & 16 as well as the cross-sectional surface morphologies of the samples; a) OM image of the surface of sample 8 with exfoliated mill scale near the center of the bend, b) OM image of the surface of sample 8 with partially

exfoliated mill scale in the area away from the center of the bend, c) OM image of the surface of sample 16 with exfoliated mill scale near the center of the bend, and d) OM image of sample 16 surface with exfoliated mill scale in the area away from the center of the bend.....	119
Figure 4.23 a) Distribution and b) frequency of pits and cracks in samples 8 & 16 and control samples.	122
Figure 5.1 Distribution of pits and cracks over the length of samples corroded for 150 days with (a tensile bending residual stress on the OD and b) compressive bending residual stress on the OD.....	126
Figure 5.2 Frequencies of pits and cracks in different depths on the samples corroded for 150 days with a) tensile bending residual stress on the OD and b) compressive bending residual stress on the OD.....	127
Figure 5.3 Estimated axial residual stress from WCL on the outer surface of the corroded samples.	132
Figure 5.4 Distribution of pits and cracks deeper than 80 μm over the length of samples corroded for 150 days with (a tensile bending residual stress and b) compressive bending residual stress on the OD.....	135

Chapter 1 : Introduction

Failure of pipelines because of stress corrosion cracking (SCC) was first recognized in 1965, US, Louisiana [1]. This early SCC exhibited branched intergranular cracks in the environment with a pH of 9 to 11. Because of the environment in which the crack was initiated and propagated, this type of SCC is now called high-pH SCC (HPHSCC). In 1986, TransCanada Pipeline (TCP) conducted a failure analysis on three ruptures in the in-service pipeline [2][3]. Unlike HPHSCC, many of the cracks observed on the pipeline were transgranular and showed small branches. Furthermore, the pH of the electrolyte in which the failure occurred was approximately 7.5. TCP concluded that these cracks were a different type of SCC from HPHSCC, resulting in the first recognition of NNpHSCC. After this discovery, a circumferential SCC found in 1975 was also identified as the first circumferential NNpHSCC (C-NNPHSCC) [3].

Since the discovery of NNpHSCC, research on the mechanisms of NNpHSCC and the factors affecting these mechanisms has been extensively conducted. It was found that the entire mechanism of NNpHSCC consists of multiple stages [4]:

- Coating disbondment on the pipe surface because of geological hazards or manufacturing errors
- Initiation of microcracks resulting from surface defects or localized corrosion sites
- Anodic dissolution-dominated crack propagation and dormancy (Stage I)
- Cycle of reactivation, propagation and dormancy of cracks caused by cyclic loading and hydrogen embrittlement (HE) (Stage II)

- Unstable crack growth leading to rupture (Stage III)

The factors influencing the mechanisms mentioned above, such as environmental conditions, metallurgical factors, and type of stress, were also studied and identified.

However, because of the minor occurrence of circumferential (along the circumference of the pipe) cracks in the NNpH environment and the absence of ruptures, most of the study has been focused on longitudinal (along the length of the pipe) cracks. Furthermore, although the effects of welds and bends on initiation and Stage I growth of NNpHSCC have been individually studied [5]–[7], the combination of both factors has yet to be extensively investigated. Additionally, little research has been conducted on the influence of mill scale on NNpHSCC [8][9].

As such, the work contained in this thesis focuses on the correlations between the morphologies of pits and microcracks in the initiation and early stage of C-NNpHSCC and the presence of mill scale, girth weld-induced residual stress, and bending residual stress on susceptible material.

In order to investigate these effects, static corrosion tests on stick-shaped specimens fabricated from girth welded pipe in NNpH solution were conducted. Prior to the testing, the fabricated specimens were subjected to mechanical bending at different bend angles to apply different types of residual stress on the outer diameter (OD). Since the degree of welding residual stress varies with the distance from the weld centerline (WCL), the specimens were designed such that the distance between the center of the bend and WCL (d) differs. From the results of this study, the effects of individual factors and the

interaction between welding and bending residual stresses on the initiation and early stages of C-NNpHSCC were estimated.

The structure of this thesis is as follows: First, the basic understanding of environmentally assisted cracking (EAC), factors affecting the initiation and growth of C-NNpHSCC, and detailed mechanisms of NNpHSCC are explained in Chapter 2. Second, the detailed experimental procedures to carry out this study are presented in Chapter 3. Chapter 4 includes the cross-sectional surface morphologies of pits and microcracks in each sample and the statistical analysis results. The results explained in Chapter 4 are interpreted in Chapter 5. Finally, the conclusions of this study and future recommendations are exhibited in Chapter 6.

Chapter 2 : Literature Review

2.1 Circumferential Near-Neutral pH SCC (C-NNpHSCC)

As mentioned in Chapter 1, NNpHSCC is the phenomenon that occurs on pipeline steel in the NNpH environment. Unlike HpHSCC, the initiation and early growth of the cracks occur through localized corrosion rather than a film rupture mechanism. Later studies specified the conditions under which NNpHSCC occurs and summarized these as follows [4]:

- Electrolyte is a dilute HCO_3^- solution such as groundwater with a pH of 5.5 to 7.5.
- Electrolyte contains a high concentration of CO_2 and a low concentration of O_2 .
- Corrosion potential ranges from -760 mV Cu/CuSO₄ to -790 mV Cu/CuSO₄ (Free potential).
- Coatings on the pipe surface are disbonded.
- Cathodic protection (CP) is applied but is unable to penetrate under the coating where the defect arises.

NNpHSCC usually refers to crack growth in the longitudinal direction because the majority of cracks observed in the field propagated along the length of pipes. As such, little research on C-NNpHSCC has been conducted.

Similar to SCC, C-NNpHSCC requires three factors: axial tensile residual and applied stress, NNpH environment, and susceptible material to the environment, which is visible in Figure 2.1 [10]. Each factor is explained in detail in the following sections.

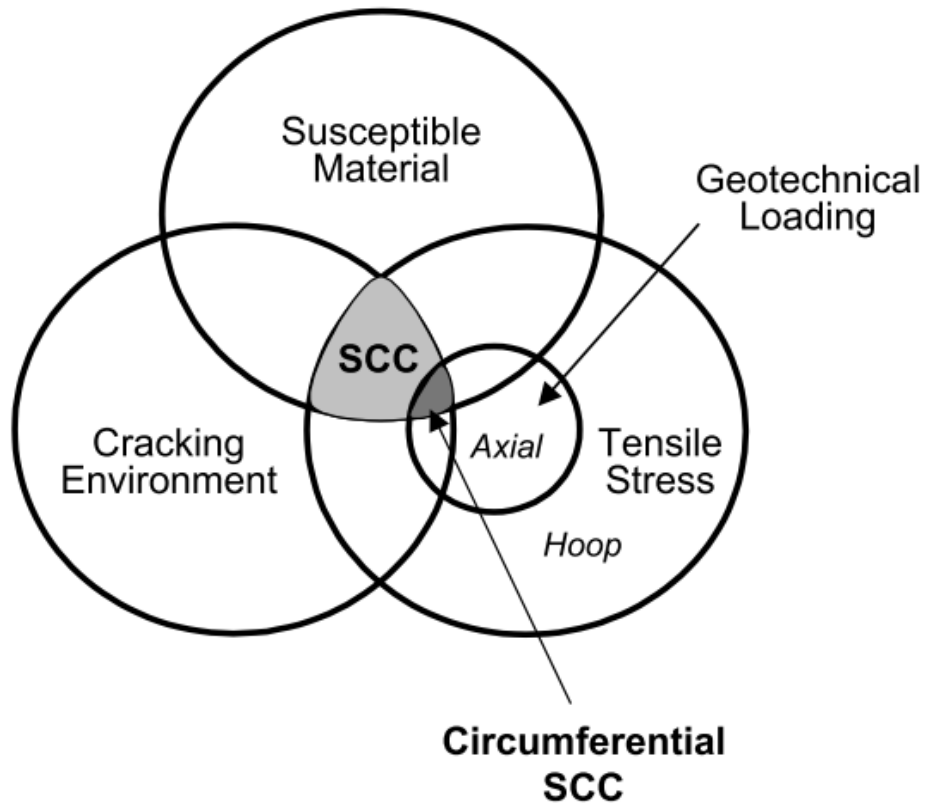


Figure 2.1 Three factors that cause C-NNpHSCC [10]

2.2 Environment

SCC requires an environment that is corrosive to the material. In this context, environment refers to the electrolyte and the combination of other factors, such as the soil surrounding the buried pipeline, the level of cathodic protection, and the type of coatings [3].

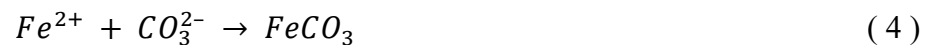
It has been consistently reported that disbonded coating and dilute bicarbonate solution are vital to NNpHSCC. Cathodic protection has been utilized as a countermeasure against surface corrosion. However, it has been reported that cathodic protection current may not be able to penetrate through the pipeline for some types of coatings, inadequate level of

cathodic protection or in soils with high resistivity [11]. The details of the abovementioned environmental factors are discussed in the following subsections.

2.2.1 Solutions

For the initiation and growth of SCC to occur, direct contact between the surface of susceptible material and the potent, corrosive electrolyte is required. In the case of NNpHSCC, this electrolyte is a carbonate (HCO_3^-)/bicarbonate (CO_3^{2-}) solution with a pH of 5.5 to 7.5 [3][4][12][13]. The formation of this solution is closely tied to the chemical compositions of soil and temperature. If the earth is unaerated and is filled with CO_2 from decaying organic matter, CO_2 diffuses faster into the groundwater within the soil than O_2 [14]. Furthermore, the solubility of CO_2 in groundwater is inversely proportional to the temperature. As such, with unaerated soil and a low-temperature environment, the pH of the bicarbonate solution is maintained within the required range, enabling NNpHSCC to occur [3].

The groundwater enters the disbonded area and contacts the metal substrate, initiating steel's anodic dissolution and water's cathodic reduction as follows [4][9][15]:



Although the oxidation of Fe and reduction of electrolytes have been observed in the field and experiments, the formation of protective siderite (FeCO_3) film was rarely observed.

Wang *et al.* plotted Pourbaix diagrams of the Fe-H₂O-CO₂ system at room temperature, which is visible in Figure 2.2 a) and b) [9].

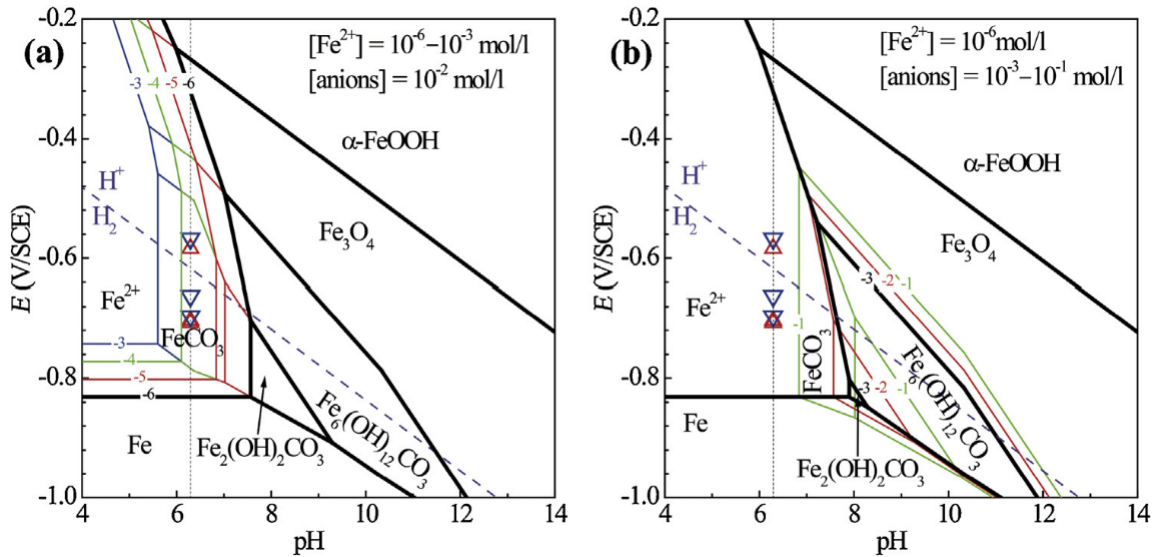


Figure 2.2 Pourbaix diagrams of Fe-H₂O-CO₂ system 25 °C and 1 bar [9]. (a) [Fe²⁺] = 10⁻⁶ to 10⁻³ mol/l with anions at 10⁻² mol/l, (b) [Fe²⁺] = 10⁻⁶ mol/l and [anions] = 10⁻³ to 10⁻¹ mol/l. Red/blue triangles show OCP values of mill-scaled and primer-pre-coated samples at different immersion times

According to Figure 2.2 a) and b), under the NNpH environment (pH = 6.3), FeCO₃ is unstable and not formed unless the concentration of anions and Fe²⁺ are at least 10⁻² mol/l and ~ 10⁻⁴ mol/l, respectively. Since the bulk solution surrounding the pipe surface unlikely contains those chemical species with such concentrations, forming a protective film in the NNpH environment is unlikely. This is the reason why the crack growth in the NNpH environment does not involve an ordinary film rupture mechanism. However, precipitation

of FeCO_3 at the locations with highly accumulated Fe^{2+} is still possible, as discussed in the later section.

It must also be noted that the significance of NNpHSCC depends on the concentration of ions involved with the aforementioned reactions, particularly CO_3^{2-} . Chen *et al.*

investigated the crack initiation and growth in four synthetic NNpH solutions with the same chemical compositions except for CaCO_3 , as well as NS4 (pH = 6.81) and NOVATW (pH = 7.1) solutions, which had been used for the studies on NNpHSCC [13]. These solutions were purged with 5% CO_2 + balanced N_2 gas, which led to an increase in pH with an increase in CaCO_3 concentration from 5.9 to 7.2. As a result, it was found that the solutions with low pH (~6.3) exhibited an overall higher corrosion rate. In contrast, the corrosion rate in the solutions with high pH (~7.2) diminished over time. This is because of the formation of a protective film attributed to the increased CO_3^{2-} concentration in the solution, as discussed above. Crack growth in the C2 solution (pH = 6.3) was compared with the NOVATW solution, which revealed that the crack growth rate in the C2 solution was three times higher than that in the NOVATW solution. They estimated that the following three factors could explain this result: Formation of FeCO_3 layer that inhibited further dissolution in NOVATW solution, hydrogen diffusion in the triaxial zone with a high-stress concentration in C2 solution, and crack blunting from room temperature creep that occurred in NOVATW solution.

2.2.2 Temperature

Temperature refers to the pipeline surface, the soil surrounding it, and groundwater flowing between both substances, which are supposed to be identical. The effect of temperature can

be roughly separated into mechanical and chemical products. Because of the heterogeneous temperature distribution, thermal stress may be applied on the surface along longitudinal and circumferential directions, contributing to the initiation and growth of both circumferential and axial SCC [3]. The detail of this force is explained in the later section. Temperature changes can also significantly contribute to creating a corrosive NNpH environment. Since the solubility of CO₂ in water is inversely proportional to the temperature, the temperature must be low so that CO₂ can diffuse faster than O₂ in soil into groundwater, forming a near-neutral bicarbonate solution. Temperature also has a significant impact on the susceptibility of the pipeline to HE. The equation for hydrogen diffusivity is expressed as follows:

$$D = D_0 \exp\left(-\frac{Q}{RT}\right) \quad (5)$$

D₀ is the diffusion constant, Q is the activation energy, and R is the gas constant. This indicates that hydrogen diffusivity in a given metal exponentially increases with temperature rise, leading to increased HE susceptibility. Therefore, a specific temperature range exists where the diffusion of hydrogen and CO₂ is most favourable for the initiation and growth of NNpHSCC. Based on reports from TransCanada and NGTL systems, it is estimated that the temperature range is at 10 degrees or lower because of a high frequency of NNpHSCC [3].

2.2.3 Coating

When it comes to preventing corrosion in buried pipelines, there are two critical components: the external coating and the cathodic protection system [3]. The coating plays

a crucial role in safeguarding the pipeline's surface from any potential damage caused by the surrounding environment. The factors related to the effectiveness of coatings against NNpHSCC have been well documented and are summarized below.

2.2.3.1 The resistance to disbondment

It is well known that NNpHSCC is primarily caused by the infiltration of electrolytes or the development of moisture into the disbonded coating area [3][11]. This coating disbondment is caused by the poor adhesion of the coating, improper installation of coating, degradation of coatings because of the long-term operation and high temperature, initial surface condition of the parent material, and geological hazards such as soil movement and land sliding [16]. To prevent coating disbondment, a selection of coatings with good adhesive properties is required. Another crucial factor is the parent material's surface roughness and impurities that prevent good adhesion between coatings and the material surface. Hence, proper surface cleaning and rough surface finishing are necessary before the installation. Although not mandatory, using primer on the parent surface may enhance the adhesion, as it smooths out the surface. Removal of the mill scale, which may worsen the localized corrosion, is also recommended. It must also be noted that a coating discontinuity, also known as a holiday, is often formed at poorly adhesive areas such as at weld toes and overlapped areas. As such, extra care is needed when installing the coatings. The mechanical properties of coatings should be kept the same because of long-term operation and temperature changes. Finally, high resistance to impact is also required for the pipe buried in unstable terrain.

2.2.3.2 Ability to prevent corrosion after disbonding

As mentioned above, coatings and CP are used as countermeasures against corrosion to ensure that either of the systems works when the other fails. However, if the coating disbondment occurs, there is a possibility that the disbonded coatings impede the cathodic current. This is because the moisture developed in a space at the disbonded zone dissipates the cathodic current, preventing it from reaching the parent material. The trapped moisture also forms a potent NNpH environment, initiating corrosion on the surface. Selecting coatings with high electric conductivity and low water permeability is necessary.

2.2.3.3 History of Coatings and NNpHSCC

The relationship between the type of coatings and initiation of NNpHSCC has been studied and well-documented by researchers [3][11][17]. They all agree that polyethylene tapes offer the weakest protection to NNpHSCC, followed by bitumastic coating, shrink sleeve and fusion bonding epoxy. NNpHSCC occurs the most under polyethylene tape coating because of its poor adhesive properties, low electric conductivity, and high-water permeability. Disbondment of polyethylene tapes occurs along the longitudinal or circumferential weld reinforcement and overlapped area of the tapes, leading to moisture development and cathodic current impediment [3]. It must also be noted that polyethylene is not considered ineffective as a protective measurement. Indeed, extruded polyethylene offers excellent protection from NNpHSCC because of its improved adhesive properties, albeit poor compatibility with cathodic protection. Bituminous enamel coatings, such as asphalt and coal tar coatings, are also prone to disbondment if the surface condition is poor before the installation. Although the probability of cathodic current reaching the pipe

surface is higher than that under polyethylene tapes because of higher electrical conductivity and saturated moisture under disbonded coating, cathodic current impediment may still occur because of external factors such as the soil with poor drainage. NNpHSCC is unlikely to occur under fusion bonding epoxy coating because of its high adhesive properties and electric conductivity.

2.2.3.4 Mill scale

While it is true that the contribution of coating disbondment is significant to the initiation and growth of NNpHSCC, cracking may occur on the pipe without coatings [11]. One of the causes is considered to be the presence of mill scale. Mill scale is a brittle iron oxide layer formed on the surface of low-carbon steel during the hot rolling process. This generally consists of three oxide layers: FeO (wüstite), Fe₃O₄(magnetite), and Fe₂O₃(hematite), although the compositions vary depending on the rolling temperature, the composition of the parent metal and cooling rate [18][19]. Much like coatings, the mill scale layer uniformly covers the surface of the parent metal and protects it from a corrosive environment. However, because of the porous and brittle features of the mill scale, cracking or removal of the mill scale during manufacturing, installation, and operation is inevitable. Such damaged portions of the mill scale become paths for the contact between electrolyte and bare metal, yielding a localized corrosion site. This localized corrosion is further accelerated by a galvanic couple formed because of the potential difference between bare metal (anode) and mill scale (cathode) [8]. Shirband investigated the effect of the mill scale on initiation and Stage I growth of NNpHSCC on X52 steel subjected to cyclic loading. As

a result, it was found that the crack initiation frequency increased by approximately five times in comparison to the sample with no mill scale [8].

As mentioned above, for better adhesion of coatings on the pipe surface, primer may be applied on the pipe surface, including the mill scale. Wang *et al.* examined how the presence of primer and mill scale affects the initiation and growth of NNpHSCC in two types of X65 steel specimens [9]. The composition of the mill scale was examined with EDS and Raman spectrum and identified as magnetite, hematite, and lepidocrocite (γ -FeOOH). The specimens included one with both mill scale and primer and one with only mill scale. They were all immersed in the C2 solution for 90 days. Figure 2.3 shows the number of corrosion pits observed on the above specimens with different depths. As can be seen, the number of pits observed on the specimen with primer and mill scale is higher than that with mill scale. Moreover, the pits deeper than 30 μm were only observed on the specimen with primer and mill scale.

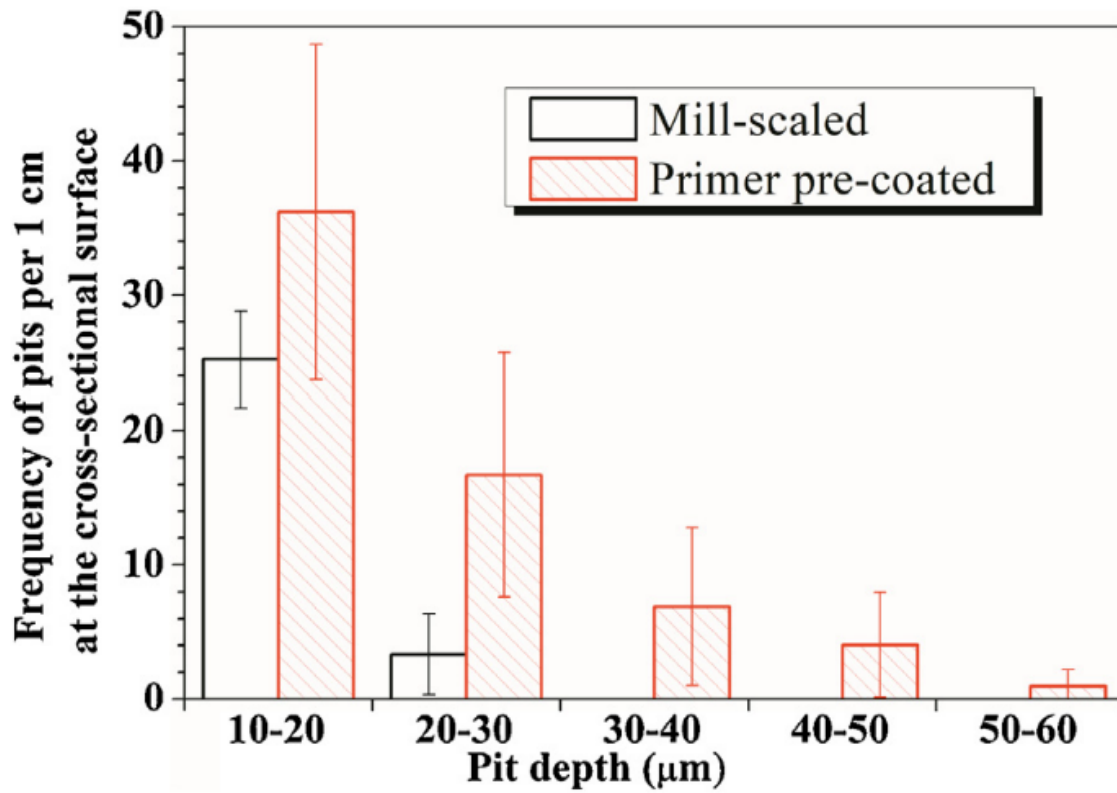


Figure 2.3 Pit depth distribution per 1 cm at the cross-sectional surface of corroded samples with and without primer for 90 days [9]

Figure 2.4 a) and b) show the cross-sectional morphologies of mill scale and corrosion pits on the specimens a) with primer and b) without primer, respectively.

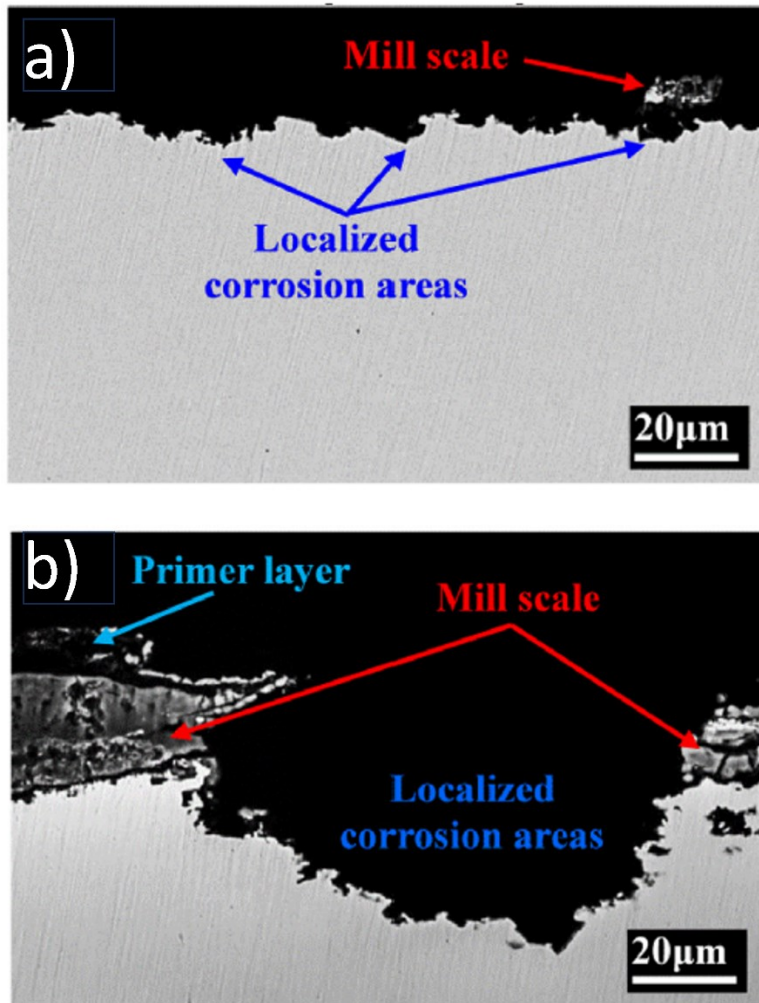
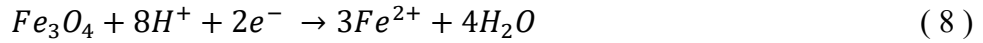
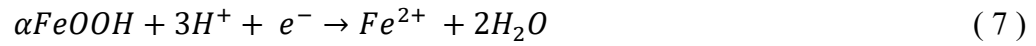
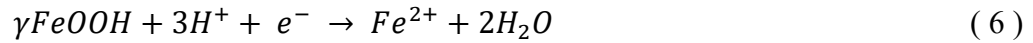


Figure 2.4 Cross-sectional morphology of mill scale and corrosion pits on the samples a) without primer and b) with primer corroded for 90 days [9]

Although localized corrosion sites are observable in both Figure 2.4 a) and b), Figure 2.4 b) shows a large remaining mill scale layer, whereas only a small portion of the mill scale is observed in Figure 2.4 a). They concluded that the lower significance of localized corrosion on the specimen without a primer could be accounted for by the loss of galvanic couples caused by the dissolution of mill scale by the hydrogen evolution reactions as follows [9]:



Furthermore, the author discovered that the accumulation of Fe^{2+} and CO_3^{2-} may occur at narrow, open gaps, such as the porous and cracked sites in the mill scale, satisfying the required conditions to produce siderite. In this study, it was concluded that the larger portion of the remaining mill scale in Figure 2.4 b) and more significant localized corrosion on the specimen with a primer is likely because of the primer protecting the underneath mill scale layer from the chemical reactions mentioned above, extending the duration of galvanic corrosion between the mill scale and parent metal. The schematics of these mechanisms are summarized in Figure 2.5 a) to h).

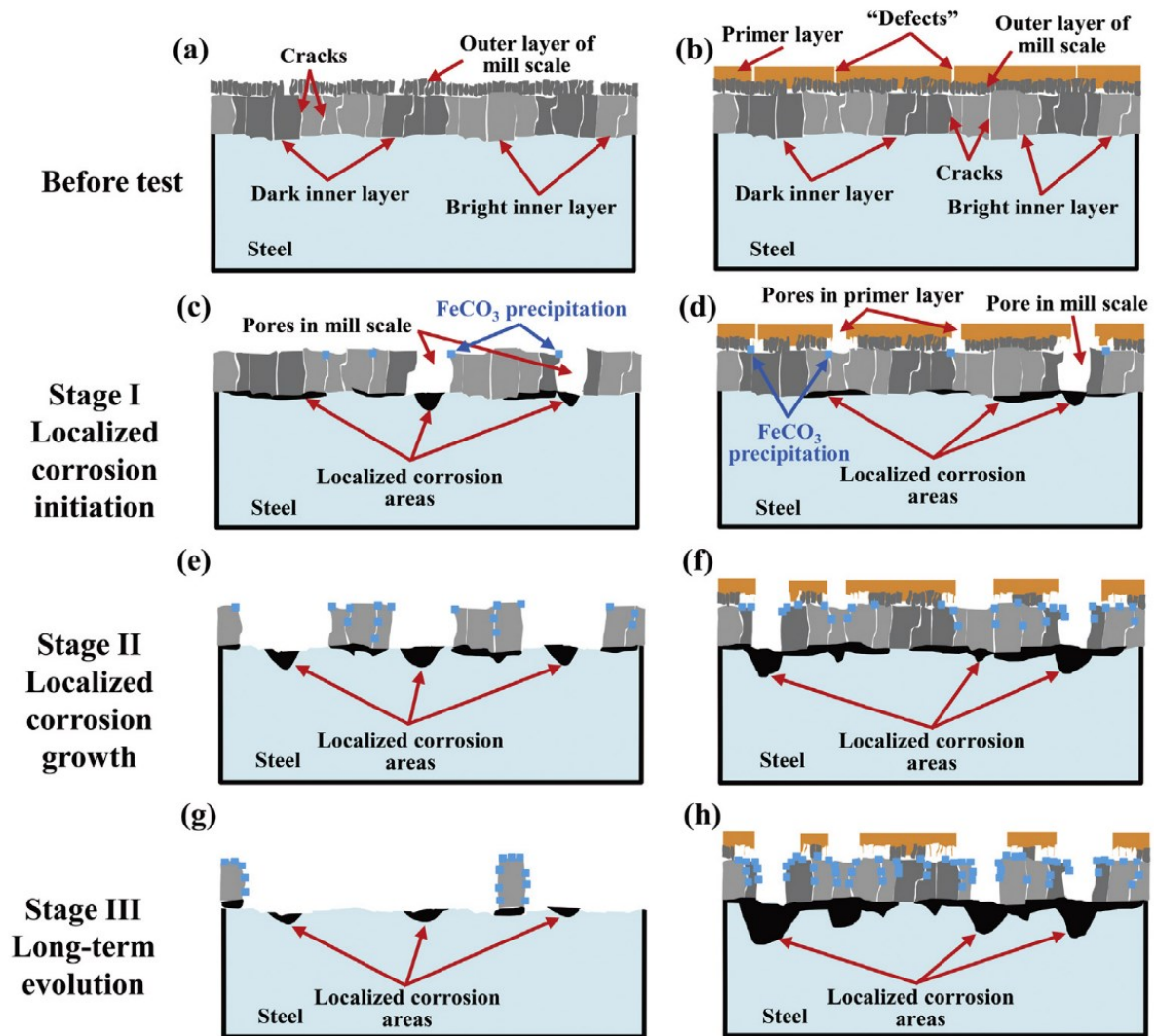


Figure 2.5 Schematics of the effect of mill scale on localized corrosion a), c), e) g): without primer and b), d), f), h): with primer [9]

2.2.4 Soil

Soil topography, drainage level, and resistivity are crucial in forming the NNpH environment. Like the polyethylene tapes, soil with high resistivity also impedes cathodic protection current, leading to the failure of CP. Soil resistivity is mainly tied to the soil

drainage level or the ability of the soil to store water. For instance, clay soils can hold water within their pores, lowering the moisture level throughout the structure and resistivity [3]. A high moisture level is developed if the soil is poorly drained or imperfectly drained, protecting the pipe surface from cathodic protection current. Soil drainage level also determines if the ground is aerobic or anaerobic. Anaerobic soil favours NNpHSCC as it contains more CO₂ than O₂, increasing the possibility of forming a bicarbonate solution with near-neutral pH. Furthermore, because of the lack of O₂ in anaerobic soil, sulphate in the soil is reduced to sulfide by sulfate-reducing bacteria. The synthesized sulfide prevents the formation of hydrogen gas and allows atomic hydrogen to diffuse into the metal, causing HE [3].

2.2.5 Cathodic Protection (CP)

Cathodic protection (CP) is the system that prevents anodic reactions between metal and electrolyte by applying a negative potential to a structure [20]. Two main types of CP systems are commonly used. The first type is known as sacrificial anode CP. This system employs an anode material that is more electronegative than pipe steel. Once the anode is connected to the pipe, the pipe then acts as the cathode in the circuit. This helps to prevent corrosion from occurring. Materials such as zinc and magnesium are typically used as sacrificial anodes for underground pipelines. The second type of corrosion prevention system is known as impressed-current CP. This system involves the use of an external power supply, commonly known as a rectifier. The rectifier regulates the voltage between the pipe and an anode. The anode could be cast iron, graphite, platinum clad, mixed metal oxide, etc. The impressed-current CP system ensures that the pipe becomes the cathode in

the circuit. This helps to prevent corrosion from occurring. The schematics of these systems are shown in Figure 2.6.

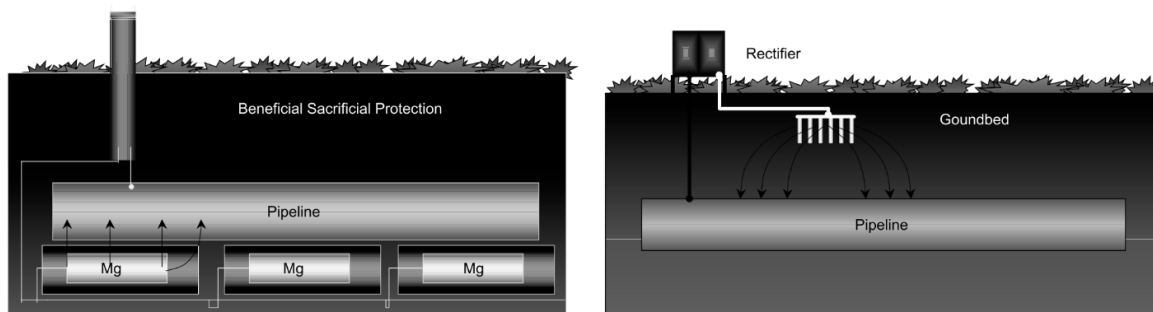


Figure 2.6 Schematics of cathodic protection [20]

As mentioned above, cathodic protection is also effective in the NNpH environment, particularly with proper coating on the surface of the targeted metal. However, the measure of protection depends on numerous factors, such as the coating type and soil moisture level between the source of cathodic current and the targeted material [3]. In the case of polyethylene tape-coated pipes, the cathodic protection is limited to a few centimetres from the areas where the coating is lifted or damaged because of the shielding effect caused by the disbonded tape. Soils with high drainage, such as sandy soil, contain little moisture, thus lacking the electric path for the cathodic current to reach the targeted metal.

2.3 Axial Stresses

As mentioned above, both applied and residual stresses are the main factors for NNpHSCC to occur, regardless of the direction of the cracks. Therefore, the identification and analysis of the stresses are necessary to determine the safest operating conditions and environment for the pipelines.

2.3.1 Axial Residual Stress

Residual stresses greatly influence the initiation and Stage I growth of NNpHSCC, as the surface with high compressive residual stress becomes more anodic than the adjacent areas, forming a stress corrosion cell [7]. Although both tensile and compressive residual stress decrease the activation energy required for metal atoms to leave the surface, compressive stress also increases the surface atomic density, ultimately increasing corrosion resistance [21]. Furthermore, since tensile stress is required for pit-to-crack transition, the surface with high tensile residual stress will likely exhibit more crack initiation sites than the others. This, however, does not mean that the number and depth of cracks are proportional to the surface tensile residual stress. Van Boven *et al.* investigated the effect of surface residual stress on the initiation and early growth of NNpHSCC by applying cyclic loadings on the specimens immersed in NNpH solution [7][22]. They plotted the surface residual stress on the specimen measured with neutron diffraction (ND) over the length and superimposed it with the frequencies of cracks, of which the result is visible in Figure 2.7.

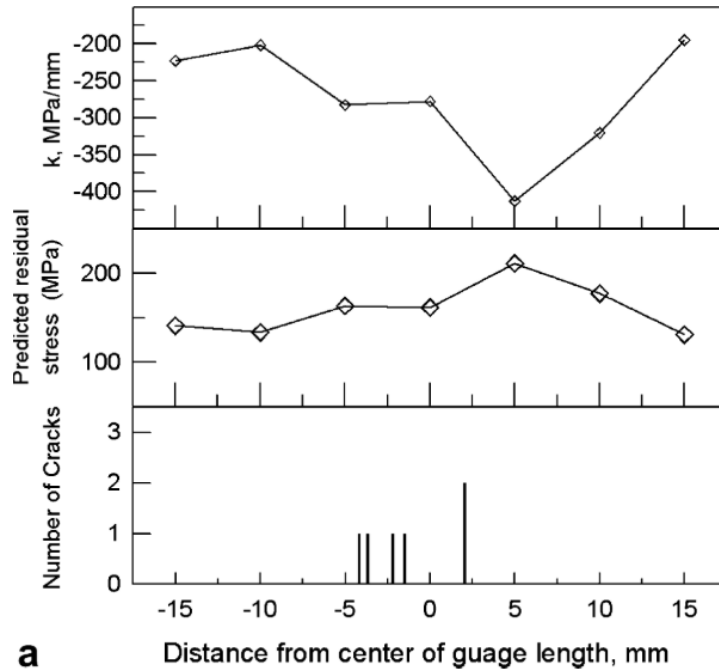


Figure 2.7 The relationship between predicted surface residual stress, number of cracks, and residual stress gradient, k (MPa/mm) [22]

As shown in Figure 2.7, cracks were mainly observed in the area with moderate residual stress, whereas no crack was observed in the area with the highest surface tensile residual stress. This is because of the self-equilibrating feature of residual stress distribution throughout a structure; the net sum of residual stress must be balanced out.

Generally, as shown in Figure 2.7, the steepness of the residual stress gradient in the depth direction, k (MPa/mm), is proportional to the magnitude of local surface residual stress.

This indicates that the pits initiated at the most tensile zone experienced the highest reduction of residual stress in the depth direction, thus losing the driving force for crack

initiation. On the other hand, the area with moderate tensile residual stress had a more benign residual stress gradient that enabled both the initiation and growth of cracks.

The sources of axial residual stresses are mainly from the manufacturing processes, such as the original fabrication of the pipe sections, welding, forming, machining, grinding, handling, and assembling of the pipeline [23]. Residual stress also emerges from the mechanical deformation on the pipe surface because of the impact of materials such as rocks and field bends caused by geological hazards such as settlement and landslides.

While the literature confirms that the initiation and growth of axial SCC are indeed likely to occur at weld toes because of the low corrosion resistance at the HAZ and high localized stress, limited literature on the correlations between welding residual stress and initiation and Stage I growth of C-NNpHSCC is currently available [6][24].

2.3.1.1 Welding Residual Stress

Welding processes have been crucial for countless industries, including the pipeline industry. While joining pipelines by welding significantly reduces both cost and time for pipeline construction, the problems arising from this process, particularly residual stress, must be analyzed and addressed.

During welding, metal pieces are heated to their melting temperature and fused, followed by a cooling process and alteration of microstructures. During the cooling process, the weld metal and parent metal near the fusion zone experience thermal contraction, whereas the region away from weld metal does not change its dimensions because of non-homogeneous heat distribution. Because of this difference, strain incompatibility will arise between the weld and parent metals. As a result, residual stress emerges throughout the structure. The

developed residual stress differs with numerous factors, such as pipe thickness, number of passes, weld geometry, deposition sequence, pipe radius to thickness ratio (r/t), global restraints, material properties, weld method, inter-pass temperature, and heat input [25]. For the pipeline girth weld, heat input, wall thickness (t) and r/t ratio significantly affect both axial and hoop residual stress distributions [26]–[30].

2.3.1.2 Axial Welding Residual Stress from Girth Weld on In-Service Pipelines

There are several methods for the measurement of through-thickness residual stress distributions from the weld centerline (WCL), such as the hole-drilling technique, X-ray diffraction (XRD) and neutron diffraction (ND) methods. Hempel *et al.* plotted axial residual stress gradients around a girth weld on the outer and inner surfaces of austenitic steel pipe through XRD and ND, visible in Figure 2.8 a) b) [31].

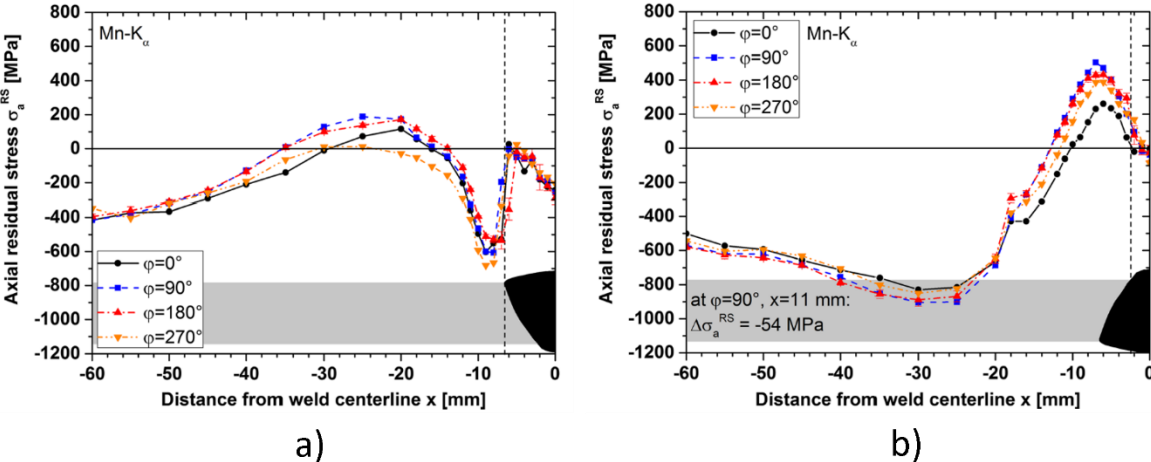


Figure 2.8 Axial residual stress distribution from the weld centerline of girth weld on a) outer diameter (OD) and b) inner diameter [31]

Figure 2.8 a) shows that the residual axial stress on the OD near the weld centerline is compressive and shifts tensile toward the base metal. Tensile axial residual stress peaks at $|x|$ (Distance from weld centerline) = 30 mm and gradually decreases with an increase in $|x|$. Contrary to the OD, axial residual stress distribution on the ID in Figure 2.8 b) shows the opposite tendency; The highest tensile residual stress is observed near the weld centerline and shifts compressive toward the base metal. The peak compressive stress is observed at $|x| = 40$ mm and gradually shifts back to zero with an increase in $|x|$. These tendencies agree with the distribution graphs plotted by other researchers, although the magnitude of the stresses differs because of the variables mentioned above [32]–[34]. Hempel *et al.* estimated that such residual stress distribution is because of the self-constraining geometry of the pipe [31]. As the structure has been welded, thermal contraction occurs on weld metal and adjacent base metal because of cooling. The circumferential contraction causes necking, leading to pipe wall bending. This bending state of axial residual stress significantly contributes to the tendency of residual stress distribution on the OD and ID. Additionally, axial contraction because of cooling adds tensile stress to the OD, accounting for the diminishment of compressive residual stress away from the weld. It must be noted that the welding residual stress distribution also depends on the circumferential angle (φ) between the welding start and welding direction.

2.3.1.3: Bending Residual Stress

Another source of axial residual stress on the pipeline is bending residual stress. As explained in the previous section, pipeline surface bending occurs during manufacturing, installation, and operations [17]. While bending during manufacturing and installation is

relatively predictable, the bending effect during operations such as geohazards is almost impossible to predict and measure. Figure 2.9 a) and b) show the through-thickness bending stress distribution on the pipeline during bending and after the bending moment is released, where D is the diameter of the pipe and σ_y is yield stress.

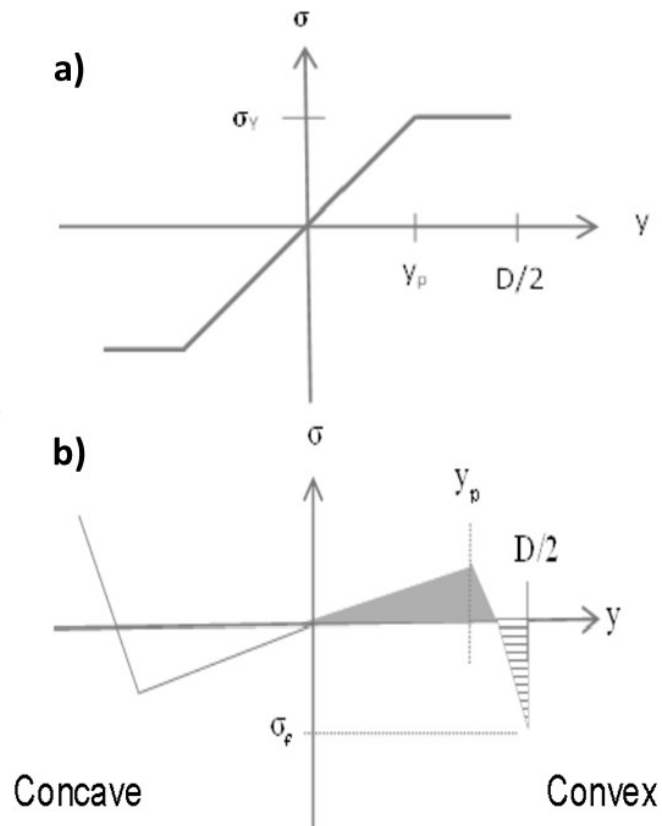


Figure 2.9 Stress profile from the concave side to the convex side a) for original bend and b) after springback [17]

As visible in Figure 2.9 a), the concave side exhibits a compressive stress gradient, as opposed to the convex side shows a tensile stress gradient. This residual stress distribution remains after the release of the bending moment so long as the pipeline is locked on both sides such that springback does not occur. However, if springback is allowed because of the

self-equilibrating feature of the material, the remaining internal moment must be cancelled out. As a result, a stress gradient from elastic recovery is added to the structure, resulting in the stress distribution shown in Figure 2.9 b). Figure 2.9 b) shows that the surface residual stress on the concave side becomes tensile to balance out the compressive residual stress in-depth and vice versa for the convex side.

2.3.1.4: Relaxation of Welding Axial Residual Stress Because of Bending

The relaxation of residual stresses may occur during the pipeline operation because of several factors. Hempel *et al.* experimented with the change in residual stress around the girth weld of pipeline steel before and after applying a four-point bending load through XRD and ND [35]. Figure 2.10 a) to b) shows the welding axial residual stress distribution on the outer surface after applying 182 MPa (50% of yield stress) and 337 MPa (90% of yield stress) of bending stress, respectively. As shown in Figure 2.10 a), stress relaxation caused by 182 MPa bending stress is negligible. However, 337 MPa bending stress decreased the compressive stress around the weld centerline and tensile stress at $|x| = 45$ mm, as visible in Figure 2.10 b).

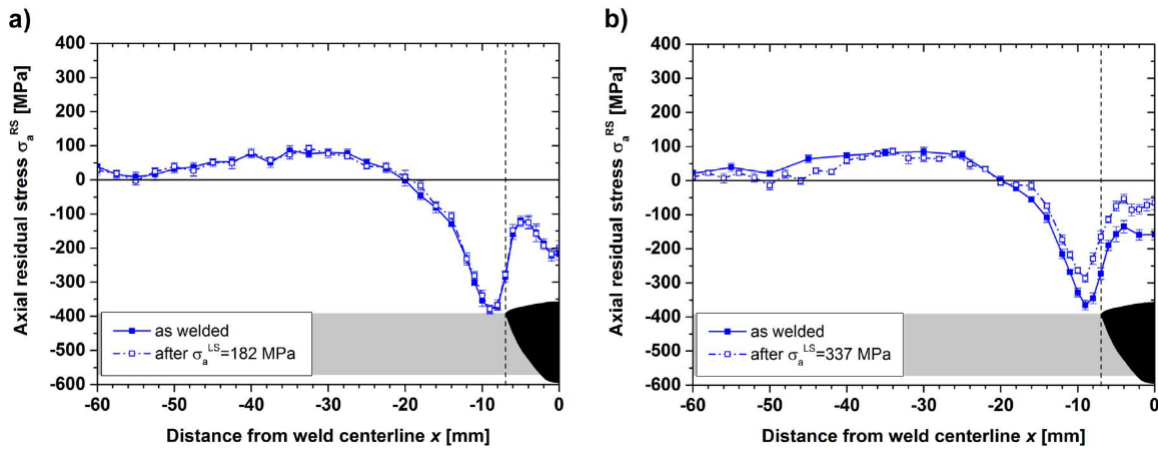


Figure 2.10 Change in axial residual stress distribution from WCL after applying a bending force of a) $\sigma_a^{LS} = 182 \text{ MPa}$ and b) $\sigma_a^{LS} = 337 \text{ MPa}$ [35]

Figure 2.11 a)-c) shows the axial residual stress distribution in the control sample, sample with 182 MPa bending stress, and sample with 337 MPa bending stress, respectively.

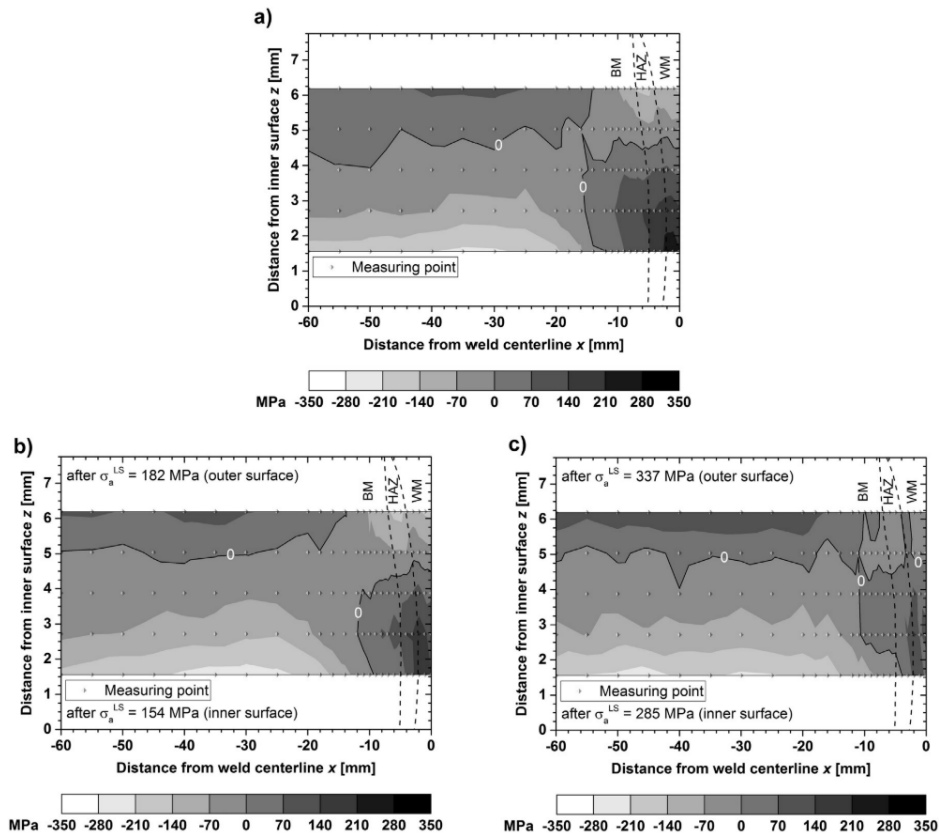


Figure 2.11 Axial residual stress gradient over the length and depth of a pipe from WCL of girth weld a) before applying bending force, b) after applying $\sigma_a^{LS} = 154$ MPa and c) $\sigma_a^{LS} = 337$ MPa on the OD [35]

Comparison between Figure 2.11 a) and b) shows no significant difference in the residual stress distribution except for the weld root on the inner surface. On the other hand, a comparison between Figure 2.11 a) and Figure 2.11 c) shows a significant change in the residual stress around the weld centerline near the inner and outer surfaces. Furthermore, the extension of tensile residual stress near the outer surface is observed.

These observations indicate that the interaction between welding residual and bending stress causes residual stress relaxation and redistribution. This phenomenon can be explained using the von Mises yield criterion. The von Mises equivalent stress (σ_{vM}) used for this criterion is calculated as follows:

$$\sigma_{vM} = \sqrt{\frac{1}{2} \left[(\sigma_r^{RS} - \sigma_\phi^{RS})^2 + (\sigma_\phi^{RS} - (\sigma_a^{RS} + \sigma_a^{LS}))^2 + ((\sigma_a^{RS} + \sigma_a^{LS}) - \sigma_r^{RS})^2 \right]} \quad (10)$$

σ_r^{RS} , σ_ϕ^{RS} and σ_a^{RS} in Equation (1) are radial, hoop, and axial residual stress, respectively. σ_a^{LS} is the applied bending stress. Figure 2.12 a) to b) shows the correlation between von Mises equivalent stress distribution and change in residual stress on the outer surface with $\sigma_a^{LS} = 182$ MPa and $\sigma_a^{LS} = 337$ MPa, respectively.

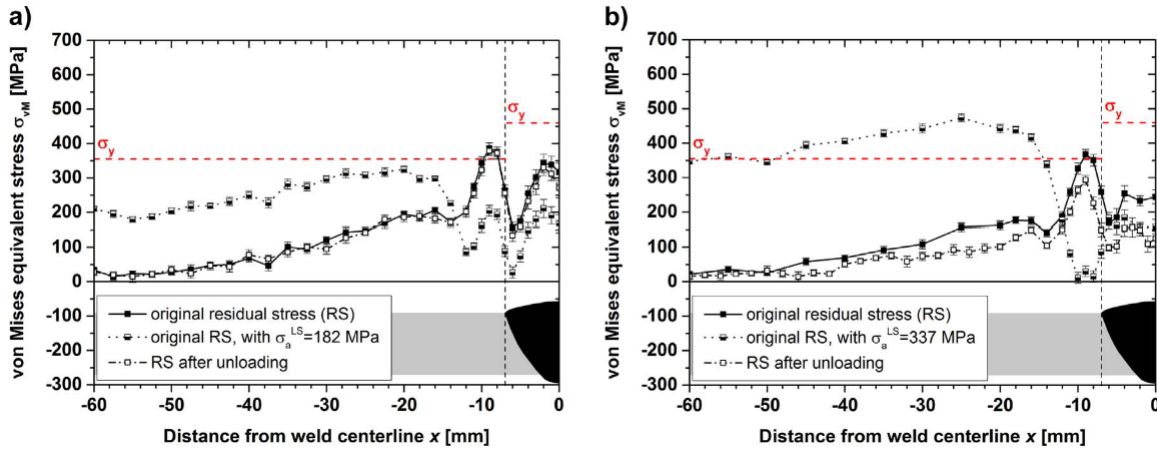


Figure 2.12 Von Mises equivalent stress on the outer surface a) before and after applying $\sigma_a^{LS} = 182$ MPa, b) before and after applying $\sigma_a^{LS} = 337$ MPa [35]

As shown in Figure 2.12 a), σ_{vM} does not exceed yield stress (σ_{ys}) at any measured points except for the weld root, resulting in no stress relaxation. On the contrary, Figure 2.12 b) shows σ_{vM} exceeding σ_{ys} for $14 \text{ mm} < |x| < 50 \text{ mm}$, leading to the stress relaxation within

the corresponding areas. The author compared this result with Figure 2.12 b) and concluded that the stress relaxation effect in an axial direction is significant for $40 \text{ mm} < |x| < 50 \text{ mm}$. The author also stated that the stress relaxation observed near the weld centerline can be attributed to the residual stress relaxation on and near the inner surface. In conclusion, such stress relaxation and redistribution may occur during the pipeline operations, influencing the initiation and early growth of C-NNpHSCC.

2.3.1.5: Relaxation of Welding Axial Residual Stress Because of Sectioning

One of the challenges in measuring welding residual stress and its effect on SCC is the stress relaxation effect after the sectioning process. Hempel *et al.* cut the girth-welded pipe of the austenitic steel X6CrNiTi18-10 with a wall thickness of 7.5 mm into quarter pipes and 6 mm width strips [31]. They measured the residual stress distribution from the weld centerline on each sample with XRD and ND to investigate the residual stress change after sectioning. Figure 2.13 shows the axial residual stress distribution on the outer surface of the specimen before and after sectioning [31].

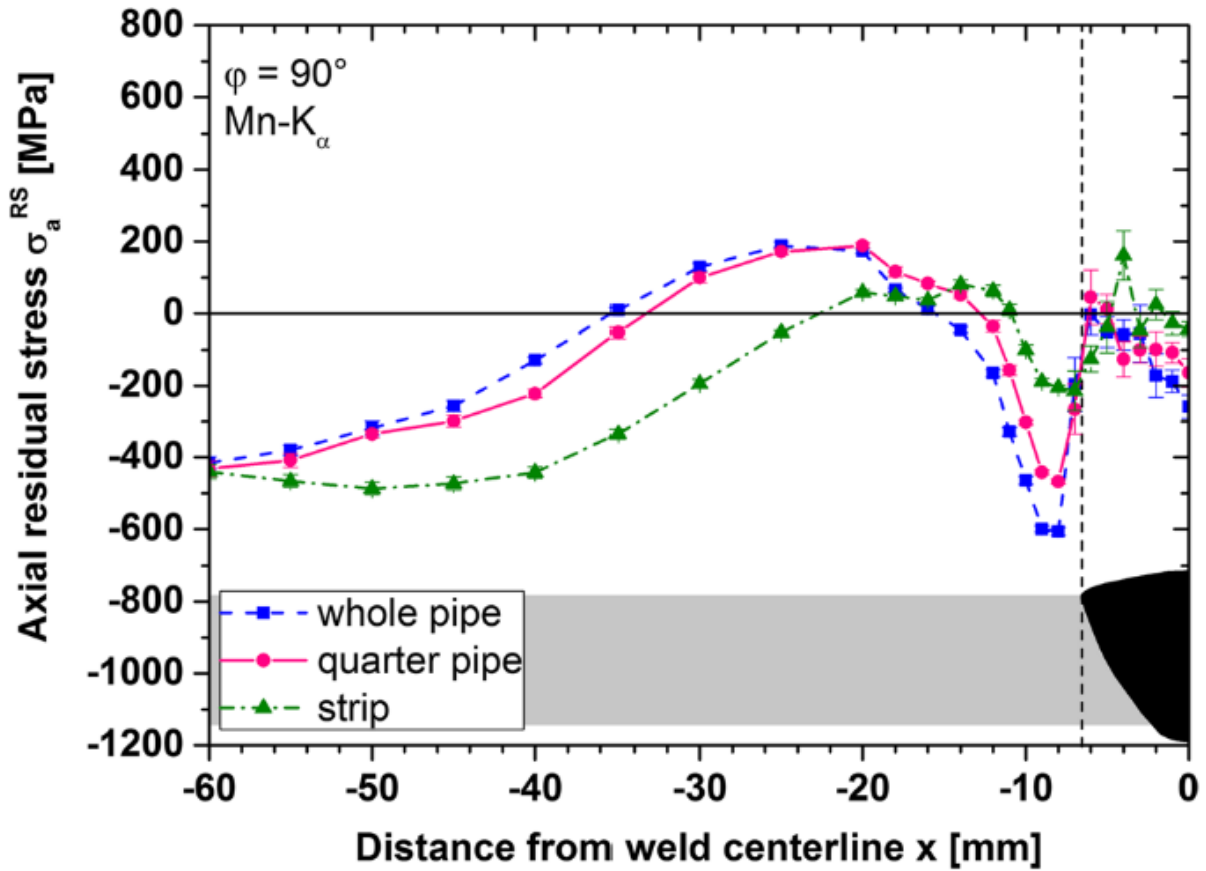


Figure 2.13 Axial residual stress distribution from WCL on whole pipe, quarterly sectioned pipe, and 6 mm width strip sectioned from a quarter pipe [31]

Figure 2.13 shows little change in the axial residual stress near the weld toe before and after sectioning into quarter pipes. However, the residual stress distributions in the other areas are nearly identical. This result is accounted for by the slight change in surface geometry before and after cutting into quarter pipes, showing a minor release of axial strain. On the contrary, the 6 mm strip exhibits significantly different axial residual stress distribution compared to the whole and quarter pipes. In detail, the absolute value of compressive stress at the weld toe decreased by 500 MPa. Furthermore, at $20 \text{ mm} < |x| < 55 \text{ mm}$, residual

stress distribution shifting downward was observed, resulting in a narrower tensile zone at $12 \text{ mm} < |x| < 20 \text{ mm}$. The effect of sectioning eventually diminishes at $|x| > 60 \text{ mm}$. The axial strain release after sectioning can account for this shift in the axial residual stress. As shown in Figure 2.14, the surface profile on the outer surface of the base metal shifted downward after sectioning. It into 6 mm strips [31]. The authors concluded that this massive release of axial strain is attributed to the significant contribution of bending components to axial welding stress.

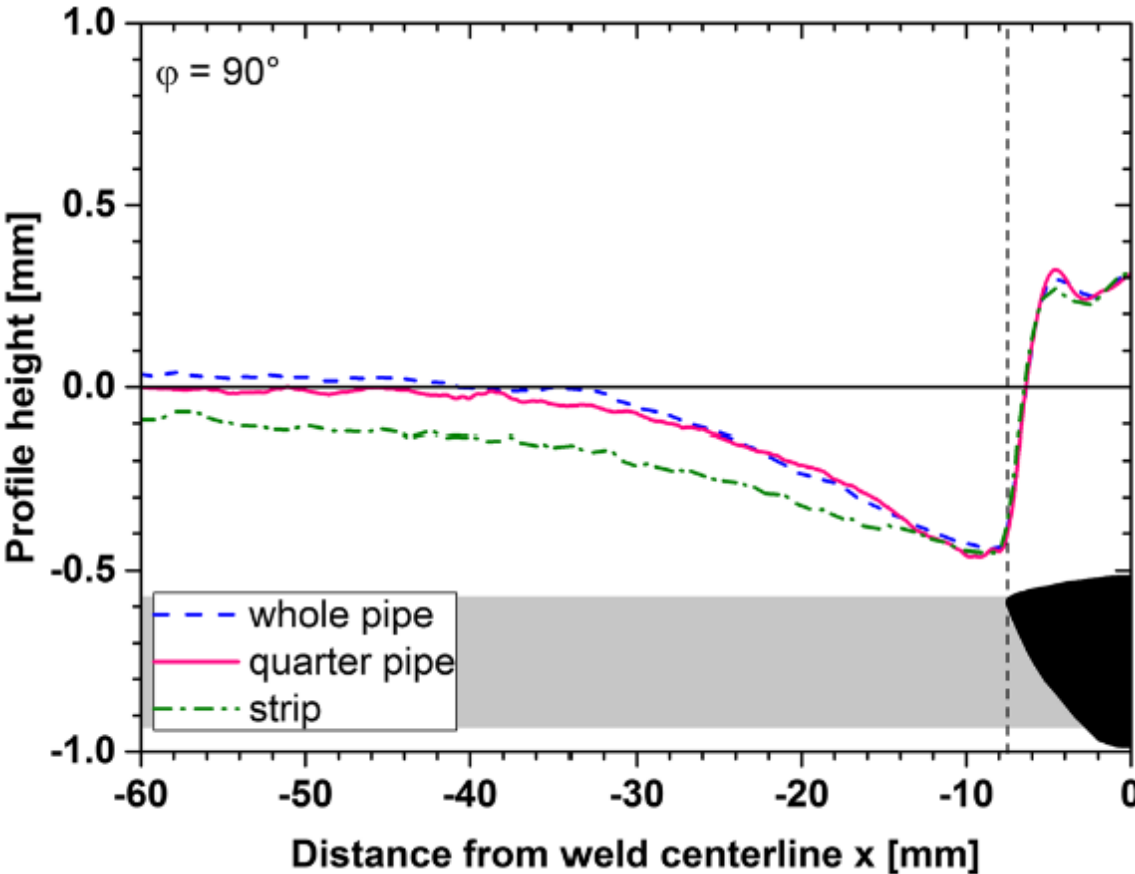


Figure 2.14 Surface profiles at $\phi = 90^\circ$ on the outer surface of a girth welded pipe before and after sectioning [31]

As mentioned above, welding residual stress distribution is influenced by the dimensions of the pipeline. Indeed, Song *et al.* found out that which stress component governs the welding residual stress is primarily determined by the thickness (t) and radius-to-thickness ratio (r/t) [27]–[30]. As shown in Figure 2.15, welding residual stress can be decomposed into three components: membrane, bending, and self-equilibrating [26]. For welding axial stress, the membrane component is generally negligible.

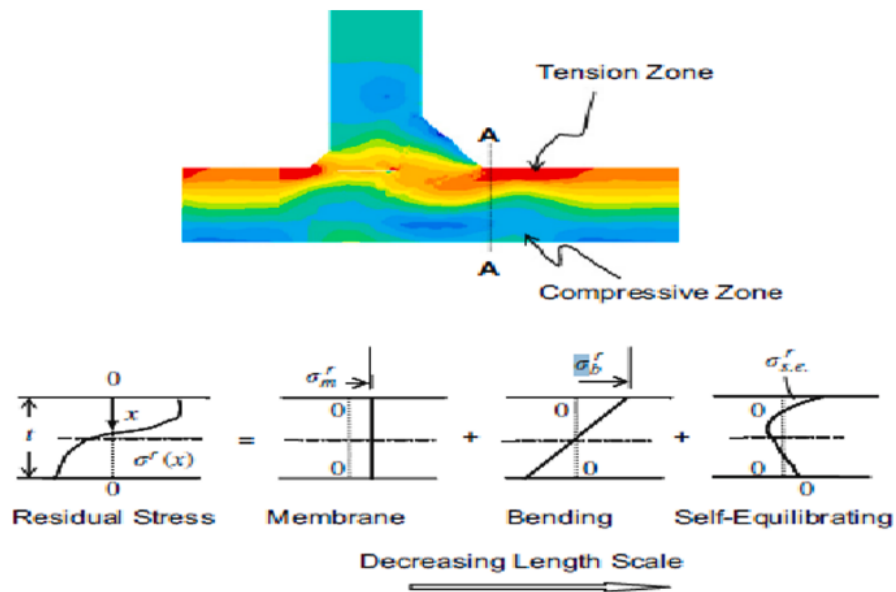


Figure 2.15 Three components of welding residual stress derived by residual stress decomposition technique [26]

As shown in Figure 2.16, the bending component of axial residual stress decreases with an increase in r/t and vice versa for the self-equilibrate component [30]. This indicates that the component geometry primarily influences the significance of axial strain relaxation. As such, one must consider these factors when performing lab-scale tests.

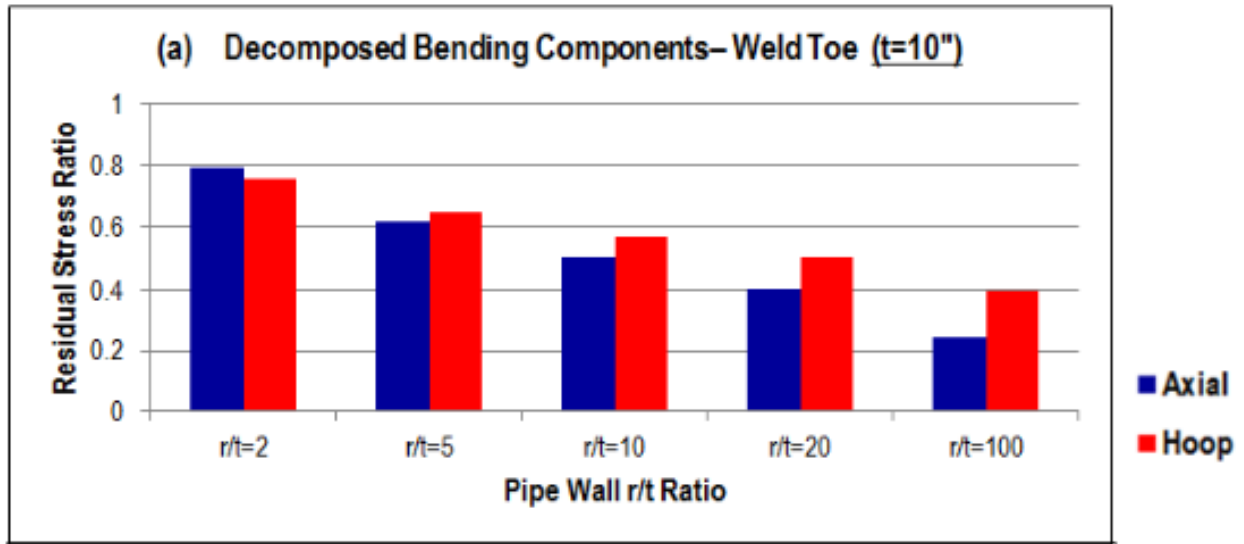


Figure 2.16 Change in bending component of the hoop and axial residual stress with an increase in r/t ratio [30]

2.3.1.5: Relaxation of Residual Stress Because of Cyclic Loading

As discussed in the later section, oil and gas pipelines are subjected to cyclic loading because of internal pressure fluctuations during the operation. As such, just as the effect of bending stress discussed above, the effect of cyclic loading on residual stress distribution must be considered. Van Boven *et al.* applied tensile cyclic loading on tensile specimens in air [7]. As illustrated in Figure 2.17 a) and b), They measured the residual stress distribution in gauge and thickness directions on the specimens before and after the tests through the neutron diffraction (ND) method to investigate the interaction between the effect of cyclic loading on residual stress distribution [22].

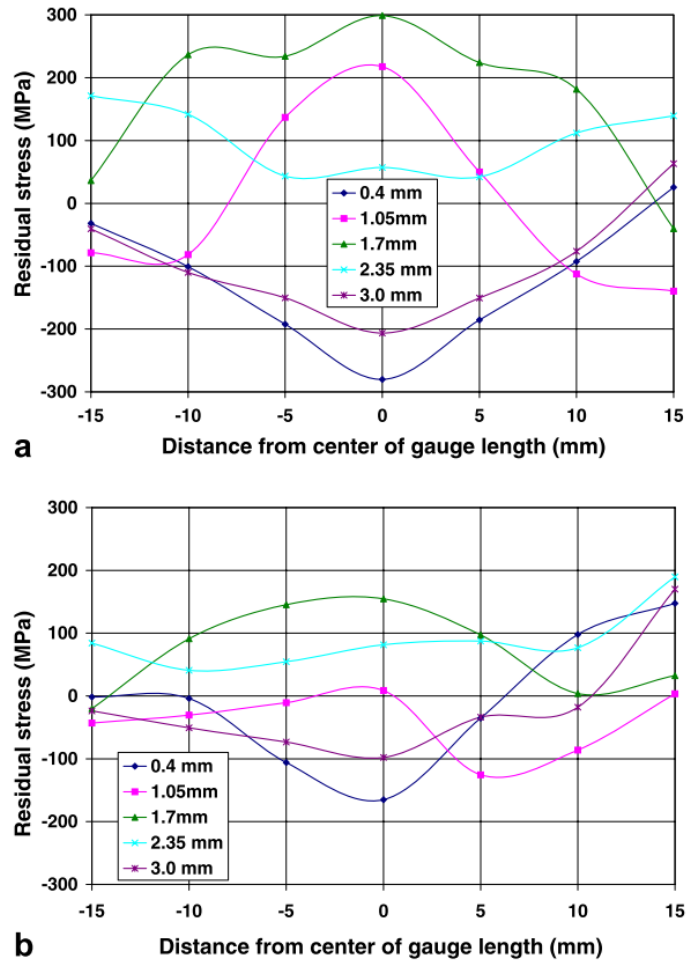


Figure 2.17 Residual stress distribution measure by ND on a tensile specimen a) before and b) after tensile cyclic loadings [22]. Distances from the outer surface are shown in legends.

As a result, they confirmed that cyclic loading has decreased both the maximum value of residual stresses and the sudden variations of residual stresses in the gauge length and thickness directions [7]. Chen *et al.* pointed out that this change in residual stress occurs

after a few cycles [22]. As such, the effect of cyclic loading may extend to the initiation and Stage I growth of NNpHSCC, where residual stress has an important role.

2.3.1.6 Residual Stress in SCC Colonies

Beavers *et al.* discovered that SCC colonies exhibit higher residual tensile stress than the area with no SCC, as shown in Figure 2.18 [36].

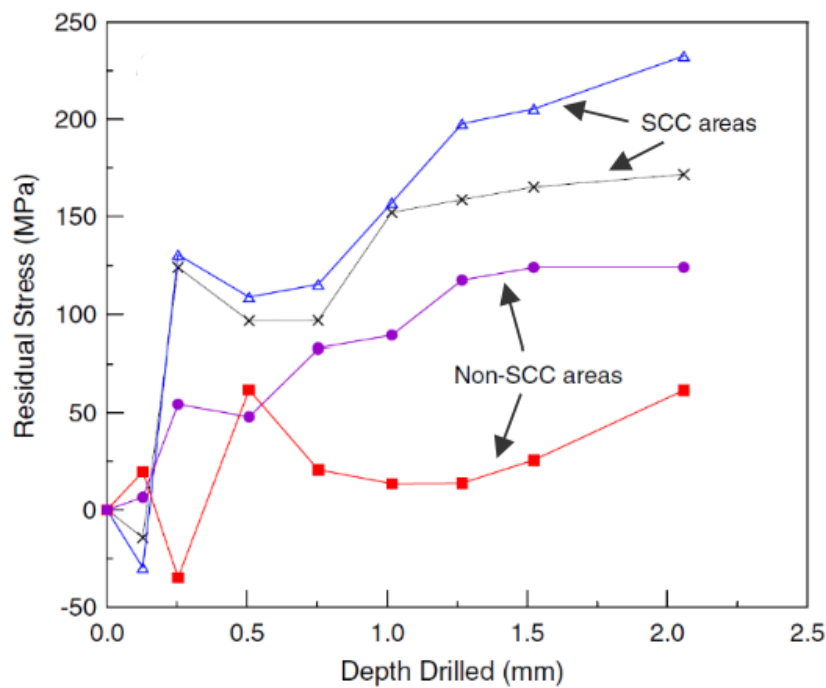


Figure 2.18 Residual stress distribution toward the inner surface of pipeline steel at and away from SCC colonies, measured with hole drilling method [36]

Although the surface residual stress ($x = 0$ mm) shows no differences, the near-surface residual stress at SCC colonies shifts to compressive, whereas the stress at non-SCC areas becomes tensile. However, toward the inner surface, the residual stress in SCC areas steeply shifts to tensile, whereas the stress in non-SCC areas either shifts to compressive or

increases to a lesser degree than in SCC areas. Since, as discussed in the previous section, crack growth requires a tensile residual stress gradient, it can be concluded that the SCC colonies are precursors of crack growth in the NNpH environment.

2.3.2 Applied Axial Stress

2.3.2.1 Internal pressure

Because of the internal pressure during operation, pipelines in service experience hoop and axial stresses [3]. Since these stresses contribute to the initiation and growth of NNpHSCC the most, pipes and operating factors are designed such that the resultant stresses do not exceed the value determined by standards such as CSA Z662 [37]. The maximum axial stress exerted on the pipeline is ~50% of hoop stress and can be expressed as follows:

$$S = \frac{PD}{4t} \quad (11)$$

Where P is operating pressure, D is the outer diameter of the pipe, and t is wall thickness. It must be noted that the difference between the hoop and axial stresses from the internal pressure is believed to be the reason why circumferential cracks are rarely observed in the NNpH environment [3].

2.3.2.2 Thermal Stress

Another external stress comes from the thermal expansion of pipeline steel caused by the change in temperature during the operation [3][17]. This is caused by the difference in temperature at the time of pipeline installation and during the pipeline operation. Thermal expansion and exertion of tensile stress on the outer surface occur when the operating temperature is lower than the initial temperature, and thermal contraction and compressive

stress occur in the opposite condition. The magnitude of this stress is expressed by an equation as follows [17]:

$$\sigma_T = \alpha(T_1 - T_2) \tag{12}$$

Where σ_T is the axial stress from the temperature change, α is the coefficient of thermal expansion ($1.1 \times 10^{-6}/^\circ\text{C}$ for steel), and T_1 and T_2 are the pipeline temperatures at the time of installation and in operation, respectively. E is the elastic modulus (207 GPa for steel). A typical example is the pipeline installed at 55°C and operated at 10°C , which yields $\Delta T = 45$. As shown in Figure 2.19, this temperature difference increases the total axial stress up to 37% SMYS while maintaining the magnitude of hoop stress [17].

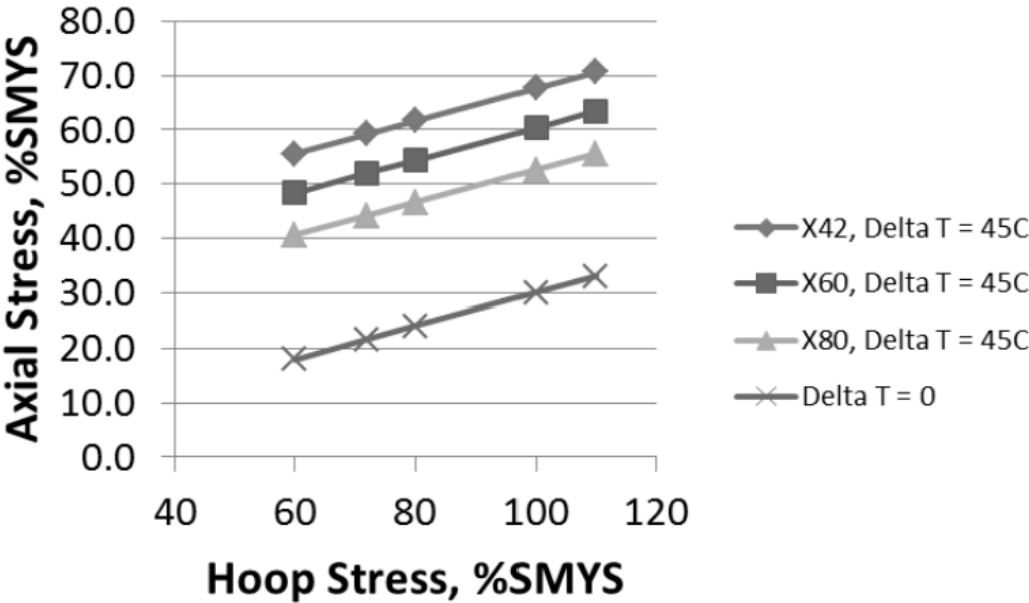


Figure 2.19 Change in axial stress in various pipeline steels by temperature change [17]

Other sources of external axial stress are soil movement, the hydrodynamic force from oil at the elbow, and the Bourdon Effect at the elbow. In addition to these external stresses,

axial residual stresses also have a crucial role in the initiation and growth of C-NNpHSCC, which is explained in detail in the next section.

2.3.2.4 Soil Movements

Geological hazards may exert circumferential and axial stress on pipes, contributing to pipeline failure. Frequently observed stresses caused by geological factors are shear stress applied by landslides, bending stresses induced by either settlement or earthquake and overburdened pressure applied by soil layers above the pipe. Since the frequency of these geological hazards and the numerical value of stresses yielded depend on numerous factors, it is difficult to predict the effect of these factors on NNpHSCC.

2.3.2.5 Bourdon Stress

The major applied stresses contributing to the initiation and growth of NNpHSCC have been believed to be the three factors mentioned above. However, Shirazi *et al.* noted that Bourdon stress may also influence crack growth [38]. When a bend experiences internal pressure, it may straighten out because of the Bourdon effect [39]. This effect occurs depending on the bend's stiffness and surrounding constraints. The intrados and extrados of the pipe elbow have different surface areas, which creates an outward resultant force. This unbalanced thrust force can cause high stress levels on the pipe wall and deformations that can impact the pipeline.

2.3.2.6 Hydrodynamic Stress

Shirazi *et al.* stated that the influence of hydrodynamic stress on NNpHSCC is likely [38].

Fluid flowing through a bend in a pipe causes changes in momentum, resulting in the application of hydrodynamic stresses at the bend. The author used an impulse-momentum equation to calculate the resultant force on a pipe bend and concluded that the effect is likely significant. However, further research is required to evaluate the significance of this stress in detail.

2.4 Materials

It is known that every pipeline steel is susceptible to NNpHSCC [3]. Although the effect of metallurgical factors, such as microstructure, mechanical properties, and chemical compositions, on the significance of NNpHSCC is complex, it is generally acknowledged that the microstructure somewhat affects the susceptibility of steel to NNpHSCC. Kushida *et al.* investigated the effect of microstructure on NNpHSCC by conducting cyclic loading tests on the notched specimens with different microstructures in NNpH solution [40]. As a result, it was found that the non-uniform ferrite-pearlite microstructure was more susceptible to NNpHSCC than uniform bainite or bainitic-ferrite microstructures. They concluded that such susceptibility was because of the plasticity of the ferrite-pearlite microstructure that accelerated HE. In another study, Chen *et al.* investigated the correlations between microcrack initiation and ferrite-pearlite microstructure of X-65 pipeline steel by applying cyclic loading in NNpH solution [41]. It was found that preferential dissolution occurs along the ferrite-pearlite banded structure observed in the middle section of pipeline steel, leading to the initiation of microcracks. This is because the galvanic couple formed between pearlite and ferrite accelerates anodic dissolution. This non-uniform ferrite-pearlite microstructure is also observed in heat affected zone (HAZ)

adjacent to the weld toe. Fang *et al.* conducted a slow strain rate test (SSRT) on the specimens fabricated from a welded pipe in NNpH solution and found that HAZ was most susceptible to NNpHSCC compared to the base metal and weld metal [5]. It was concluded that this is because of both microstructure and high residual stress in HAZ. While SSRT does not represent the entire mechanism of NNpHSCC [4], it is believed that the galvanic effect in the microstructure is responsible for the difference in the susceptibility to NNpHSCC between HAZ and base metal. The detail of weld-induced residual stress is explained in the later section. As such, it can be concluded that the pipeline steel with non-uniform ferrite-pearlite microstructure is mechanically and chemically susceptible to NNpHSCC.

The presence of non-metallic inclusions also contributes to the initiation of microcracks. Liu *et al.* conducted SSRT on X70 pipeline steel with different types of inclusions to investigate the effect on SCC [42]. Crack initiations were observed at Al-rich inclusions because of their brittleness and incoherency to the metal matrix, whereas no crack initiations occurred at Si-rich inclusions.

2.5 Mechanisms of NNpHSCC

NpHSCC is commonly referred to as SCC; however, it is a failure resulting from localized corrosion and corrosion fatigue [4]. The growth stage of NNpHSCC can be divided into four phases, as illustrated in Figure 2.20: initiation, Stage I growth, Stage II growth and Stage III growth [43].

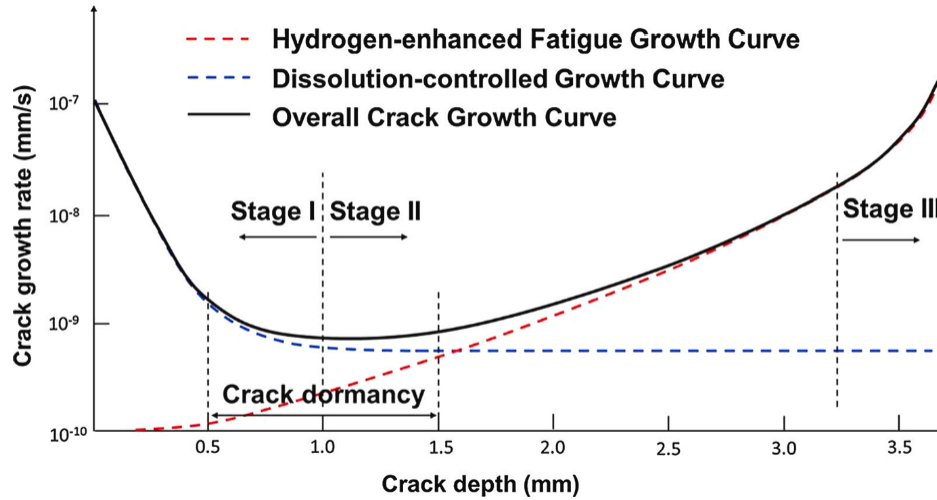


Figure 2.20 Bathtub model for NNpH stress cracking [43]

After the initiation of crack growth from corrosion pits or surface scratches, the growth stage of NNpHSCC can be broken down into three phases, as shown in Figure 2.20 [43]. Anodic dissolution and tensile stresses dominate the initiation and Stage I growth, including residual and applied stresses. Corrosion fatigue, facilitated by hydrogen embrittlement, is the dominant factor in Stage II growth. Stage III is unstable crack growth, leading to material rupture. This section provides a detailed explanation of the mechanisms of each stage of NNpHSCC.

2.5.1 Initiation and Stage I Growth of NNpHSCC

Like an ordinary SCC, the initiation and early growth of NNpHSCC require three factors: tensile stress, corrosive environment, and susceptible material. Literature shows that several sources contribute to the emergence of tensile stress on the outer pipeline surfaces [38]. These include but are not limited to internal pressure during operations, changes in the temperature, bending caused by geohazards, dent on the surface caused by rocks, unstable

soil movement, and manufacturing processes such as welding [4][38]. A corrosive environment can be divided into electrolyte, coating, and CP [3]. As mentioned in section 2.2.1, the electrolyte is the dilute bicarbonate solution with a high concentration of CO₂ that diffuses from the surrounding soil containing decaying organic components [3]. Pipeline surfaces are coated to safeguard the metal substrate against corrosive electrolytes.

However, there is a possibility of the coating detaching from the metal surface because of external factors. Coating disbondment during pipeline operations can have various causes, such as soil stress because of soil movement, pipe surface damage resulting in wrinkles and dents, and coating degradation caused by high operating temperatures [11]. In addition, coating discontinuity can happen when applying it to a pipeline surface. This can be in the form of a "holiday," a gap typically forming around the weld toes and overlapped coating area [3]. Afterward, the groundwater infiltrates the disbonded region. It comes into contact with the metal substrate, which starts the steel's anodic dissolution and the water's cathodic reduction, as outlined in section 2.2.1.

CP is a method to prevent metal corrosion by applying a negative potential to the surface through a cathodic current. However, it may not be effective because of environmental factors that affect conductivity, such as moist clay and holidays with groundwater.

Excessive cathodic current can cause hydrogen evolution, leading to coating disbondment and crack growth. Although the initiation of NNpHSCC commonly occurs because of anodic dissolution, the detailed sources and mechanisms vary. Typical initiations are caused by dissolution at surface discontinuities such as scratches, grooves, and mechanical dents [44]. Metallurgical defects such as grain boundaries, inclusions, and voids become

preferential corrosion sites, leading to the initiation of microcracks. It must be noted that preferential dissolution also occurs at banded structures typically observed in pipeline steels. Because of stress corrosion, localized corrosion pits are often the starting point for cracks. These pits can be caused by stress corrosion cells, formed by residual stress differences. Galvanic corrosion cells between mill scale and base metal can also contribute to the formation of corrosion pits and subsequent crack initiation [8][9]. The schematic of these mechanisms is briefly summarized in Figure 2.21 [15].

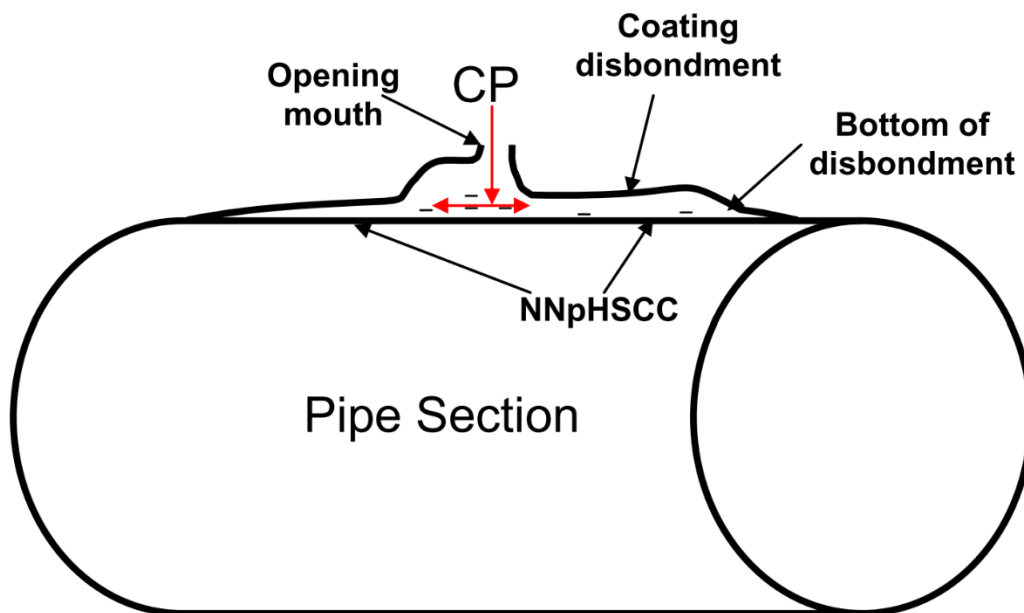


Figure 2.21 Schematic of NNpHSCC initiation from coating disbondment [15]

Because no passive film is formed in the NNpH environment, the resultant pits have a high length ratio over depth, as shown in Figure 2.22 [4].

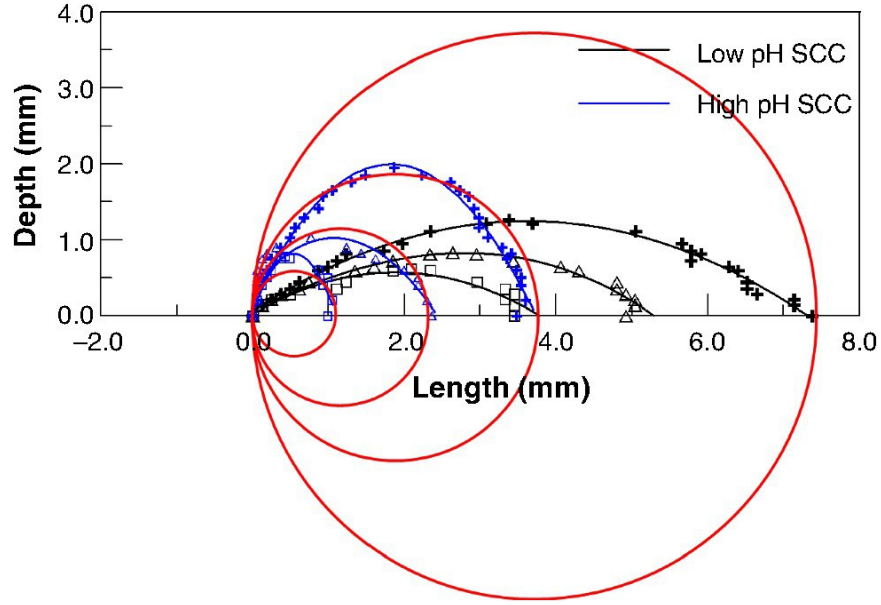


Figure 2.22 Crack length-depth profiles of near-neutral pH SCC and high pH SCC [4]

With these initiation sites and high continuous tensile stress, the sum of both operating and residual stresses at the subsurface, microstructurally short cracks may be initiated. The crack growth rate (da / dt) (mm / s) in this stage is expressed by the equations as follows [43]:

$$\frac{da}{dt} = \begin{cases} e^{-\frac{a}{m}} \times r, & a \leq 1.0 \text{ mm} \\ h, & a > 1.0 \text{ mm} \end{cases} \quad (13)$$

h , r , m , and c in the equations above are the crack growth rate in Stage II growth, crack growth rate by anodic dissolution along the pipeline surface, a fitting parameter, and half crack length, respectively.

As shown in Equation (13), the crack growth rate in Stage I exponentially decreases as the depth of cracks increases. This is because of the reduction in the anodic dissolution rate at the bottom of the cracks because of the localized change in pH of the solution involved

with the gradient of CO₂ and variation of ionic concentrations [4][38]. As such, static tensile stress at the bottom of pits becomes dominant to crack growth. Microcracks propagate until they reach a certain length, usually between 0.5 mm and 1.0 mm, shifting from active to dormant. This is because of the self-equilibrated nature of macro-scale residual stress (Type I stress) near the tip of dormant cracks. The net sum of Type I residual stress throughout the structure must be zero [38]. As such, if the high tensile residual stress is present at or near the outer surface, the residual stress tends to decrease with increased depth from the outer surface. This indicates that the magnitude of residual stress may become compressive toward the inner surface, leading to the loss of driving force for Stage I growth. However, residual stress relaxation and redistribution because of crack initiation and propagation must not be ignored, as these factors may affect the crack growth rate. To investigate these effects in detail, surface residual stress measurement before and after the crack initiation may be required.

Because of the decrease in the tensile residual stress at the crack tip, the crack tip blunting because of anodic dissolution occurs, and consequently, the crack becomes dormant. This morphology is evidenced by the typical balloon-shaped cracks found in the NNpH environment, one of which is shown in Figure 2.23 [45].



Figure 2.23 Blunted, the balloon-shaped crack propagated in the NNpH environment [45]

Chen. *et al.* discovered that the reactivation of these dormant cracks is impossible unless cyclic loading ($\Delta K > 0$) is applied, as shown in Figure 2.24 [46]. This interaction between the new driving force and reactivation of dormant cracks, also known as Stage II growth, is further discussed in the next section.

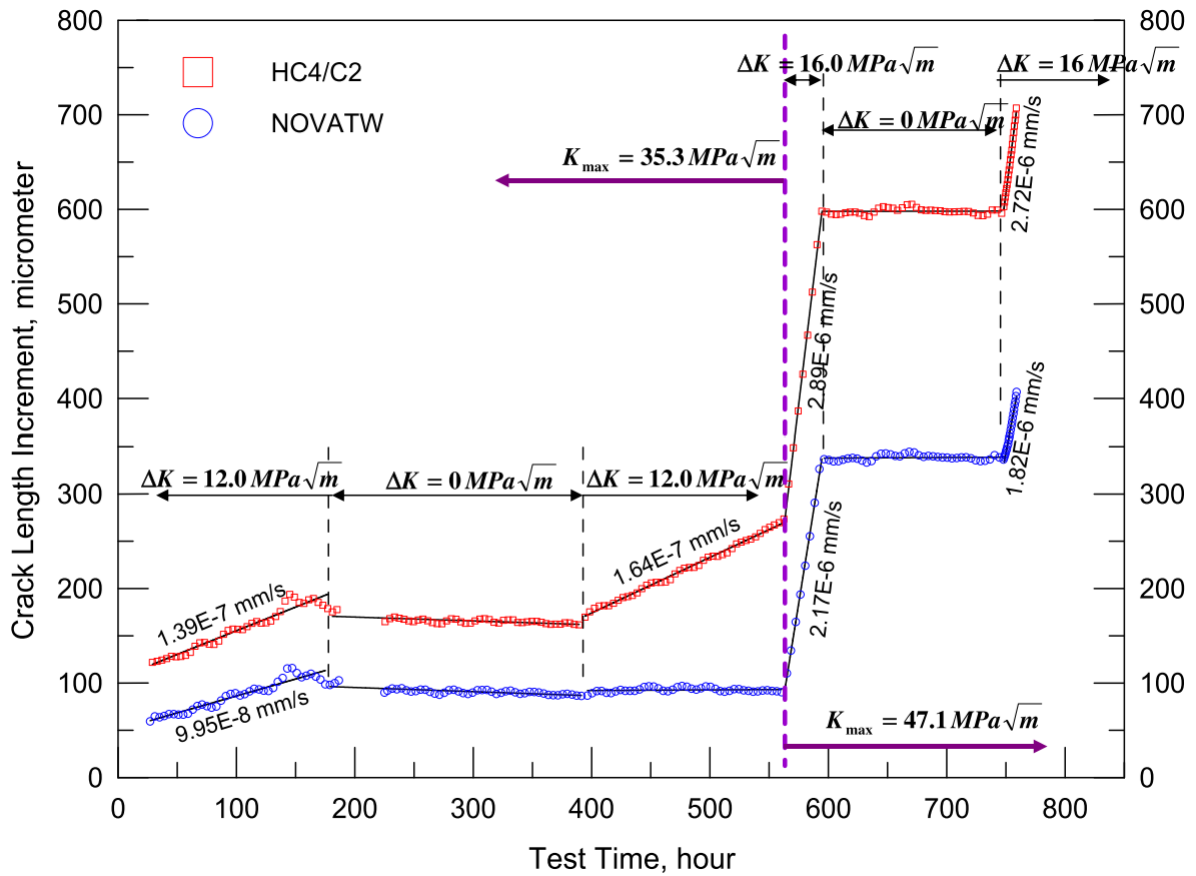


Figure 2.24 The increase in crack length over time in two NNpH solutions with cyclic loadings [46]

2.5.2 Stage II growth

As mentioned in the previous section, crack dormancy occurs because of the loss of driving forces: anodic dissolution and static tensile stress. As such, new driving forces are required to propagate the cracks further. This subsection explains the mechanisms of crack reactivation and growth and the factors influencing them.

2.5.2.1: Effect of Location-Specific Conditions on Crack Reactivation

As explained in the previous section, the reactivation of dormant cracks is influenced by location-specific conditions, one of which is macro-scale residual stress (Type I stress) near the tip of the cracks. The magnitude of residual stress in this area is a critical factor for reactivation, as mechanical driving forces govern Stage II growth [4]. Figure 2.25 demonstrates how residual stress near the crack tip affects crack reactivation and growth rate [4].

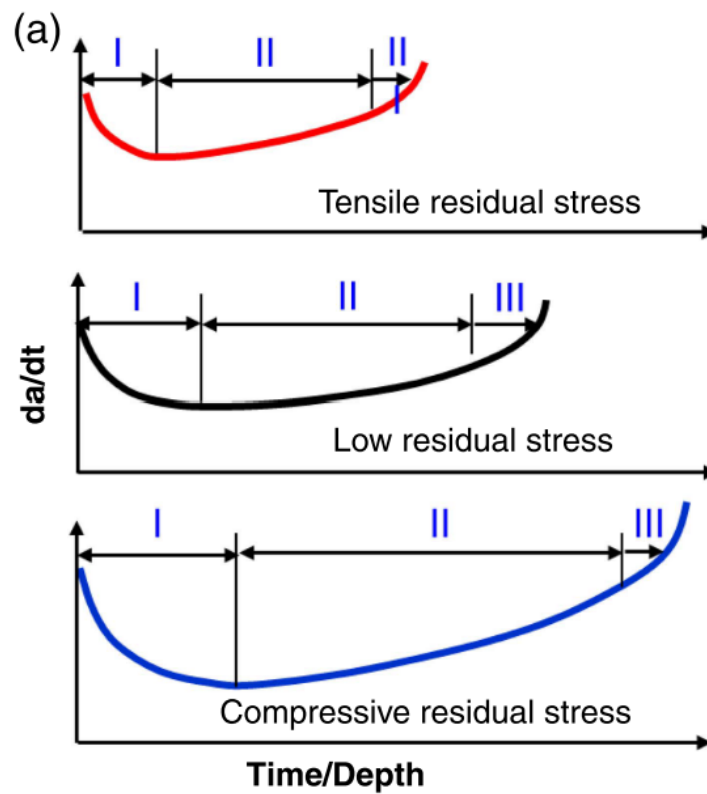


Figure 2.25 The effect of stress on the growth and dormancy of cracks [4]

As can be seen, high tensile stress shortens the duration of Stage I and crack dormancy. In contrast, the duration of Stage I and crack dormancy becomes longer as the residual stress shifts to compressive.

Another location-specific factor is the local diffusibility of hydrogen atoms to the cracking zones [46]. As explained in section 2.2, hydrogen atoms generated on the surface of pipeline steel and at the crack tip diffuse into the plastic zones of dormant cracks under cyclic loading, triggering the further growth of the cracks. These two factors interact, as high residual stress leads to more aggressive steel corrosion and enhanced hydrogel generation [46]. It is widely understood that only a small percentage, less than 5%, of the inactive cracks under cyclic loading meet the specific location requirements mentioned previously. Nonetheless, the reactivated cracks do not continuously expand until the pipeline ruptures. Instead, they undergo a repetitive cycle of dormancy and reactivation under cyclic loading. The schematic of this recurring cycle is illustrated in Figure 2.26 [47].

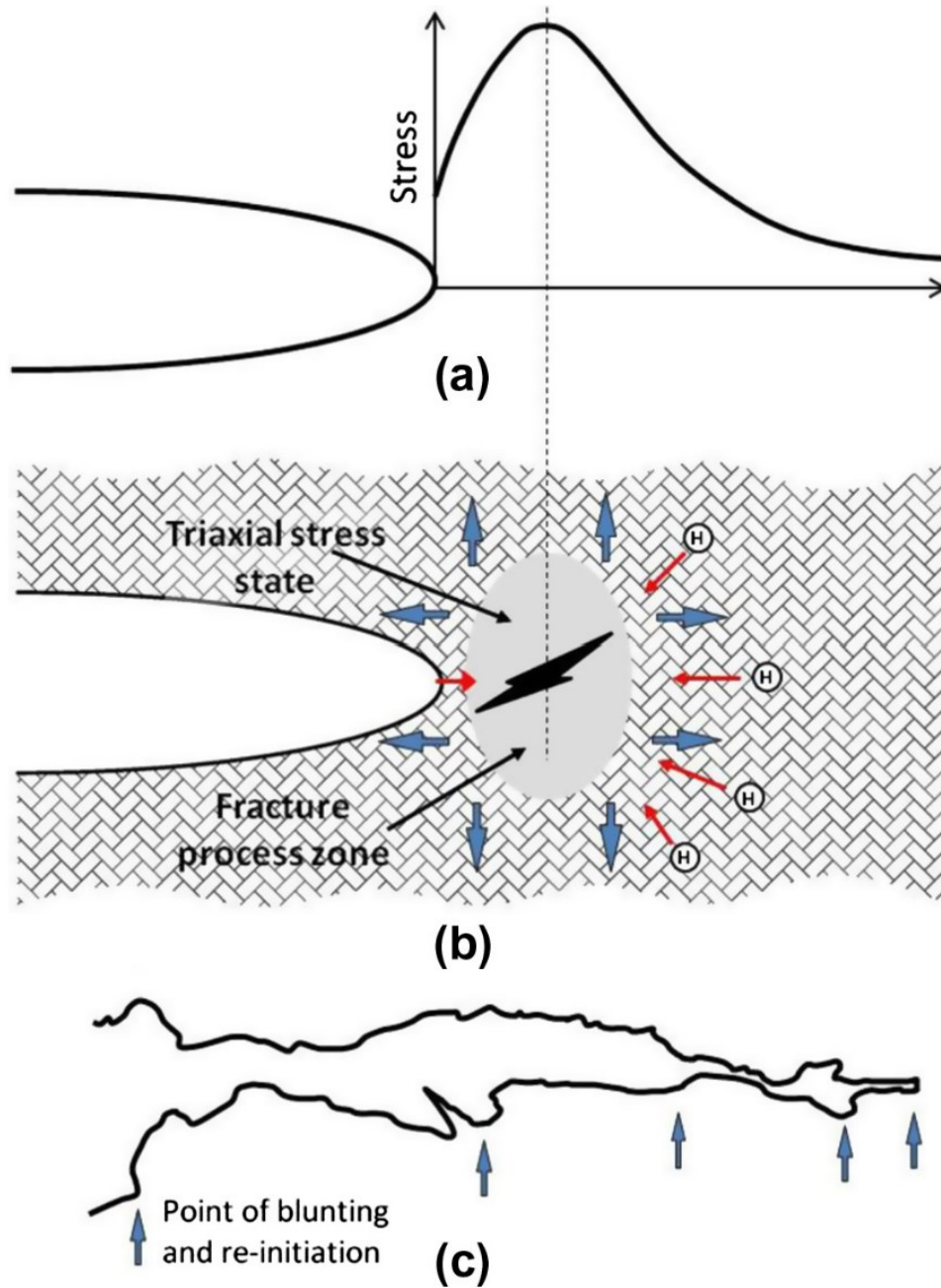


Figure 2.26 The mechanism of discontinuous crack growth: (a) Stress distribution ahead of the blunt crack tip, b) Triaxial zone at which HE and facilitated crack growth occurs, c)

The crack becomes blunted again and reinitiated [47]

2.5.2.2: Effect of Cyclic Loading on Crack Reactivation and Growth

As stated earlier, Stage II growth is mainly caused by cyclic loading. This type of loading comes from the fluctuating pressure that occurs internally during operation [3]. The crack growth rate can be calculated based on the corrosion fatigue model and expressed as a combined factor in the following equation [4]:

$$\frac{da}{dN} = A \left(\frac{\Delta K^\alpha K^\beta_{max}}{f^\gamma} \right)^n + h \quad (14)$$

A, n (= 2), α (= 0.67), β (= 0.33), and γ (= 0.033) in the combined factor above are all constants, and $\alpha + \beta = 1$. Although h represents the crack growth induced by anodic dissolution at the crack tip, the magnitude of this variable is significantly lower than the other factors [43]. Moreover, the dissolution of the anode at the tip and walls of the crack may blunt the crack, leading to the inhibition and cessation of crack propagation. Constant A takes into account several factors influencing Stage II crack growth, including the diffusion rate of hydrogen, hydrogen concentration in the material, and temperature. This constant can be expressed as [4]:

$$A = \left[\frac{4\sqrt{2.476}(1+\nu)\Omega}{3\pi k_B T \sqrt{2\pi \ln\left(\frac{1}{c_0}\right)}} \right]^{2n} \quad (5)$$

Where $N = 0.6n$, k_B is the Boltzmann constant, T is the temperature, ν is the Poisson's ratio, c_0 is the atomic ratio of H/Fe away from the crack tip, and Ω is the partial molar volume of the hydrogen atom.

Using Equation (14), Chen *et al.* investigated the crack growth rate in CT specimens in different NNpH solutions. They discovered that the data showed the least scatter if

normalized by $\Delta K^2 K_{\max}/f^{0.1}$ and that the threshold value of the combined factor in the C2 solution is 8500 $(\text{MPa}/\sqrt{\text{m}})^3/\text{Hz}^{0.1}$, as visualized in Figure 2.27 [48].

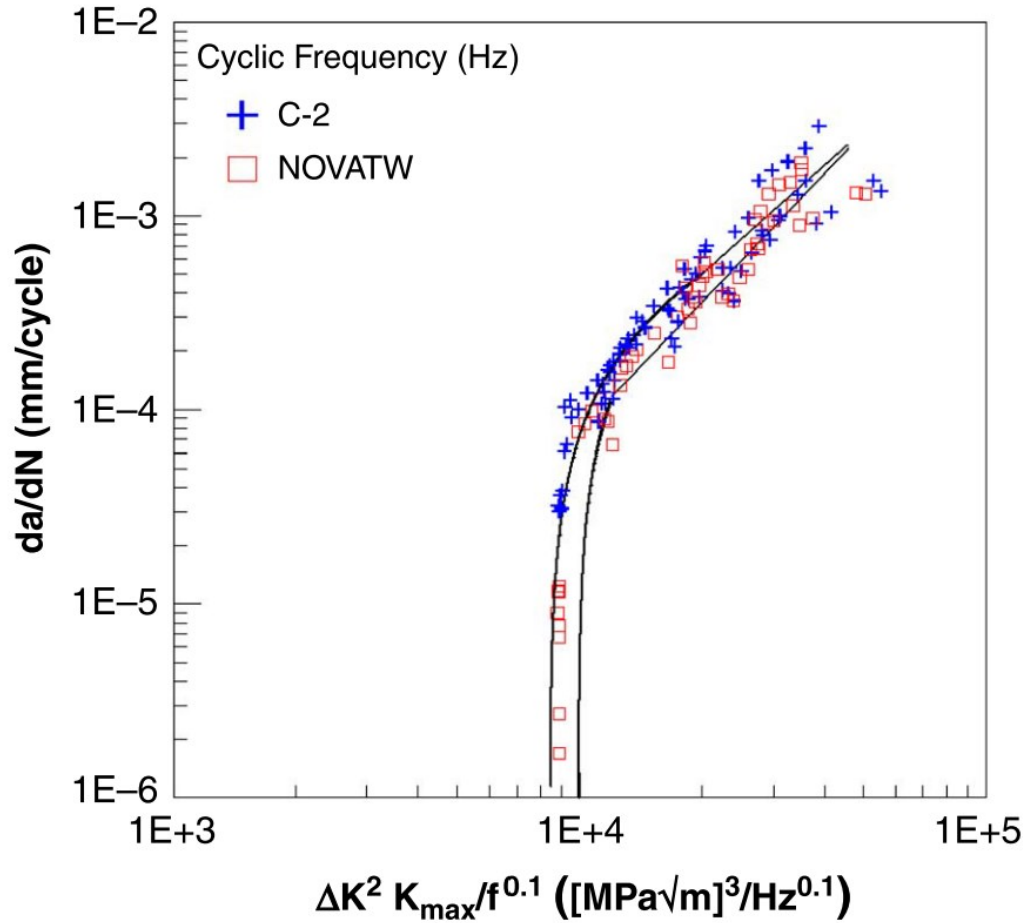


Figure 2.27 Crack growth rate (da/dN) as a function of combined factor in C2 and NOVATW solutions [48]

Hence, the modified equation for the crack growth rate in Stage II in response to this result is as follows [4]:

$$\left(\frac{da}{dN}\right)_{tot} = A \left(\frac{\Delta K^2 K_{max}}{f^{0.1}}\right)^N, f \geq f_{critical} \quad (16)$$

This equation can be separated into two factors: $\Delta K^2 K_{max}$, which is consistent with the Paris equation ($da/dN = c\Delta K^m$) and $f^{0.1}$, which represents enhanced crack growth by corrosion and becomes minimized by an increase in overall frequency. The frequency effect on Stage II crack growth is visualized in Figure 2.28 [49].

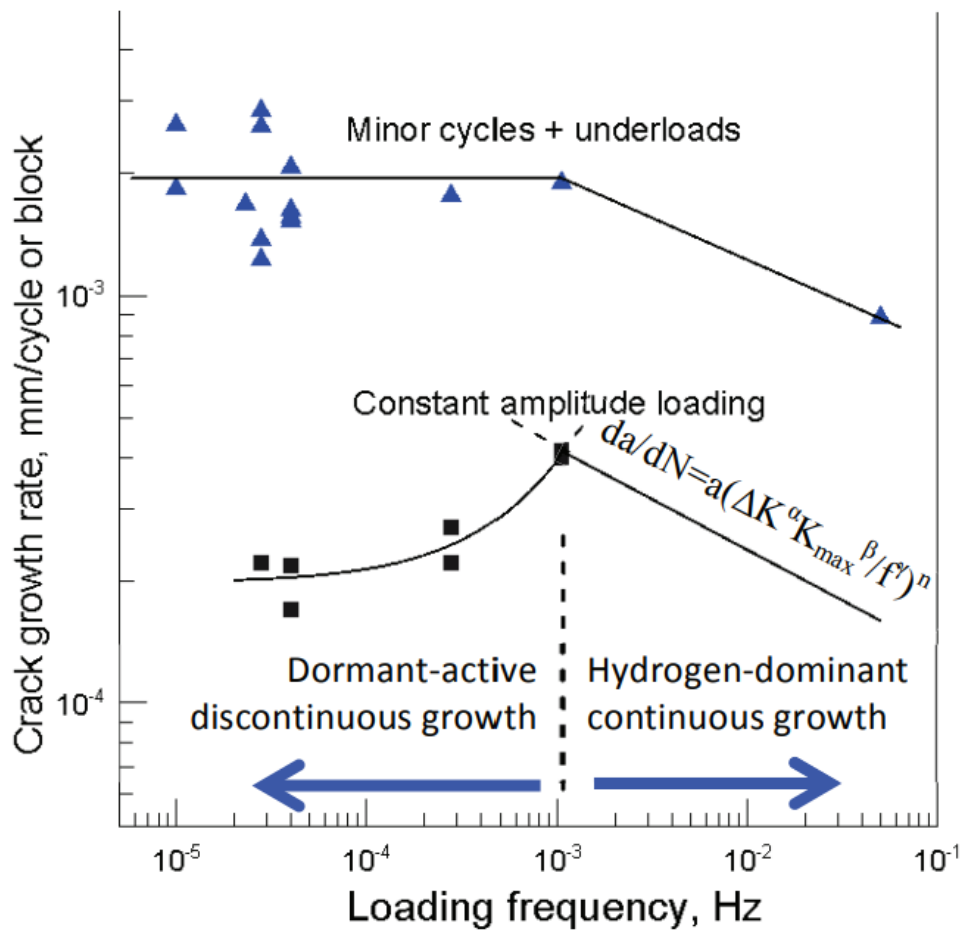


Figure 2.28 Crack growth rate and change in the mechanism of crack growth at different loading frequencies [49]

As can be seen, Stage II growth can be broken down into two parts. Up until the loading frequency reaches 10^{-3} Hz, the crack growth rate exponentially increases by the following equation [4]:

$$\frac{da}{dN} = 1.94 \times 10^{-4} + 0.204f \quad (17)$$

This is because of the crack growth mechanisms governed by the cycle of crack dormancy, reactivation and growth mentioned above. The crack growth mechanism shifts to hydrogen-dominant continuous growth once the loading frequency exceeds 10^{-3} Hz. The steep decrease in the crack growth rate results from fewer hydrogen atoms diffusing into the plastic zones ahead of crack tips because of the increased frequency.

Chapter 3 : Experimental Methods

In this chapter, the material used for the experiment, the design of lab-scale specimens, the methods to study the purpose of this research, the relationship between the shapes of pits and microcracks during the beginning and early stages of C-NNpHSCC and the existence of mill scale, residual stress induced by girth welding, and residual stress caused by bending on welded material are discussed.

3.1 Material and Specimen

3.1.1 Material

For this research, a 45.4 cm OD X52 pipeline with a thickness of 6.35 mm, as shown in Figure 3.1, has been selected.



Figure 3.1 X52 pipeline steel used for the experiment.

This pipeline had a girth weld, a longitudinal weld seam, and a coating on its surface.

Information on the service conditions and durations was not available. The geometry of the girth weld is shown in

Figure 3.2 a). The width of HAZ is approximately 2 mm, as shown in Figure 3.2 b).

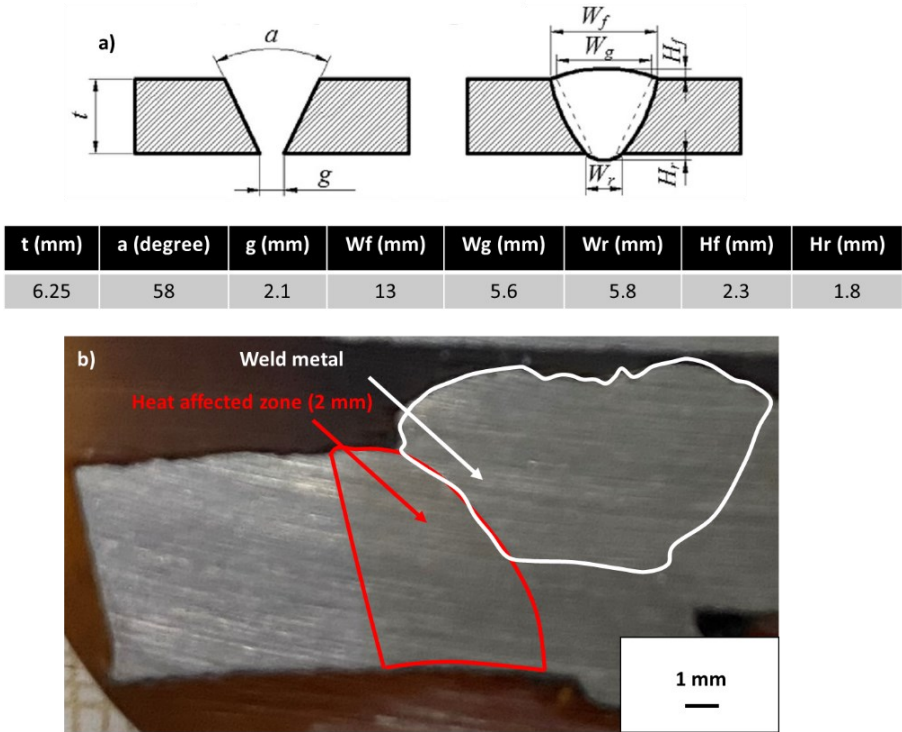


Figure 3.2 a) Geometry of single-V girth weld on the selected specimen and b) picture of weld metal and heat affected zone on the specimen.

3.1.2 Lab-Scale Specimen

Since this experiment only focused on the initiation and Stage 1 growth of C-NNpHSCC primarily governed by residual stress and localized corrosion, stick-shaped samples for static corrosion tests were designed and are shown in Figure 3.3.

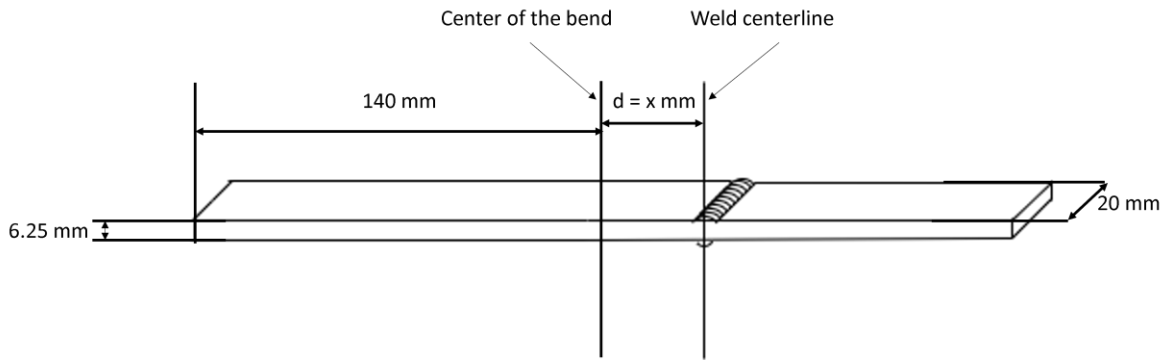


Figure 3.3 Schematic of a stick-shaped specimen

As mentioned in section 2.3.1, surface tensile weld residual stress on the OD typically shows its peak at $|x| = 30$ mm. However, welding residual stress varies with numerous factors. Since only a little information is available for the pipeline steel used in this research, it is impossible to estimate the magnitude of the welding residual stress with FEA. Because of the limitation in the available equipment, instead of the use of synchrotron and neutron diffraction techniques to analyze the residual stresses in fabricated samples, based on the existing results of residual stress measurement on both lab-scale and full-scale samples with the girth weld, it was assumed that the highest distribution of deep pits and cracks ($> 80 \mu\text{m}$) is to be observed if the mechanical bending is applied at $0 \text{ mm} < |x| < 30$ mm. As such, the addition of tensile bending residual stress on the OD surface at $d = 30$ mm, $d = 15$ mm and 0 mm was conducted to compare the effect of welding residual stress distribution on pits and cracks morphologies. Furthermore, specimens with no girth weld were also fabricated to identify the effect of girth weld on the initiation and Stage I growth of C-NNpHSCC. The specimens were cut along the length direction to observe the pit and crack growth in the circumferential direction with a water jet, as shown in Figure 3.4.

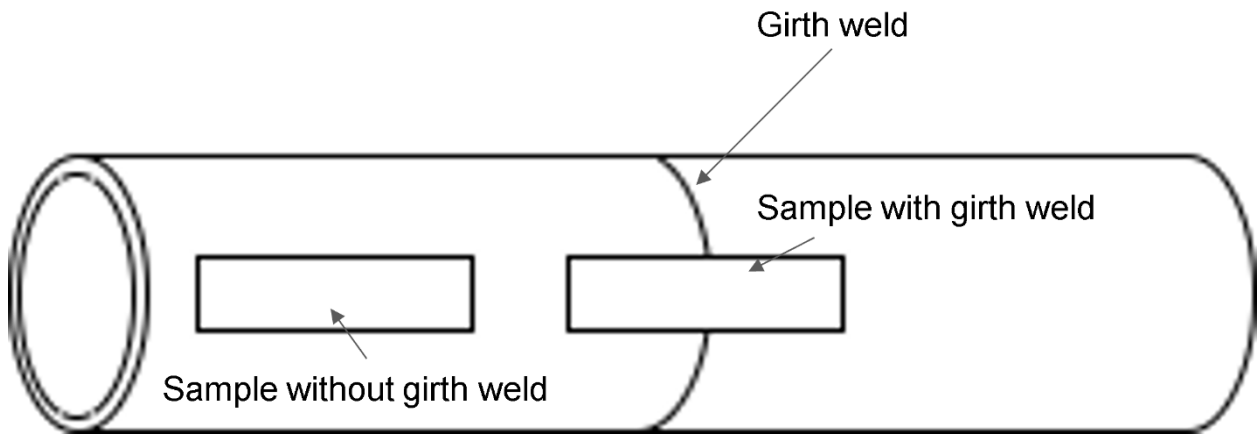


Figure 3.4 Brief schematic of X52 pipeline steel and the specimens cut from it.

Half of each kind of sample was manually bent inwardly with a bend angle of 20 degrees (-20 degrees) to apply tensile bending residual stress to the outer surface (OD) of the sample, as well as the rest of them bent outwardly with the same bend angle (+20 degrees) to apply compressive bending stress on the OD by mechanical bending process, as shown in Figure 3.5.

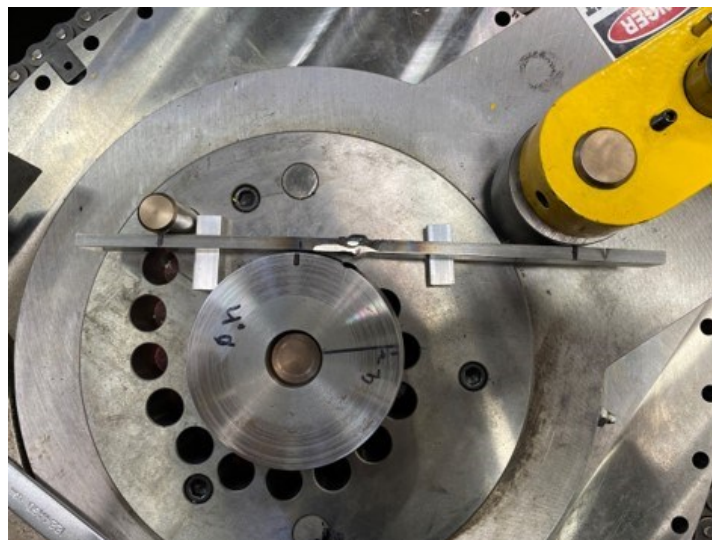


Figure 3.5 Picture of a specimen subjected to the mechanical bending process.

This process also aimed to cause mill scale exfoliation and cracking, which is expected to be more frequently observed on the samples bent outwardly with respect to the OD than those bent inwardly because of the tensile bending force exerted. The exfoliated or cracked mill scales create the path for the corrosive solution to bare metal surfaces, potentially raising the number of localized corrosion sites. It must be noted that mechanical bending applied to the specimens with $d = 0$ mm caused bending at the areas adjacent to the girth weld rather than the weld itself because of the higher thickness of the girth weld than base metal and resistance to bending accounted by the geometry, as shown in Figure 3.6.

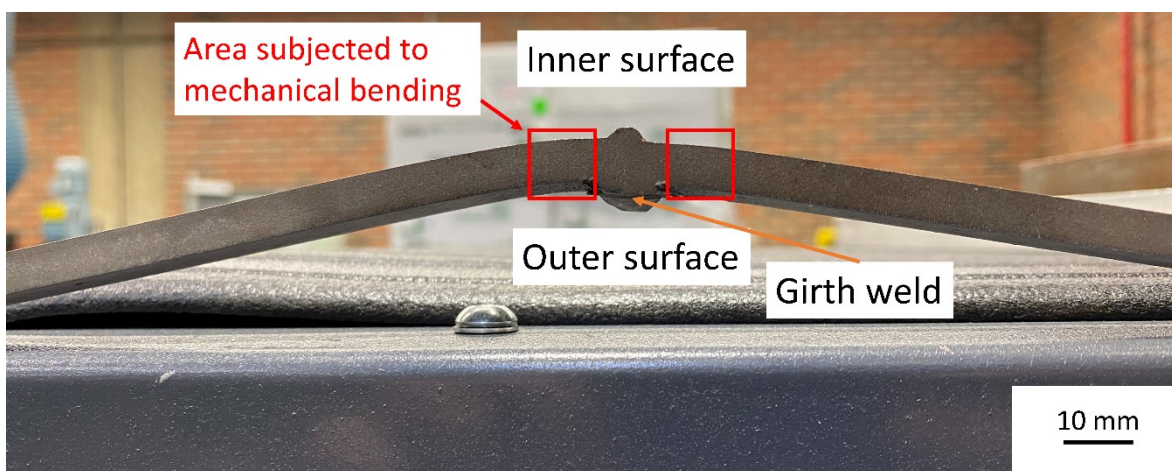


Figure 3.6 Front of a fabricated specimen ($d = 0$ mm) with the locations at which bending force was applied

In addition to the specimens subjected to static corrosion tests, three control samples were cut off from the pipeline steel to verify the result of static corrosion tests in the C2 solution and to investigate the morphologies of mill scale after the abovementioned mechanical bending process. Figure 3.7 illustrates the control samples selected for the comparisons: straight control sample A with the girth weld at the center, control sample B with the girth

weld at the center and compressive bending stress on the OD side, and control sample C with tensile bending stress on the OD and without the girth weld. Just as for the corroded samples, the total bend angles are 20 degrees inward or outward with respect to the OD. It must be noted that these control samples were not subjected to static corrosion tests.

After washing the outer surface with acetone to remove the remaining coating on the OD and clean the sample, to prevent preferential corrosion on the banded structure of X52 steel, coating tapes were applied on each specimen's inner surface and sides.

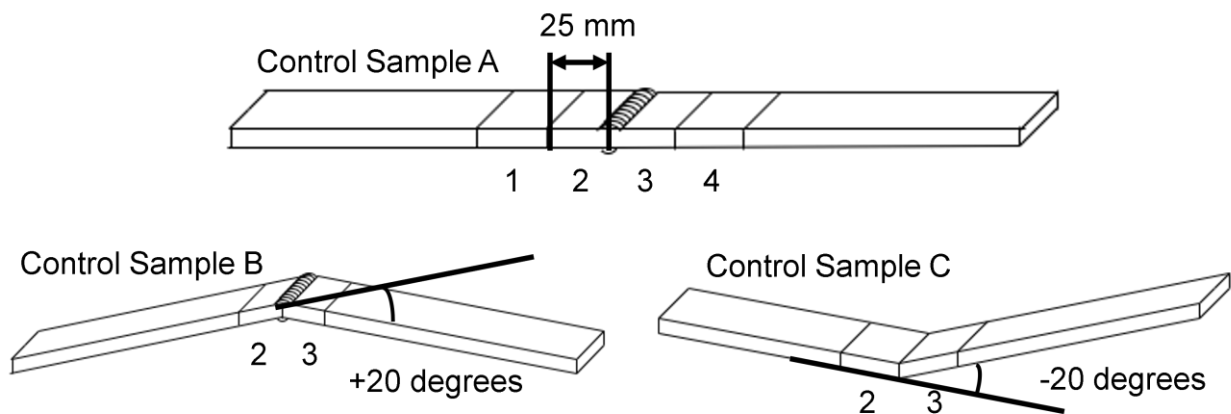


Figure 3.7 Schematics of control samples

3.2 Static Corrosion Tests

The taped specimens mentioned above were then immersed into graduated cylinders filled with NNpH solution, as shown in Figure 3.8.

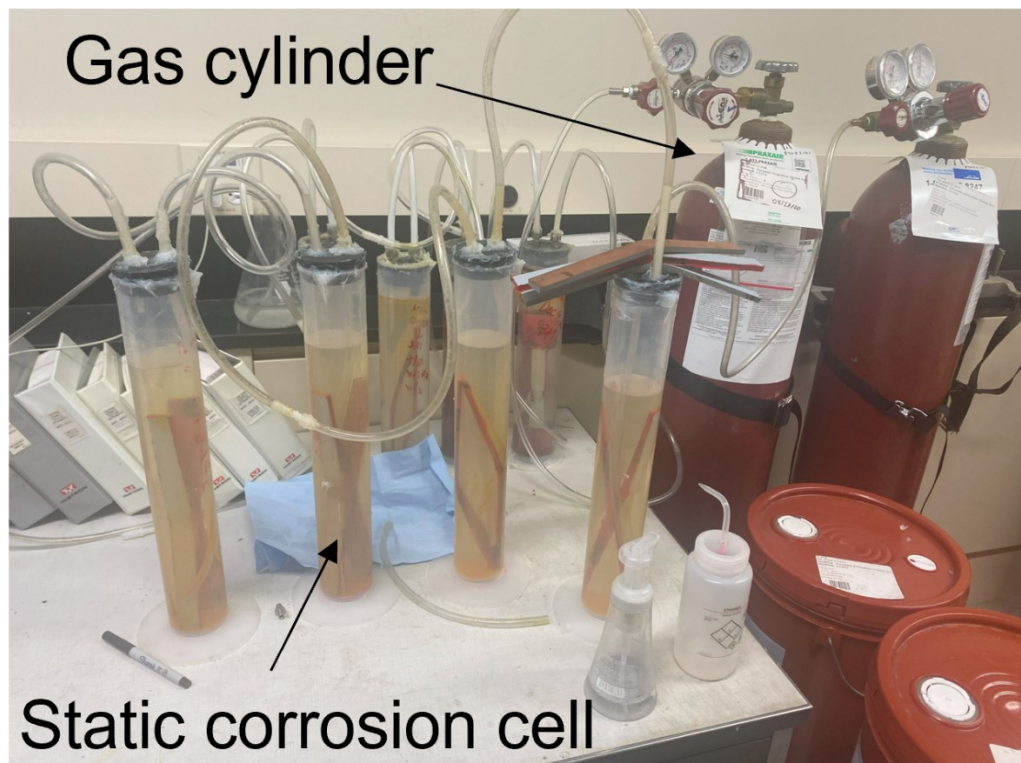


Figure 3.8 Static corrosion cells filled with C2 solution and the specimens, connected to 5% CO₂ + balanced N₂ gas cylinders

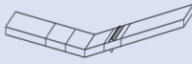
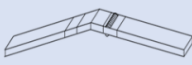


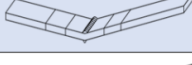



The NNpH solution used in this experiment was a C2 solution with a pH of 6.2 to 6.3 when sparged with 5% CO₂ (See section 2.2.1). The chemical composition of the C2 solution is shown in Table 3.1. Test cells containing the solution and specimens were sealed with lids and silicone sealant, then connected to a gas cylinder with 5% CO₂ and balanced N₂ gas to maintain the pH of the C2 solution by purging oxygen. Based on the results of previous research with the same experimental setup, the effect of a limited solution on the morphologies of pits and cracks is unlikely. However, a higher concentration of Fe²⁺ in the solution than in the bulk solution may facilitate the formation of FeCO₃. Further study on

pH change during the experiment and change in the concentration of Fe^{2+} may be required in future work. To understand the morphologies of corrosion pits and microcracks formed in C2 solution, the durations of the tests were set to 90 days (Sample 1 to 8) and 150 days (Sample 9 to 16). The overall test metrics and the dimensions and number of specimens are shown in Table 3.2.

Table 3.1 Chemical compositions of near-neutral pH C2 solution

Chemical compound	Mass of chemical compound per 1L of C2 solution (g)
$\text{MgSO}_4 \cdot 7\text{H}_2\text{O}$	0.0274
$\text{CaCl}_2 \cdot 2\text{H}_2\text{O}$	0.0338
KCl	0.00350
NaHCO_3	0.0195
CaCO_3	0.00606

Table 3.2 Schematics of the samples corroded for 90 days (Sample 1 to 8) and 150 days (Sample 9 to 16).

Distance between the center of the bend and the weld center line (mm)	Inward bending with tensile bending residual stress on the OD (-20 degrees)	Outward bending with compressive bending residual stress on the OD (+20 degrees)
d = 30 mm	Sample 1 (90 days) Sample 9 (150 days) 	Sample 3 (90 days) Sample 11 (150 days) 
d = 15 mm	Sample 2 (90 days) Sample 10 (150 days) 	Sample 4 (90 days) Sample 12 (150 days) 
d = 0 mm	Sample 5 (90 days) Sample 13 (150 days) 	Sample 7 (90 days) Sample 15 (150 days) 
d = N/A	Sample 6 (90 days) Sample 14 (150 days) 	Sample 8 (90 days) Sample 16 (150 days) 

3.3 Characterization Processes

3.3.1 Post-Test Processes

After the static corrosion tests, samples were cut into four pieces, each of length 26 mm, as shown in Figure 3.9.

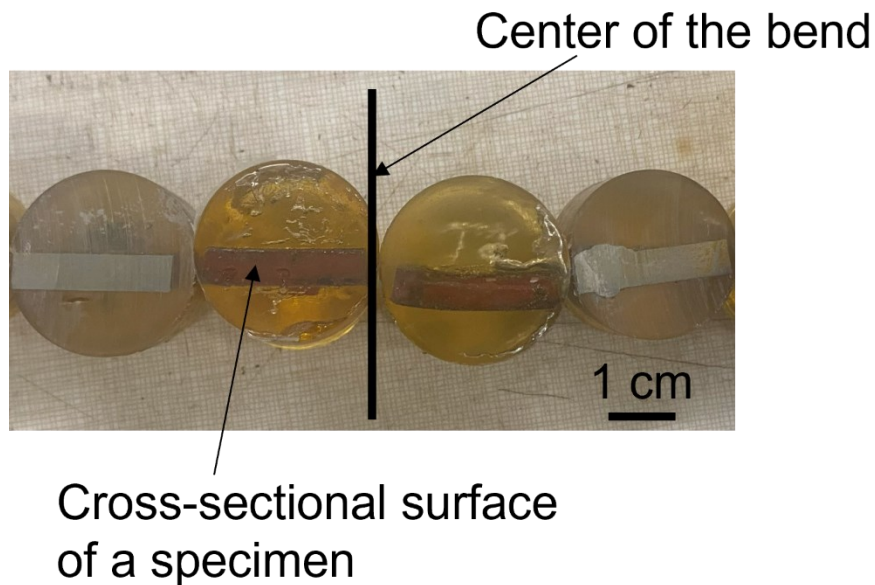
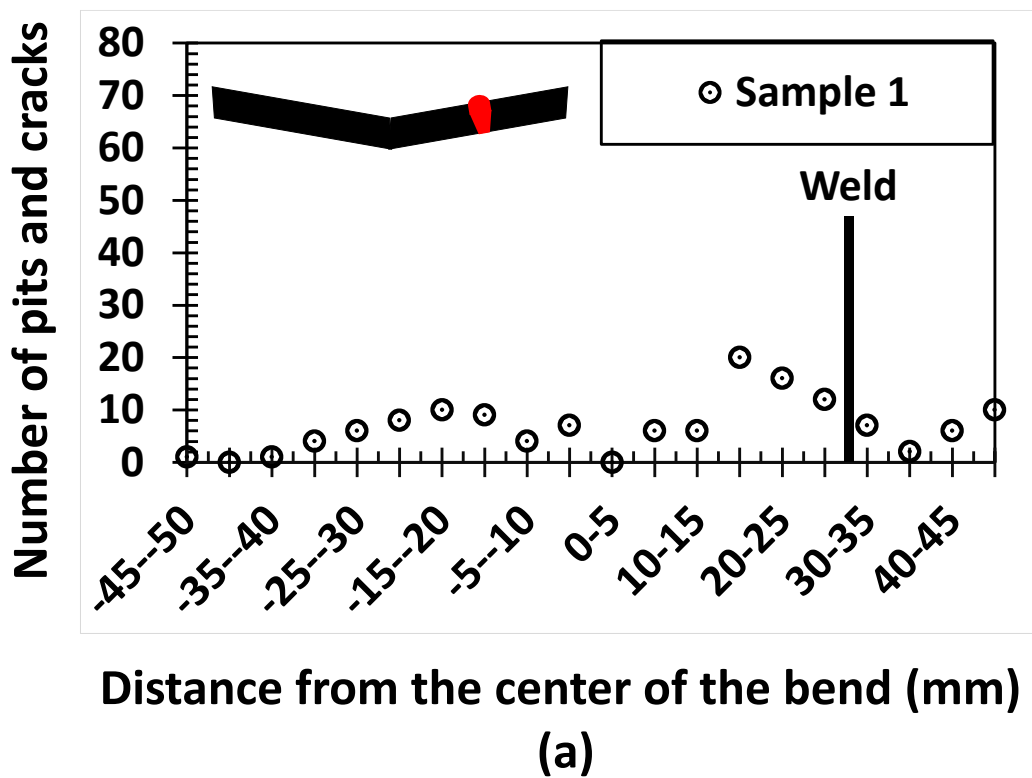


Figure 3.9 Cross-sectional surfaces of sectioned samples mounted in epoxy resin.

Each two of the sectioned specimens were mounted in epoxy resin and polished with 6 μm and 1 μm diamond pastes. These polished samples were then subjected to optical microscopy (OM) and SEM observations to count the number of pits and microcracks and investigate their morphologies. After the observation, these samples were sectioned by 2 mm with a cutting machine, polished, and characterized again. These steps were repeated until the characterization of 5 sections per piece of samples was completed. Just as for the corroded specimens, control sample A was evenly split into four sections from the center of the bend, of which the cross sections were sectioned by 2 mm each time the characterization with SEM was finished. During the characterizations of control samples B and C, it was assumed that mechanical bending would not affect the mill scale within the

regions 25 mm away from the center of the bend. As such, the number of pits and cracks and the frequencies in those samples' regions were reused from control sample A.

The collected data was then converted into two graphs: The distribution of corrosion pits and cracks with different distances from the center of the bend and the frequency of pits and cracks versus different ranges of depths. Examples of these graphs are shown in Figure 3.10 a) and b). The pits and cracks shallower than 20 μm are ignored in this research to avoid confusion with general corrosion sites. Details of the criteria for countable pits and cracks are explained in the later section.



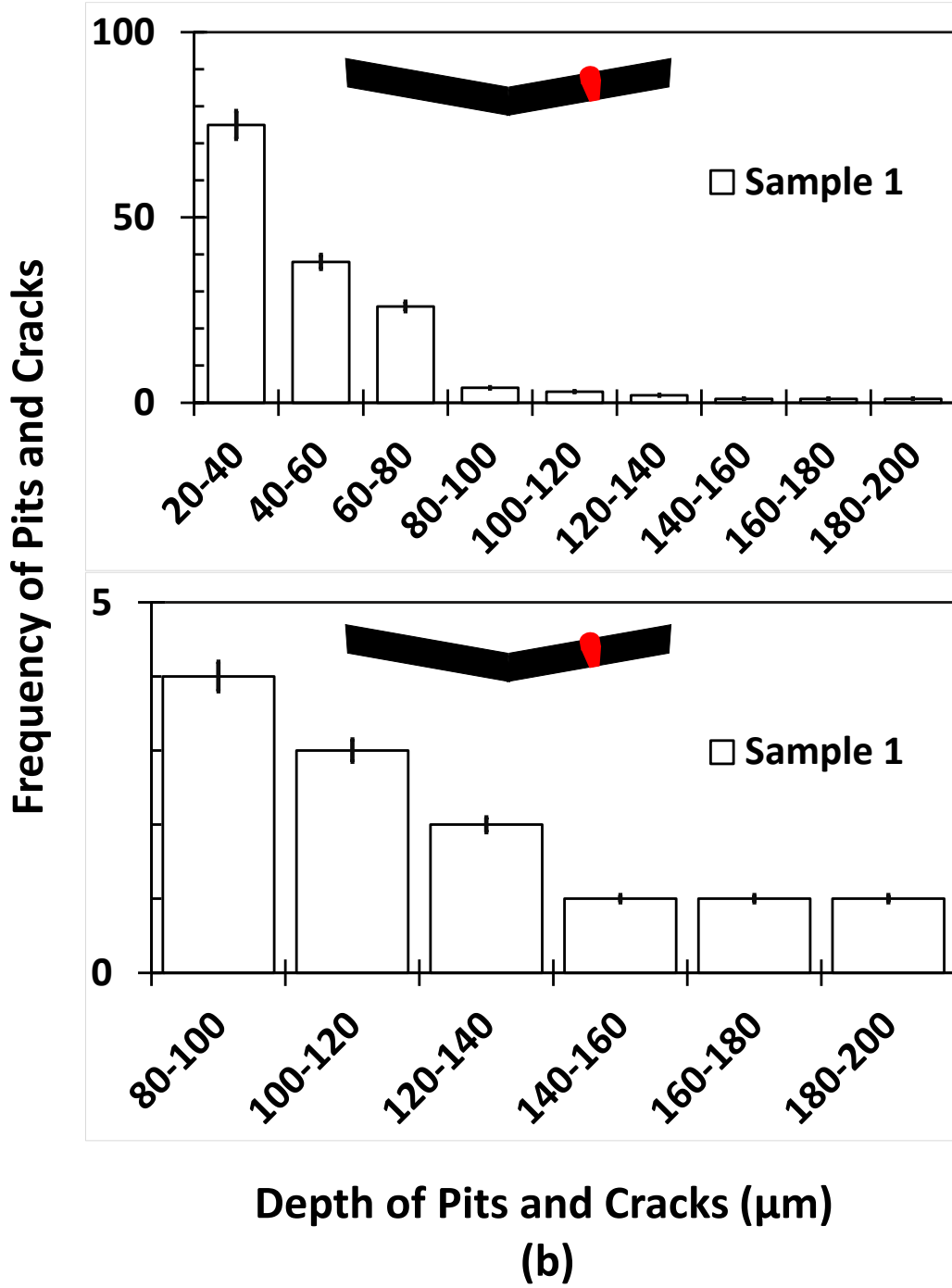


Figure 3.10 a) Distribution of pits and cracks over the length of a corroded sample and b) frequencies of pits and cracks in varying depths derived from characterization processes.

Chapter 4 : Results

This chapter will present the results of the static corrosion tests. First, the characterization of control samples and morphologies of mill scale layers before and after mechanical bending are examined and discussed. Second, the results of static corrosion tests and comparisons regarding the change in surface morphologies with varying durations are introduced. Third, the comparisons between the samples corroded for 150 days regarding the distance between the center of the bend and the weld centerline are made and discussed. Finally, the same comparisons regarding the bend angle are made and discussed.

4.1 Mill scale characterization

Figure 4.1 shows the cross-sectional images of control sample A in the regions a) - b) (within 25 mm of the center of the bend and b) - d) 25 mm away from the center of the bend.

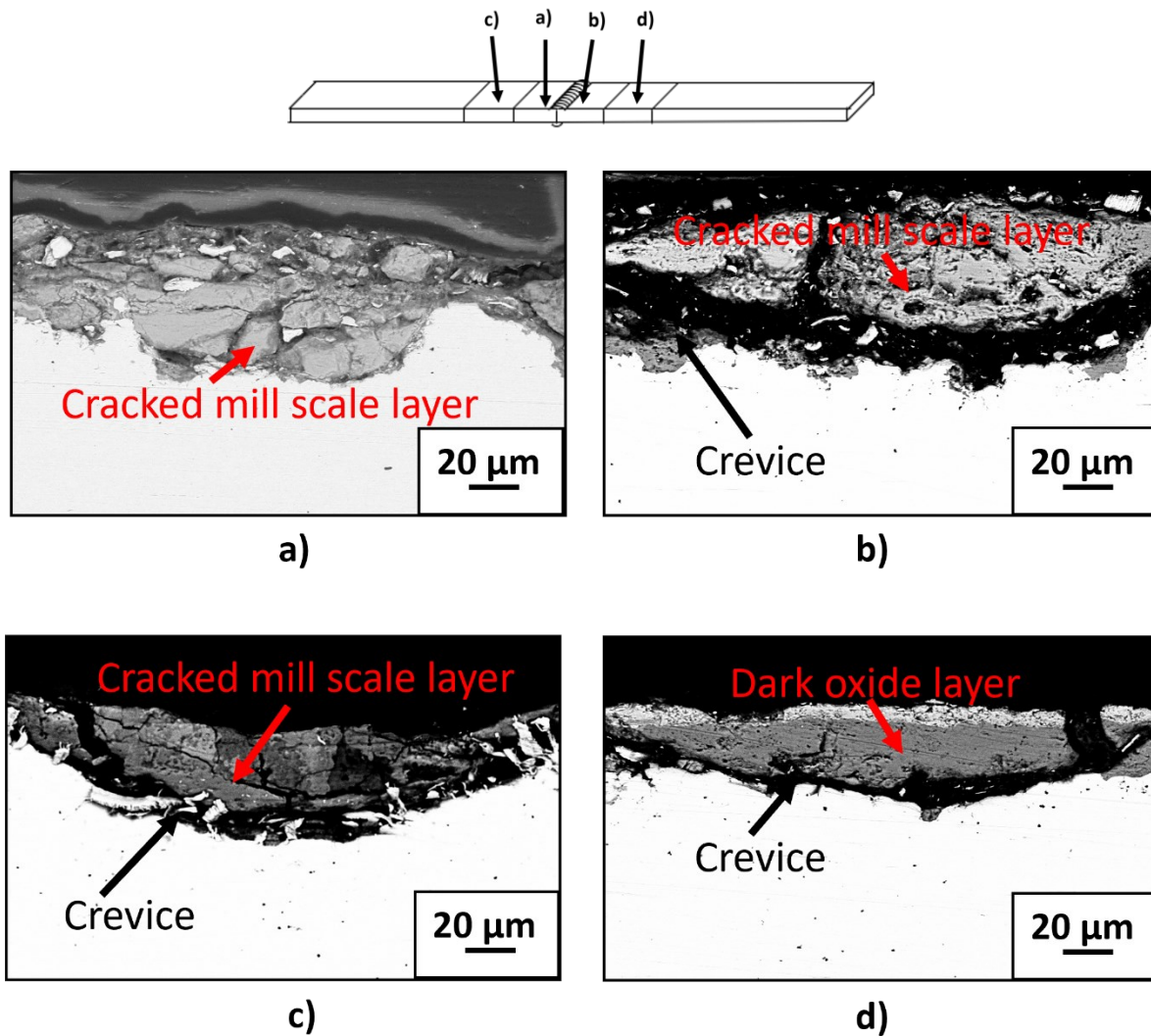


Figure 4.1 Schematics of control sample A and a)-d) surface morphologies of mill scale layer at corresponding locations

Figure 4.1 (a) shows that the sample surface is uniformly covered with $\sim 61.5 \mu\text{m}$ of mill scale. A fractured mill scale layer containing cracks is visible in Figure 4.1 b). With cracks in the mill scale and a crevice at the bottom, crevice corrosion can occur between the mill scale and base metal. Since this feature was observed in the regions away from and near the

center of a straight control sample, as visible in Figure 4.1 c), it can be estimated that the crevice corrosion will be caused regardless of the distance from the center of the bend. This exfoliation of the mill scale might have been caused in the service environment or during the sample preparation processes. The mill scale layer in Figure 4.1 d) consists of two oxides with different contrasts: a bright layer and a dark layer with identical texture. EDS analysis was conducted on the bright and dark layers to identify the composition of these oxide layers, for which the result is shown in Figure 4.2.

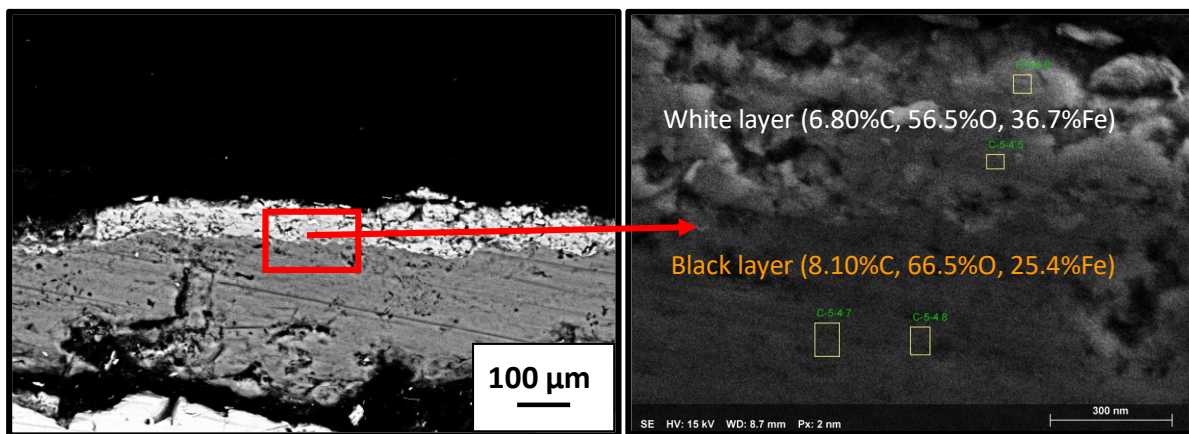


Figure 4.2 Atomic concentration (%) of a) white layer and b) dark layer of oxide in Figure 4.1 d)

As mentioned in Chapter 2, the mill scale is primarily composed of an inner layer of magnetite (Fe_3O_4), which is covered by hematite ($\alpha\text{-Fe}_2\text{O}_3$), goethite ($\alpha\text{-FeOOH}$), lepidocrocite ($\gamma\text{-FeOOH}$), and wüstite (FeO) [9]. Although a definitive conclusion cannot be made based solely on the backscattered SEM images and compositions, from the Fe/O ratios observed in EDS, it can be estimated that the dark layer shown in Figure 4.2 (b) is magnetite (Fe_3O_4). Since the atomic composition of the bright layer in Figure 4.2 (a) does

not correspond to any of the materials mentioned above, this is likely surface contamination.

Figure 4.3 a)-c) shows the cross-sectional surface morphologies of control sample B.

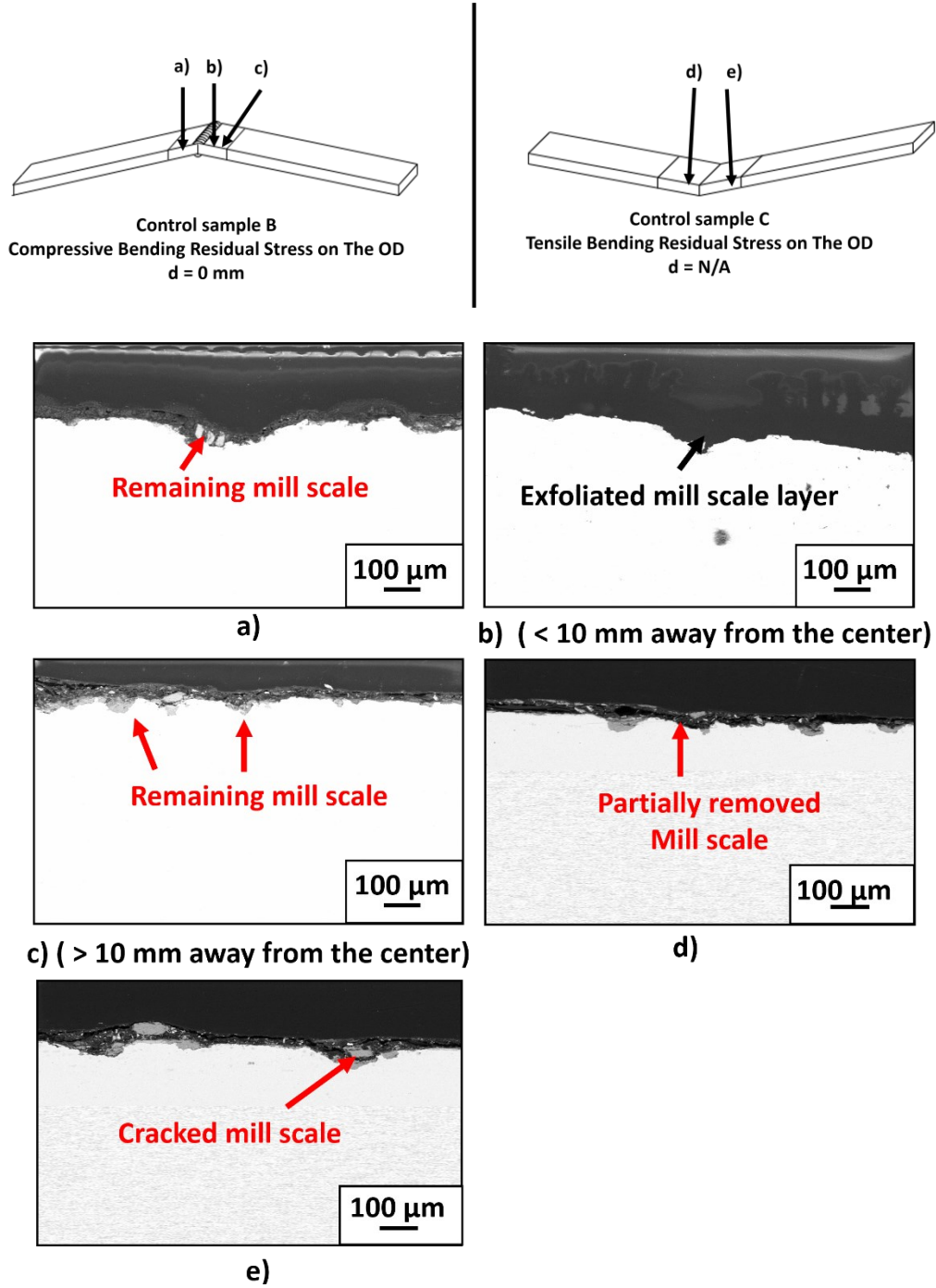


Figure 4.3 Schematics of control samples B&C and a)-e) surface morphologies of mill scale layer at corresponding locations

As shown in Figure 4.3 a), the mill scale layer observed in control sample A is not visible in control sample B. This mill scale layer is absent until 10 mm away from the center of the bend. The same feature was also observed on the opposite side of the control sample B with respect to the center of the bend, although the remaining mill scale is occasionally seen (Figure 4.3 b)). Several cracked fragments of the mill scale layer are also observed, one of which is visible in Figure 4.3 c). These observations point out that partial to complete exfoliation of the mill scale layer occurred because of outward bending with respect to OD, which potentially affects the surface morphologies after the static corrosion test.

Figure 4.3 d) and e) show the cross-sectional surface morphologies of control sample C. As shown in Figure 4.3 d), the uniform mill scale layer observed in control sample A is not visible. However, the complete exfoliation of the mill scale observed in control sample B is also not seen in control sample C. A higher magnification image of a fragment of the mill scale shows several cracks (Figure 4.3 e)). These morphologies suggest that exfoliation and cracking of the mill scale were also caused by inward bending with respect to OD, although less significantly than in the control sample B. Figure 4.4 shows the direct comparison of control samples A to C at the exact same location with respect to the center of the bend. As can be seen, the change in the thickness and density of the mill scale on the sample surface before and after bending is significant.

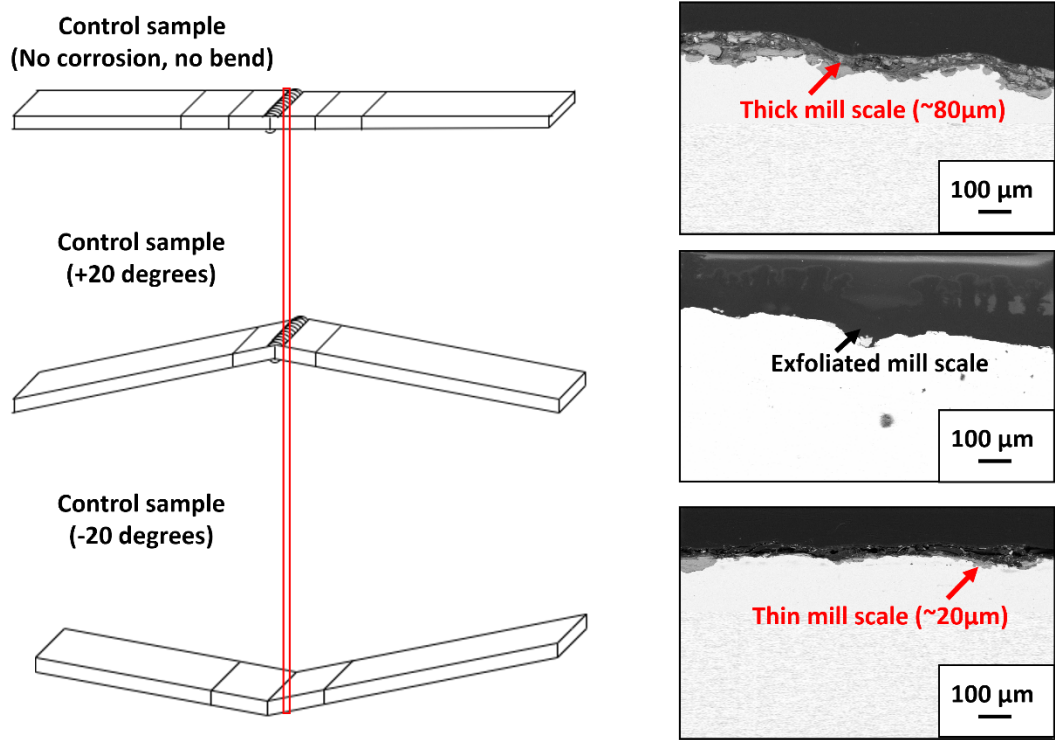


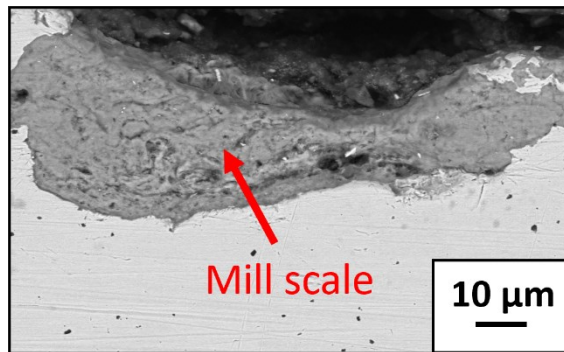
Figure 4.4 Surface morphologies of control samples A, B, and C at the center of the bend

4.1.1 Distribution and frequency of corrosion pits

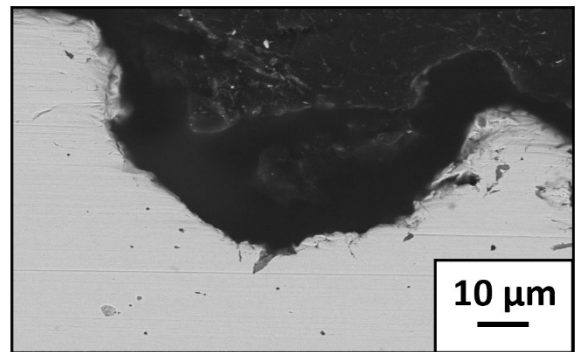
To further investigate the change in the number and depth of countable pits, the number of pits over the length of control samples with respect to the center of the bend and the frequency of pits with different depths were recorded. Before these processes, to distinguish pits and cracks formed in C2 solution from pre-existing pits, specific criteria were made as follows:

1. Pits and cracks covered in mill scale are considered uncountable (Figure 4.5 a)).
2. Pits and cracks not covered with mill scale are considered countable (Figure 4.5 b)).

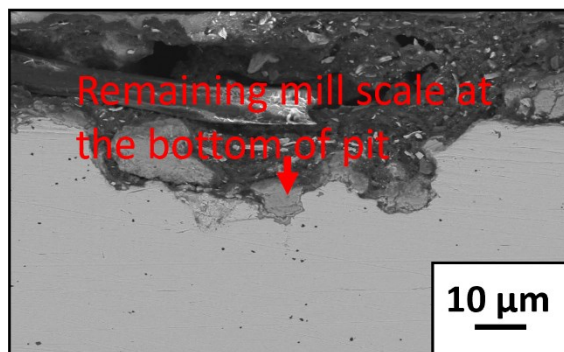
3. Pits and cracks whose bottom was covered in mill scale are considered uncountable (Figure 4.5 c)).
4. Pits and cracks partially covered with mill scale are considered countable if the crevice depth between the mill scale and base metal is deeper than 20 μm (Figure 4.5 d)).



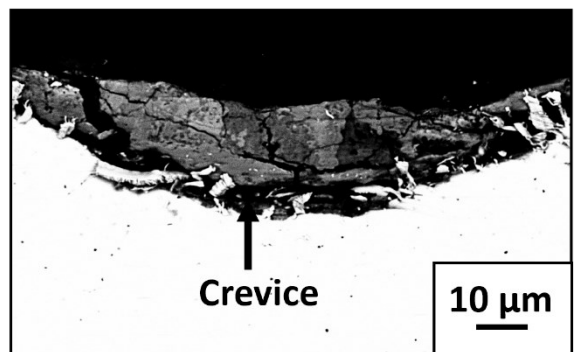
a) Not counted as a pit



b) Counted as a pit



c) Not counted as a pit

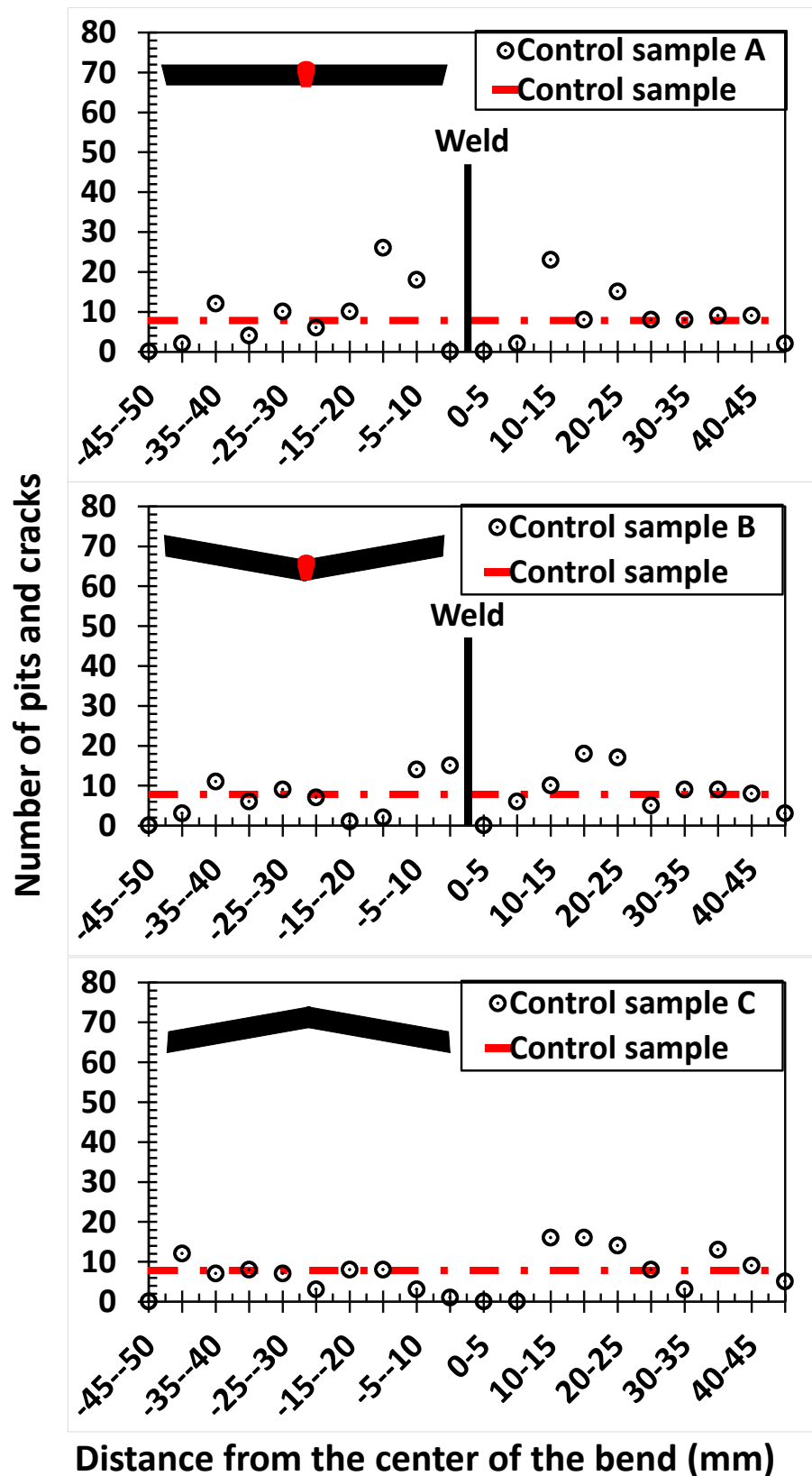


d) Not counted as a pit if < 20 μm

Figure 4.5 BSD images of typical countable/uncountable pits and cracks observed on sample surfaces.

These criteria were established because the resultant corrosion product, FeCO_3 , is unlikely to be formed unless a higher concentration of Fe^{2+} or CO_3^{2-} is achieved at specific sites such as cracked or porous mill scale, as discussed in Chapter 2 [9]. It must be noted that these criteria are not able to differentiate the pits and cracks that emerged in the NNpH environment from pre-existing defects with no trace of mill scale, as shown in Figure 4.5 b). However, these criteria are useful to minimize the errors in characterization processes caused by the initial conditions of the pipe surface and mill scale.

The resultant graphs of pits and cracks distribution vs. length of the samples relative to the center of the bend are shown in Figure 4.6 a).



(a)

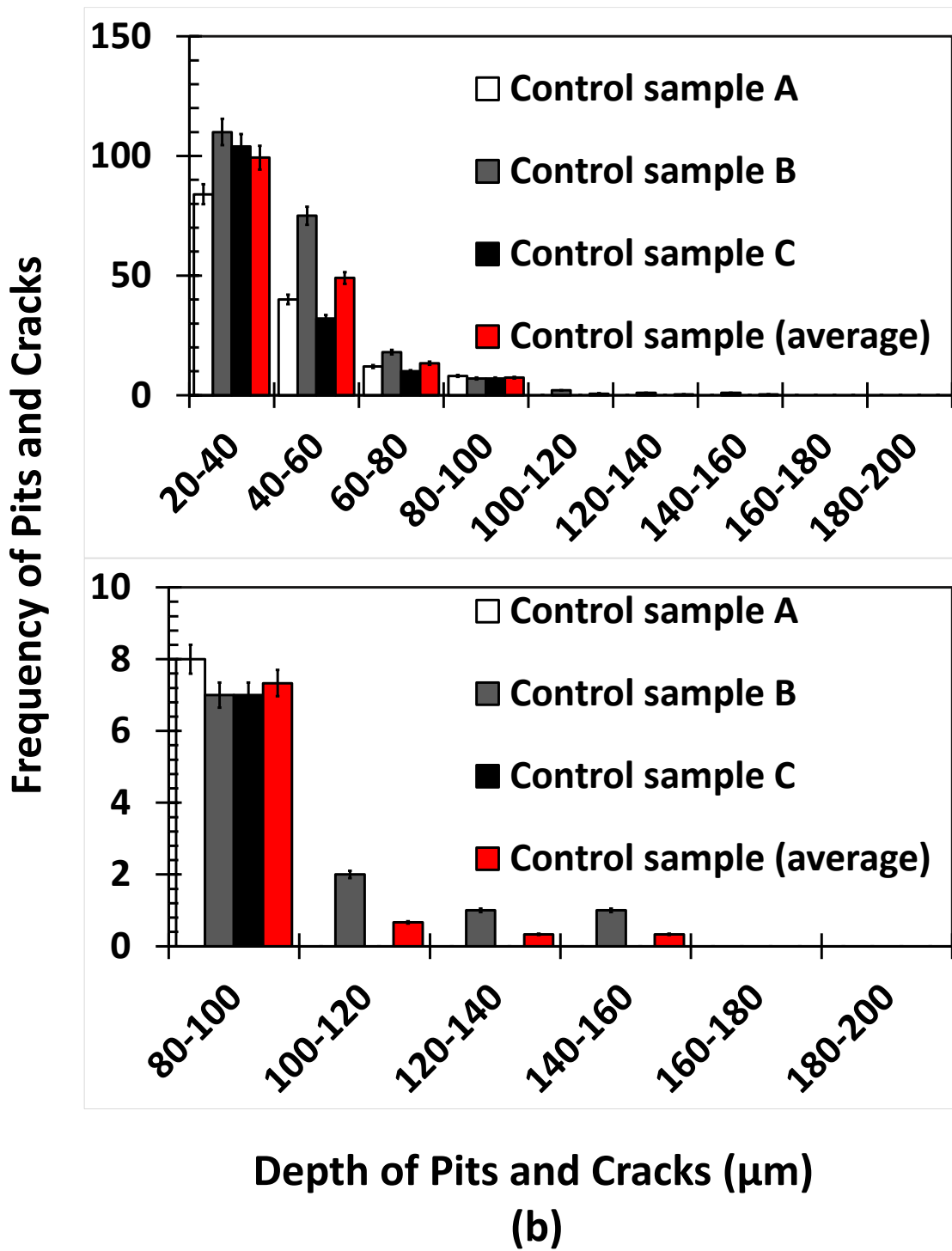


Figure 4.6 a) Distribution and b) Total frequency of pits and cracks in the control samples vs. depth of pits and cracks

Black vertical lines in the graphs show the presence of the girth welds, as well as their locations. As mentioned in the previous section, the data of the regions further than 25 mm away from the center of the bend in control sample A are reused for control samples B and C. This explains the nearly identical curves within the regions mentioned in the distribution graphs. Comparison between control samples A to C shows that the peak number of pits is 10 mm to 20 mm away from the center of the bend. However, the overall distributions are somewhat identical. Regarding the change in the number of pits in the aforementioned region, the peak number in both control samples B and C is approximately 17 % higher than that of the control sample A. A comparison between control samples B and C shows a similar trend. However, the number of pits is significantly lower at $-20 \text{ mm} < |x| < -30 \text{ mm}$ in control sample C compared to control sample B. This random spike in the number of pits is also observed in control sample A. It can be assumed that the initial surface conditions of each sample may affect the number of pits and cracks after the static corrosion test. This is particularly true for areas located farther from the center of the bend since there is less chance of mill-scale cracking and exfoliation. Figure 4.6 b) illustrates the frequencies of pits and cracks found in the control samples with different depths, ranging from 20 μm to 200 μm . It is seen in Figure 4.6 b) that the number of shallow pits ($< 60 \mu\text{m}$) significantly increased after mechanical bending. However, the frequencies of middle to deep pits ($> 60 \mu\text{m}$) only showed slight change. This indicates that the mechanical bending did not contribute to the exfoliation of the mill scale that previously filled pre-existing pits, as opposed to the shallow pits. Furthermore, the comparisons between control samples in **Error! Reference source not found.** a) and b) exhibit somewhat identical results. As such, i

It can be concluded that both outward (control sample B) and inward (control sample C) mechanical bending with respect to the OD induced no significant mill scale exfoliation compared to a straight sample (control sample A). Hence, as shown in **Error! Reference source not found.** a), the distribution of pits and cracks on control samples can be normalized as a red line at $y = 7.4$. The frequencies of pits and cracks in control samples are nearly identical, aside from the pits and cracks deeper than $100\ \mu\text{m}$. However, the difference in the frequencies above $100\ \mu\text{m}$ is less than 5, which is considered insignificant. As such, the average frequency of the control samples shown in Figure 4.6 is compared with corroded samples and further discussed in the next section.

4.2 Characterization of Corroded Samples and Comparisons in Terms of Durations

Following the procedures used for the control samples, the cross sections of 16 corroded samples with varying bend angles, distances between the center of the bend and center of the girth weld, and duration of static tests, as mentioned in section 3.2.1, were carefully characterized with SEM and optical microscopy (OM).

The literature points out that preferential corrosion and crack propagation occur at the HAZ and the weld toes. Such features were not seen in the corroded samples[6]. Instead, as shown in Figure 4.7, the weld toe was covered with a thick oxide layer, protecting the weld metal and toes from the NNpH environment.

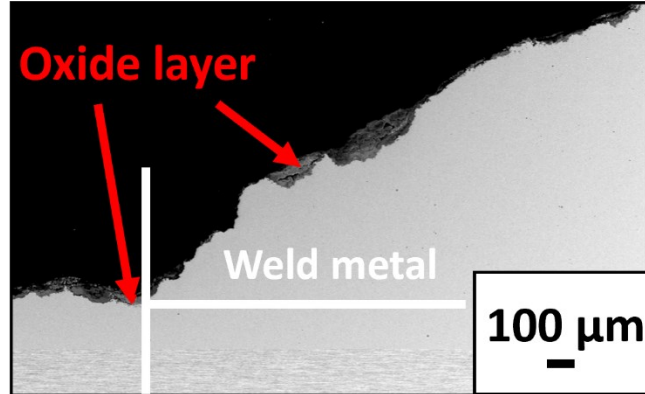


Figure 4.7 Cross-sectional morphology of a corroded sample at the weld toe

This may be the remnant of oxide layers formed during the welding process. This feature was observed throughout the corroded samples, regardless of the variables such as the duration of static corrosion tests, bending angles, and the distance between the girth weld and the center of the bend. As such, the distribution of pits and cracks around the weld centerline tends to be lower than the other points. It must also be noted that the distribution of deep pits and cracks ($> 80 \mu\text{m}$) tended to be near the center of the bend of corroded samples, particularly on the samples with tensile bending residual stress on the OD. However, those defects were also observed in the area away from the center of the bend. These are possibly the pre-existing defects initially covered by the mill scale layer, which was later dissolved in the NNpH environment.

4.2.1 Samples bent in compression with tensile residual stress on the surface ($d = 30 \text{ mm}$)

As mentioned in Chapter 3, regarding the initiation and stage 1 growth of C-NNpHSCC, samples 1 (90 days) and 9 (150 days) may represent the most aggressive situations in the field.

Figure 4.8 a) to h) illustrates the cross-sectional morphologies of samples 1 and 9 with BSD SEM.

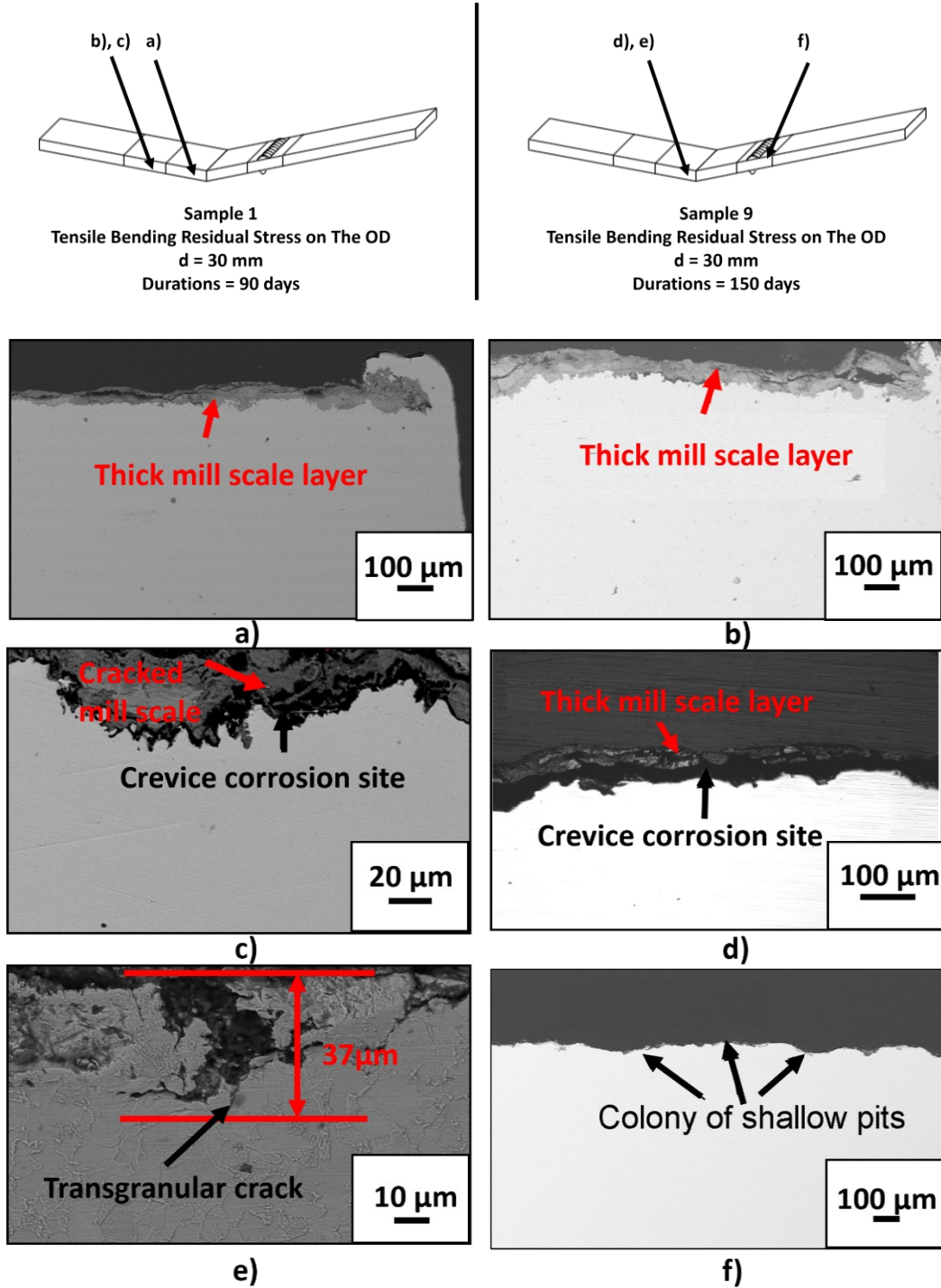


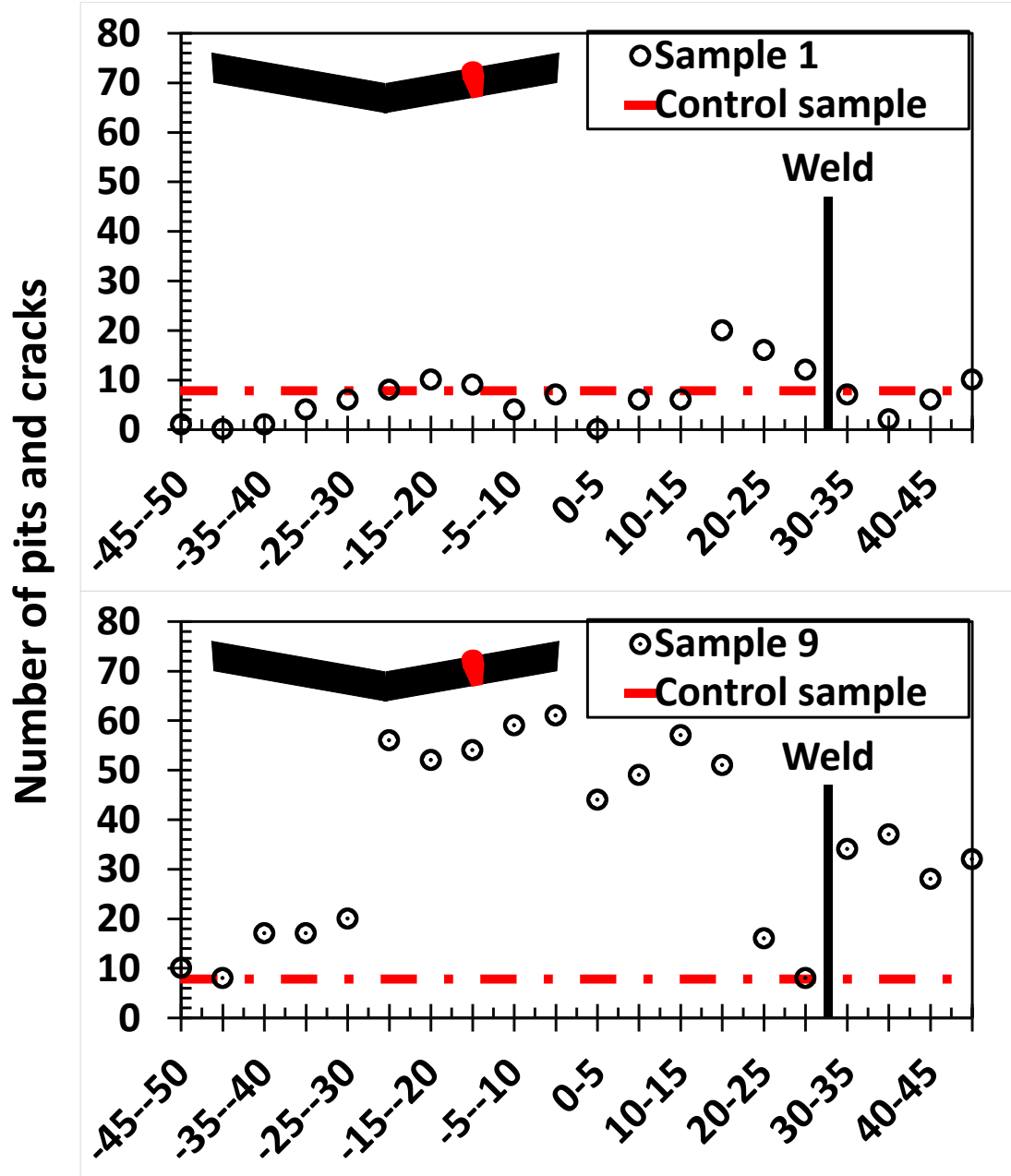
Figure 4.8 Schematics of Sample 1 & 9 as well as the cross-sectional surface morphologies of the samples; a) BSD image of sample 1 surface covered with thick mill scale layer a)

near and b) away from the center of the bend, c) magnified MDS image of a crevice corrosion site with cracked mill scale layer in the area away from the center of the bend of sample 1, d) OM image of a crevice corrosion site with dissolved mill scale near the center of the bend of sample 9, e) a magnified BSD image of transgranular crack observed near the center of the bend of sample 9, and f) BSD image of a colony of shallow pits near the girth weld of sample 9.

As shown in

Figure 4.8 a)-b), the surface of sample 1 is mainly covered with the remaining mill scale with a thickness of 100 μm . A few micrometres of microcracks propagated from the crevice between the cracked mill scale and base metal, one of which is visible in Figure 4.8 c), were observed at any region. Unlike microcracks found in the control samples, these microcracks were not covered in mill scale. Cross-sectional morphologies of the surface of sample 9 are visible in Figure 4.8 d) to e). As seen in Figure d), unlike sample 1, the mill scale on the surface of sample 9 has been mostly exfoliated. As shown in Figure 4.8 f), crevice corrosion sites deeper than 20 μm were more frequently observed in sample 9 compared to sample 1. Furthermore, the same feature was observed regardless of the distance from the center of the bend.

Figure 4.9 a) compares the distribution of pits and cracks relative to the center of the bend between samples 1 and 9, control samples.



Distance from the center of the bend (mm)

(a)

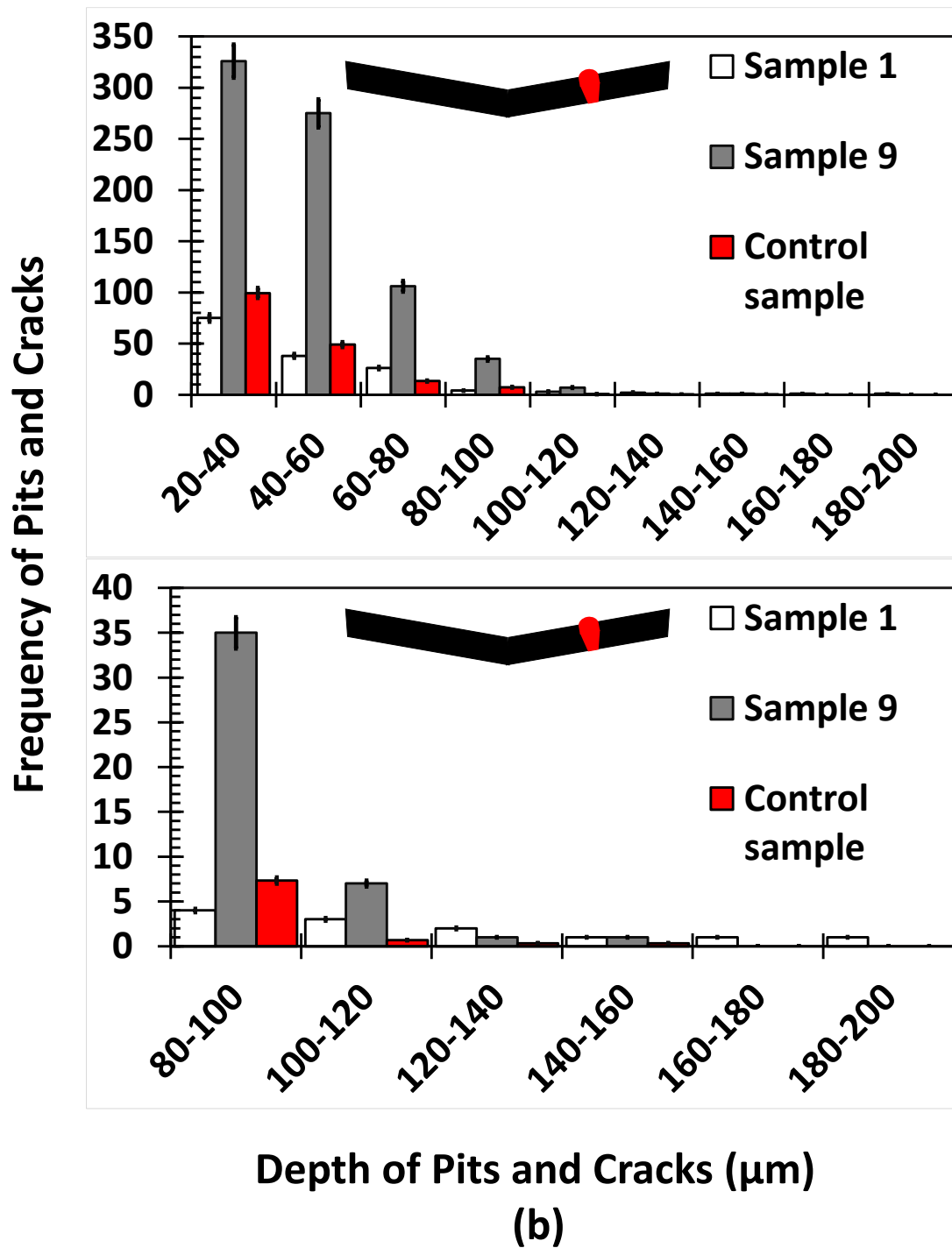


Figure 4.9 a) Distribution and b) frequency of pits and cracks in samples 1 (90 days) & 9 (150 days) and control samples.

As shown in Figure 4.9 a), the distribution of pits and cracks in sample 1 is identical to the control samples. On the other hand, sample 9 exhibits a much higher number of pits and cracks throughout the length than sample 1 and the control samples, particularly at $0 \text{ mm} < |x| < 20 \text{ mm}$. Figure 4.9 b) shows the frequencies of pits and cracks with different depths in the above samples. As can be seen, there is a common trend that the highest frequency is exhibited between 20 to 40 μm pits and cracks, diminishing with the increase in depth. The frequencies in sample 1 are roughly identical to the control samples. However, sample 9 exhibits significantly higher frequencies than both sample 1 and control samples, particularly at 20-100 μm . This trend becomes less apparent at 100-120 μm and diminishes above 120 μm . The pits and cracks deeper than 120 μm observed in sample 1 are likely pre-existing pits uncovered by the removal of the mill scale during sample preparation or static corrosion test, as such defects cannot be filtered through the criteria mentioned in section 4.1. Since this type of error has been observed across the samples subjected to static corrosion tests, the optimization of the criteria may be required in future work, which is discussed in Chapter 6.

4.2.2 Samples bent in compression with tensile residual stress on the surface ($d = 15 \text{ mm}$)

As mentioned in Chapter 3, samples with $d = 15 \text{ mm}$ have been selected to visualize the change in surface morphologies and frequencies of pits and cracks in the samples with the change in d . Figure 4.10 a) to f) shows the cross-sectional morphologies of sample 2 and sample 10, taken as BSD images.

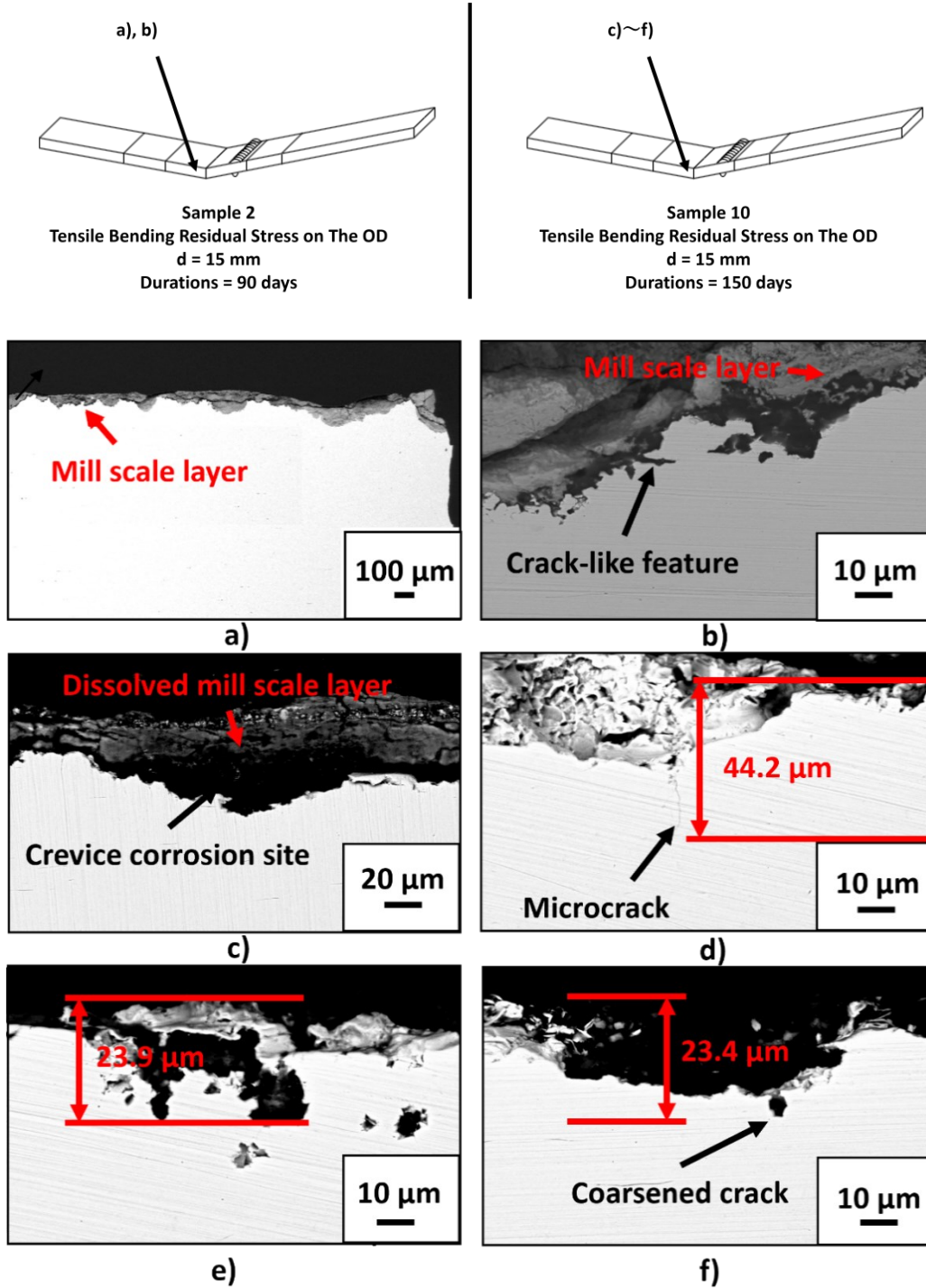
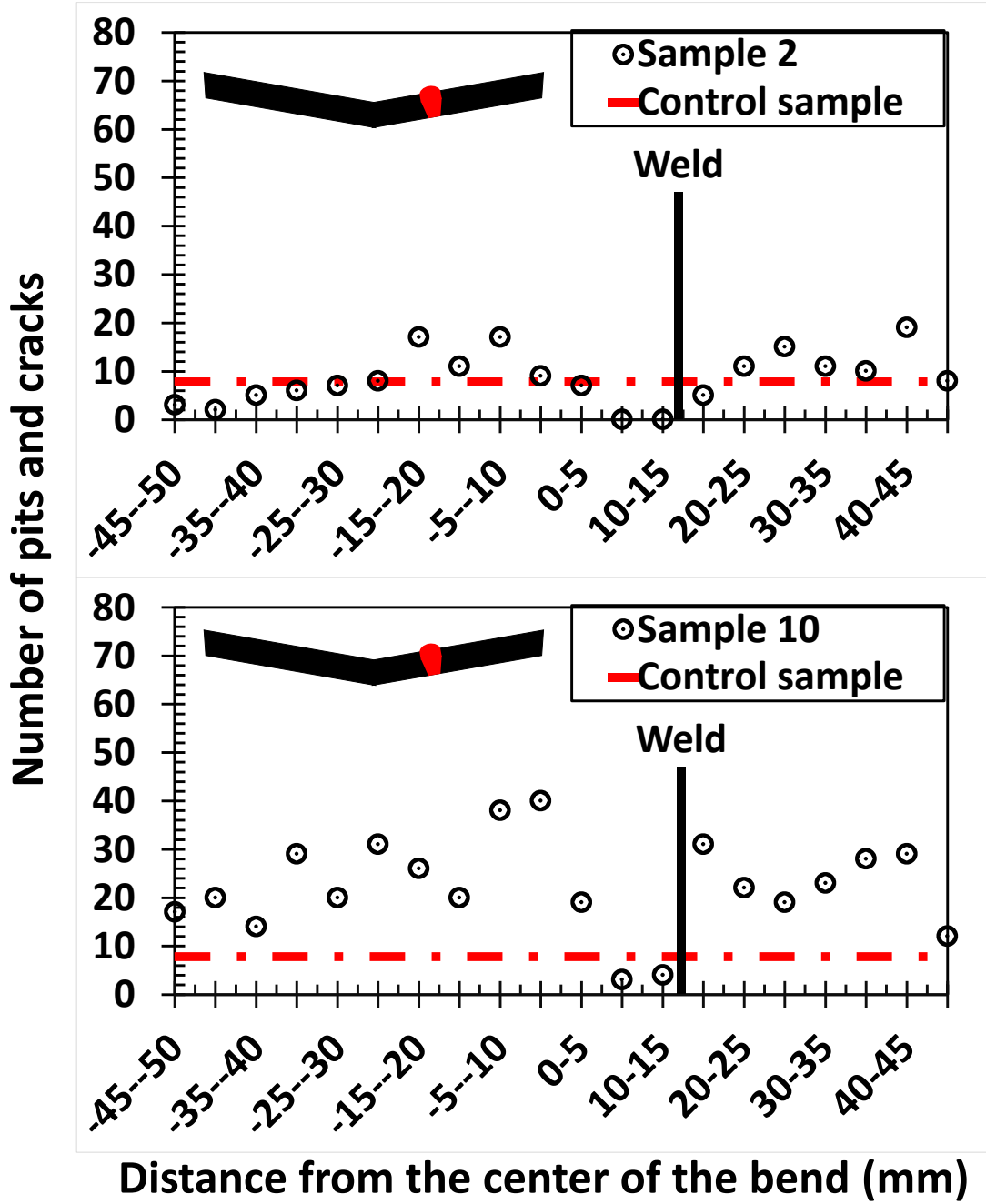


Figure 4.10 Schematics of Sample 2 & 10 as well as the cross-sectional surface morphologies of the samples; a) BSD image of sample 2 surface covered with mill scale

near the center of the bend, b) magnified BSD image of a crack-like feature propagated from a pre-existing pit covered with mill scale near the center of the bend of sample 2, c) magnified BSD image of a crevice corrosion site covered with partially dissolved mill scale layer near the center of the bend of sample 10, d) magnified BSD image of a microcrack propagated from a corrosion pit near the center of the bend of sample 10, e) magnified BSD image of a crack-like feature with coarsened tip near the center of the bend of sample 10, and f) a short crack-like feature with coarsened tip propagated from a corrosion pit near the center of the bend of sample 10.

As visible in Figure 4.10 a) to b), the cross-sectional surface of sample 2 is, just as sample 1, mostly covered in the mill scale layer with occasional traces of coarsened microcracks formed as the result of crevice corrosion in the C2 solution, most of which were shorter than 10 μm . Although the surface of sample 10 is largely covered with the mill scale layer, corrosion pits and cracks on both sample surfaces and at the bottom of the crevice are more frequently observed than in sample 2, as is visible in Figure 4.10 c). Notably, as opposed to sample 2, the growth of microcracks and crevices are preferentially seen in the region near the center of the bend, as shown in Figure 4.10 d)-f). Figure 4.11 a) illustrates the comparison in the distribution of pits and cracks over the length of the samples mentioned above and control samples.



(a)

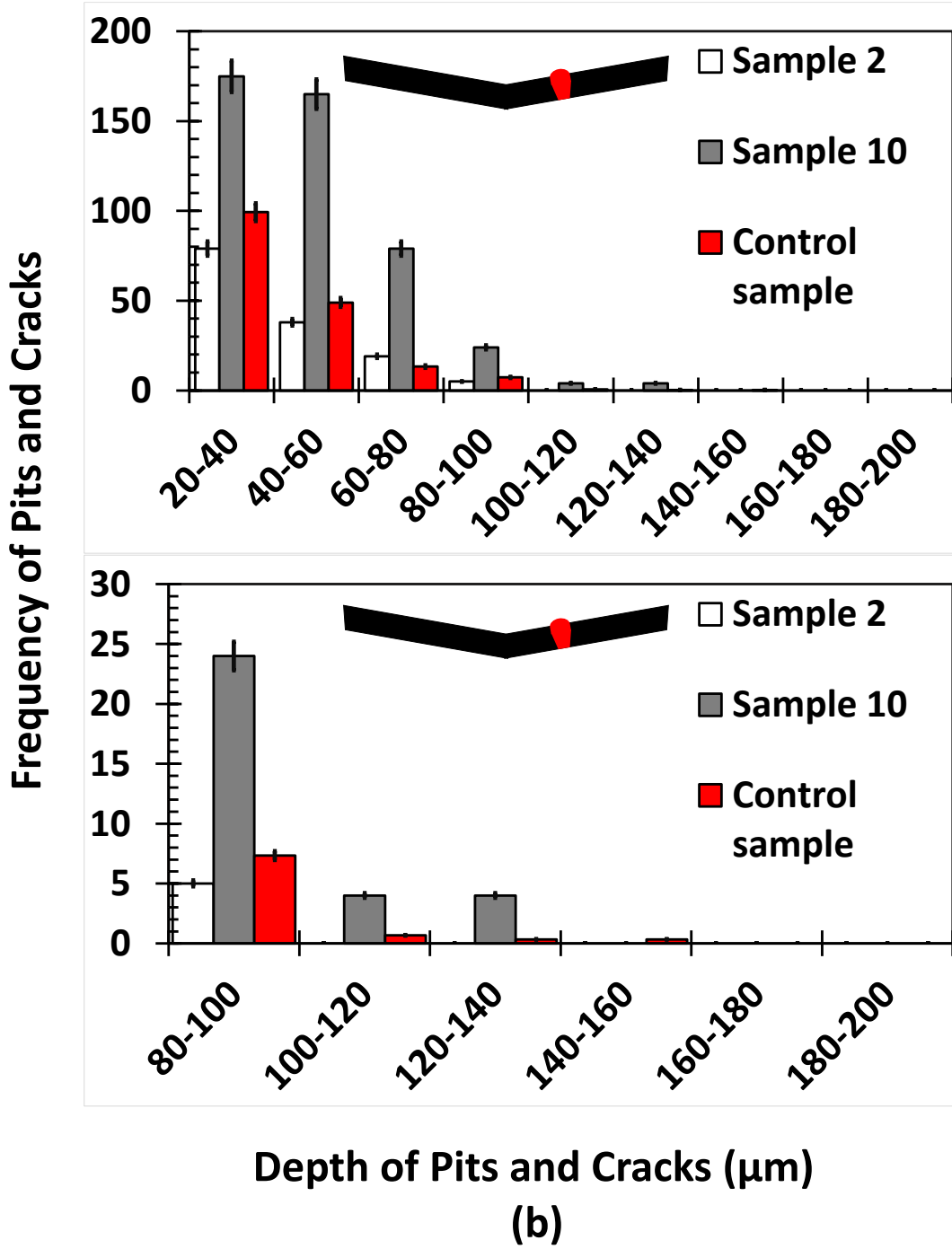


Figure 4.11 a) Distribution and b) frequency of pits and cracks in Sample 2 (90 days) & 10 (150 days) and control samples.

As can be seen, just as the trend observed between samples 1 and 9, sample 10 has more pits and cracks over the length, whereas the distribution in sample 2 does not deviate from the control samples. Notably, just as observed in the previous section, peaks of pits and cracks in sample 2 are seen at $|x| < 20$ mm, which is also observable in the control samples and sample 10. Furthermore, as opposed to sample 10, whose distribution of pits and cracks are somewhat symmetric at $|x| > 25$ mm and similar to control samples, sample 2 exhibits asymmetric distribution, particularly at $|x| > 40$ mm. Figure 4.11 b) shows the comparison of frequencies of pits and cracks with different depths in the samples. As can be seen, the overall frequencies in sample 2 are generally the same as or less than the control samples, whereas those in sample 10 overall show the highest values. Sample 2 exhibits no pits and cracks deeper than 100 μm , unlike sample 10. This is consistent with the assumption that a longer duration of static test will lead to higher frequencies of deeper pits and cracks.

4.2.3 Samples bent in tension with compressive residual stress on the surface ($d = 30$ mm)

As discussed in Chapter 3 and from the cross-sectional surface of control sample B, more exfoliated mill scale layers are expected to be observed on the surface of the samples with outward bending with respect to the OD. However, compressive bending residual stress remains on the OD surfaces during this process. As such, the depth of pits and cracks, especially around the center of the bend, may be significantly reduced.

Figure 4.12 a) to h) show the images of the cross-sectional surface morphologies of sample 3 (90 days) and 11 (150 days) taken by both BSD SEM and optical microscope.

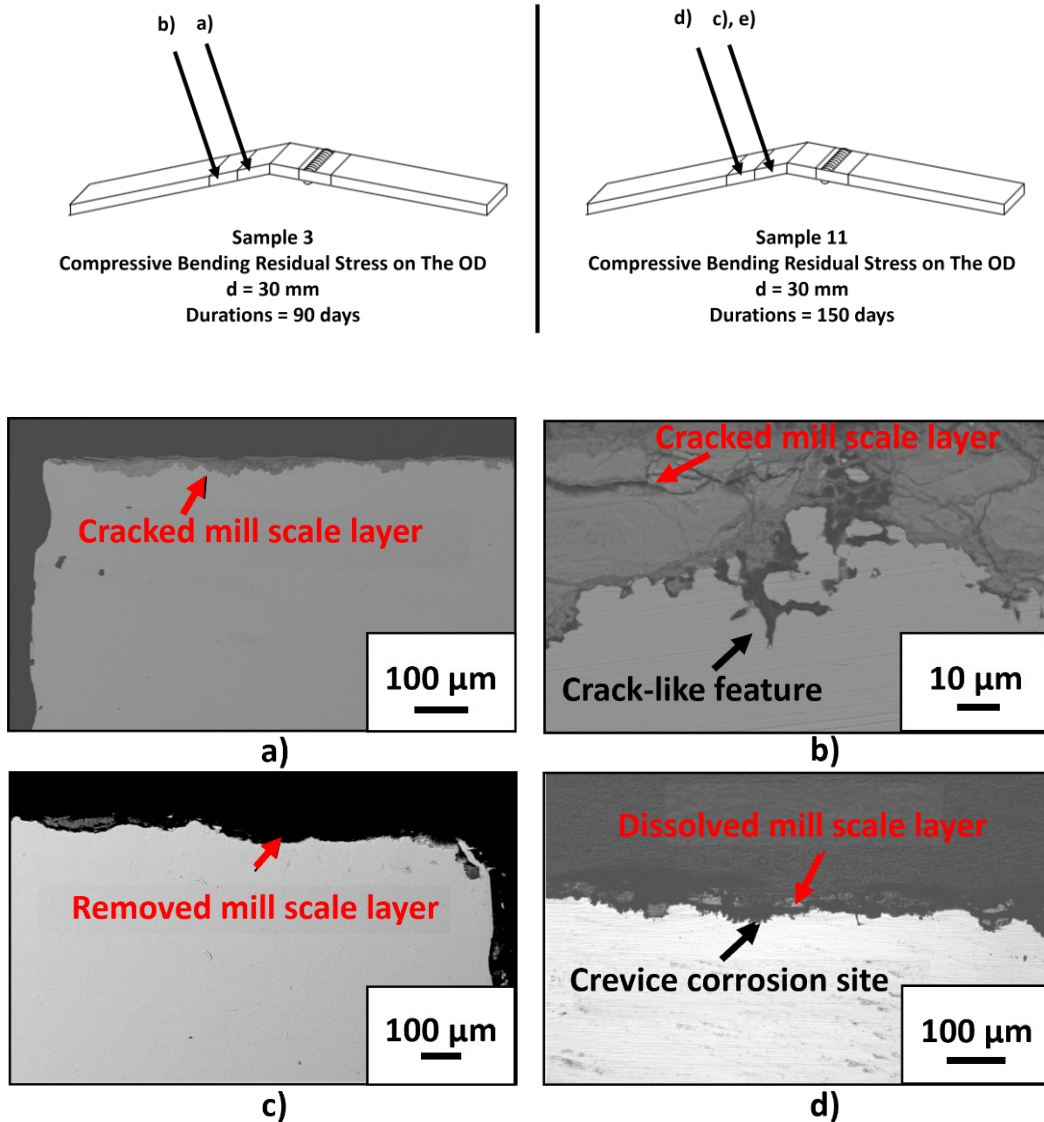
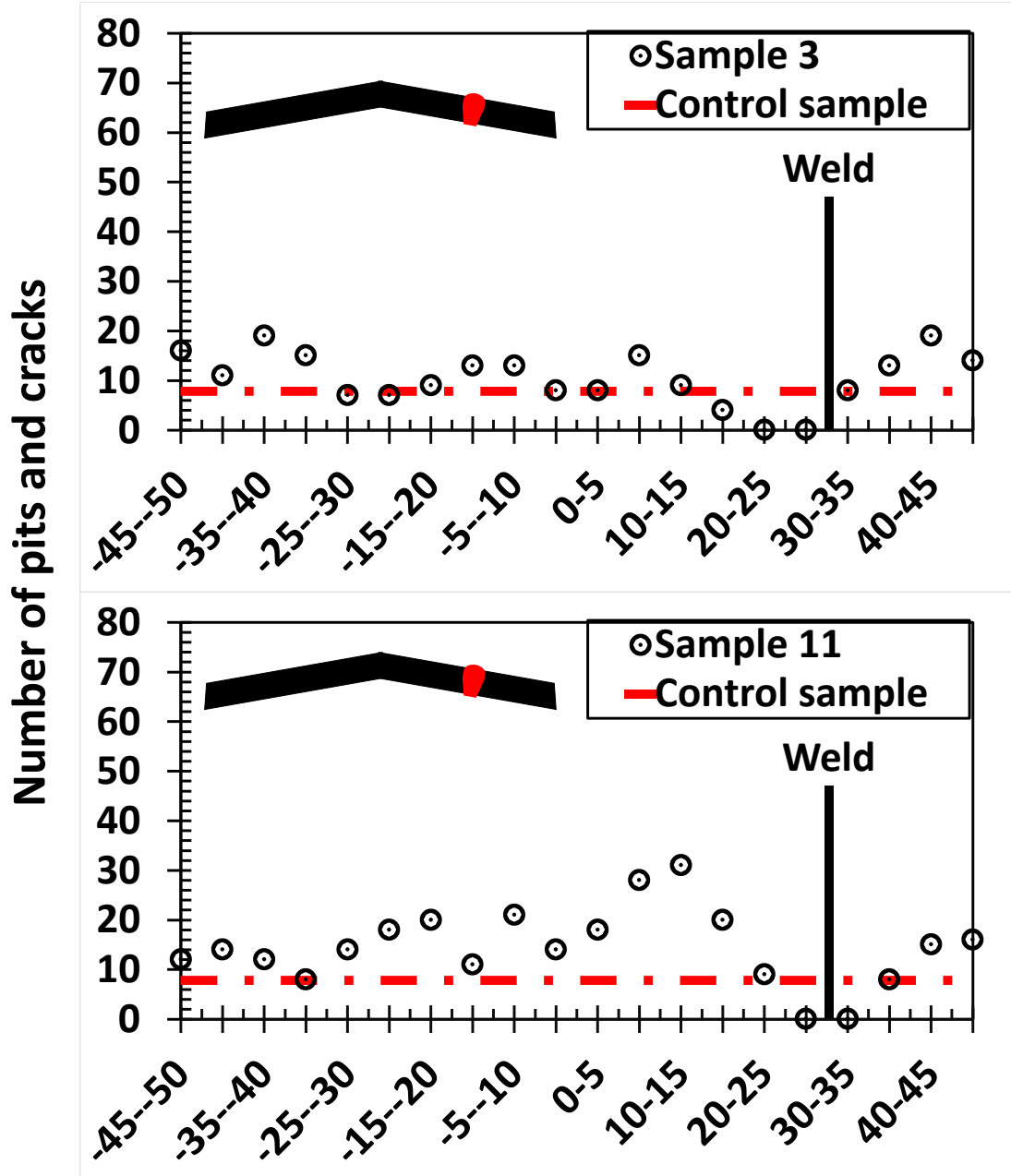


Figure 4.12 Schematics of Sample 3 & 11 as well as the cross-sectional surface morphologies of the samples; a) BSD image of sample 3 surface covered with cracked mill scale layer near the center of the bend, b) magnified BSD image of a crack-like feature propagated under mill scale layer near the area away from the center of the bend of sample 3, c) BSD image of sample 11 surface with dissolved mill scale near the center of the bend,

and d) OM image of crevice corrosion sites partially covered with dissolved mill scale layer in the region away from the center of the bend of sample 11.

As shown in Figure 4.12 a), the mill scale near the bend's center exhibits cracks, presumably formed because of mechanical bending. However, the complete exfoliation of the mill scale observed in control sample B was not observed on the surfaces. Similar to samples 1 and 2, pre-existing corrosion pits covered with fissured mill scale with a coarsened crack at the bottom are preferentially seen near the girth weld and away from the center of the bend, as illustrated in Figure 4.12 b). Just as in control sample B, near-complete removal of the mill scale is observed in sample 11, which is visible in Figure 4.12 c). Compared to sample 3 and the control samples, sample 11 contains a more significant number of enlarged pits resulting from crevice corrosion near the center of the bend, one of which is visible in Figure 4.12 d). Figure 4.13 a) compares the distribution of pits and cracks over the length between sample 3, sample 11, and control samples.



Distance from the center of the bend (mm)

(a)

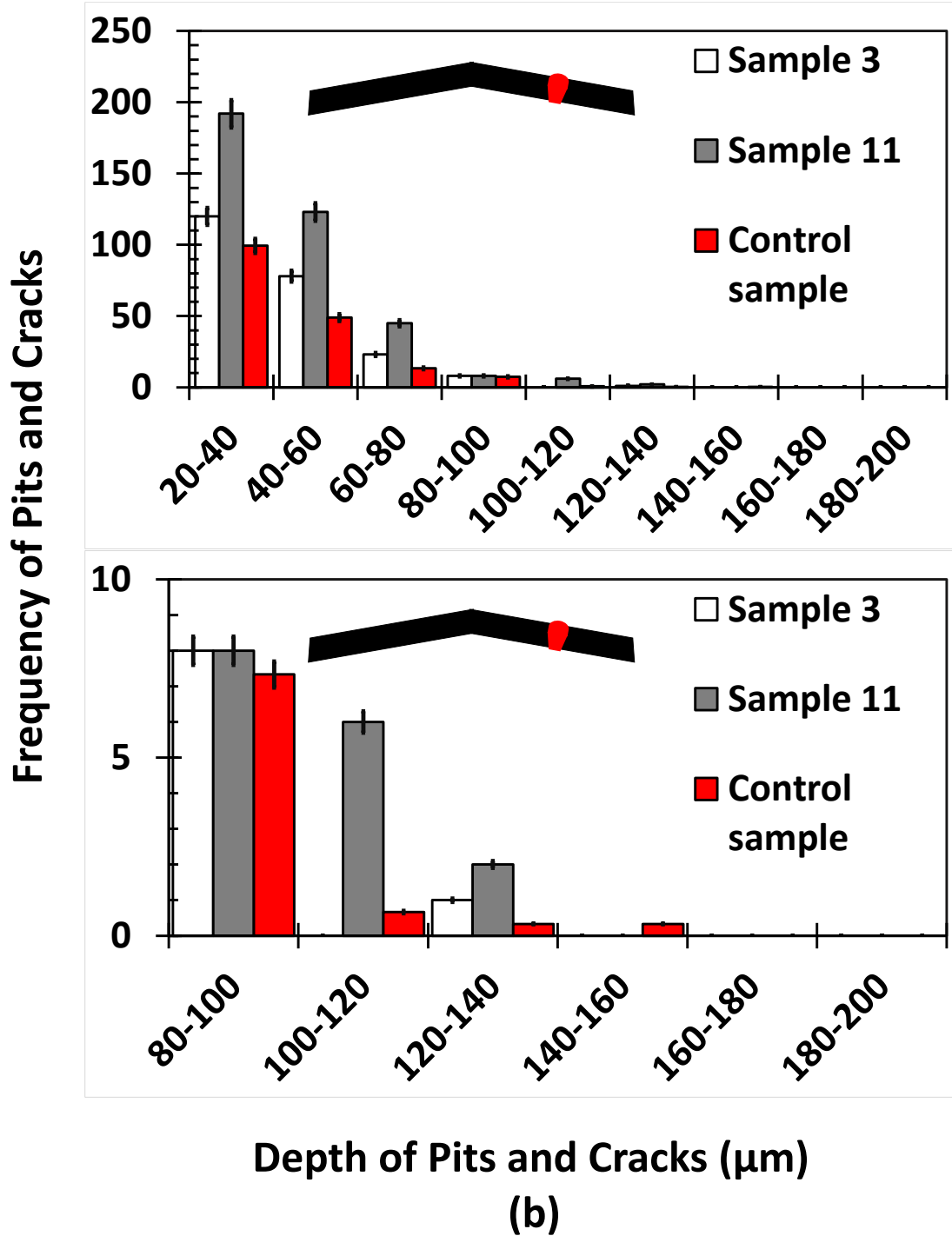


Figure 4.13 a) Distribution and b) frequency of pits and cracks in Sample 3 (90 days) & 11 (150 days) and control samples.

As can be seen, the distribution in sample 3 is somewhat symmetric and has its peak at $45 \text{ mm} < |x| < 50 \text{ mm}$. Although these peaked values exceed the distribution at the exact locations in control samples, the distributions near the center of the bend in sample 3 are lower than the control samples. On the other hand, sample 11 exhibits its peak at $10 \text{ mm} < x < 15 \text{ mm}$. Furthermore, the number of pits and cracks away from the center of the bend in sample 11 is lower than that in sample 3 despite the longer duration of the corrosion test. As mentioned above, the number of pits and cracks formed by crevice corrosion near the center of the bend is more significant in sample 11 than in sample 3. Figure 4.13 b) shows the comparison of frequencies of pits and cracks between sample 3, sample 11, and control samples. As can be seen, the frequencies of pits and cracks ($< 80 \mu\text{m}$) in samples 3 and 11 are higher than in control samples. Although the frequencies past $80 \mu\text{m}$ show almost no differences, sample 11 exhibits higher frequencies of pits and cracks deeper than $100 \mu\text{m}$. This is consistent with the result shown in the previous section.

4.2.4 Samples bent in tension with compressive residual stress on the surface ($d = 15 \text{ mm}$)

Figure 4.14 a) to c) show the cross-sectional surface morphologies of sample 4 (90 days).

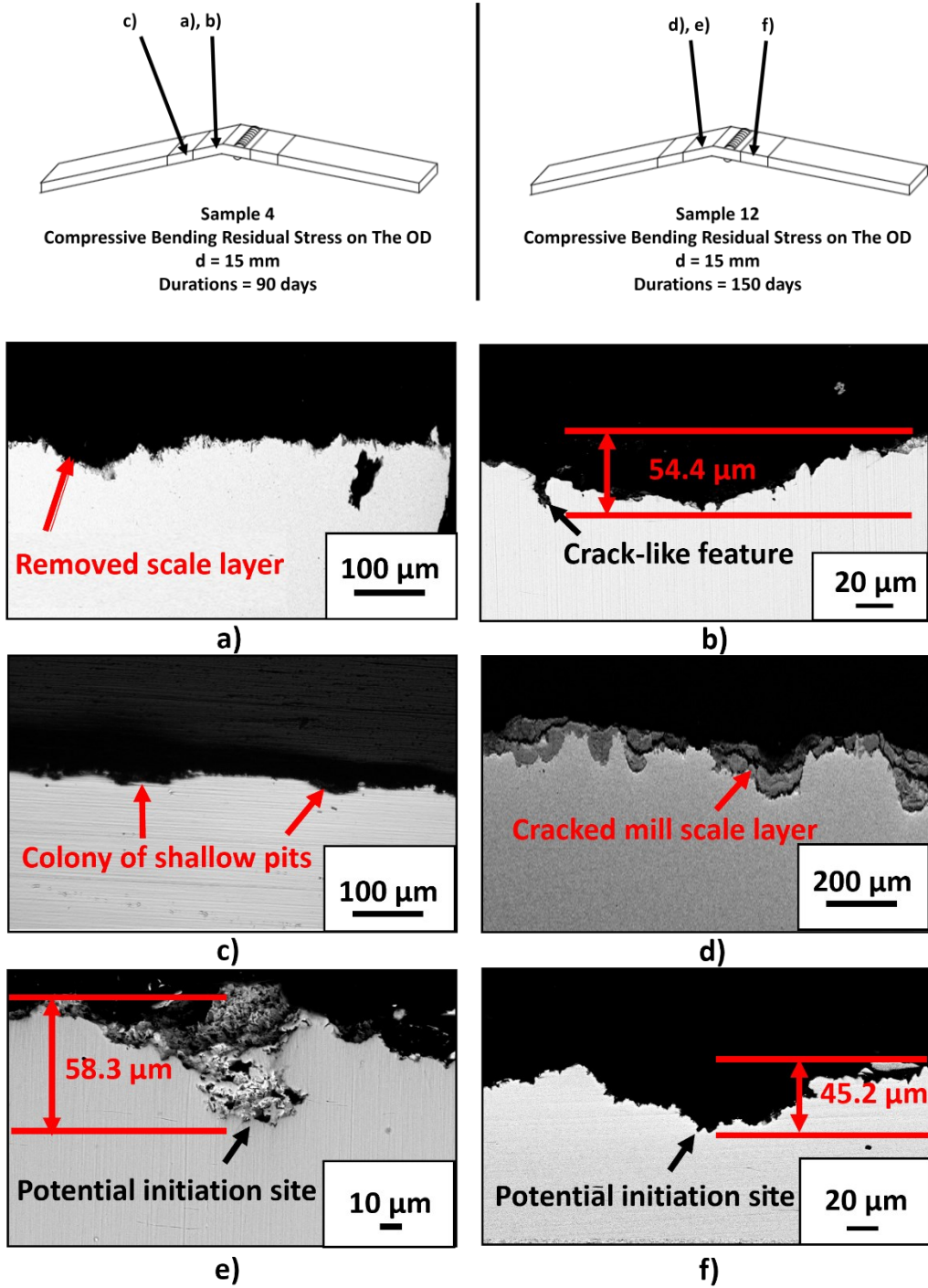
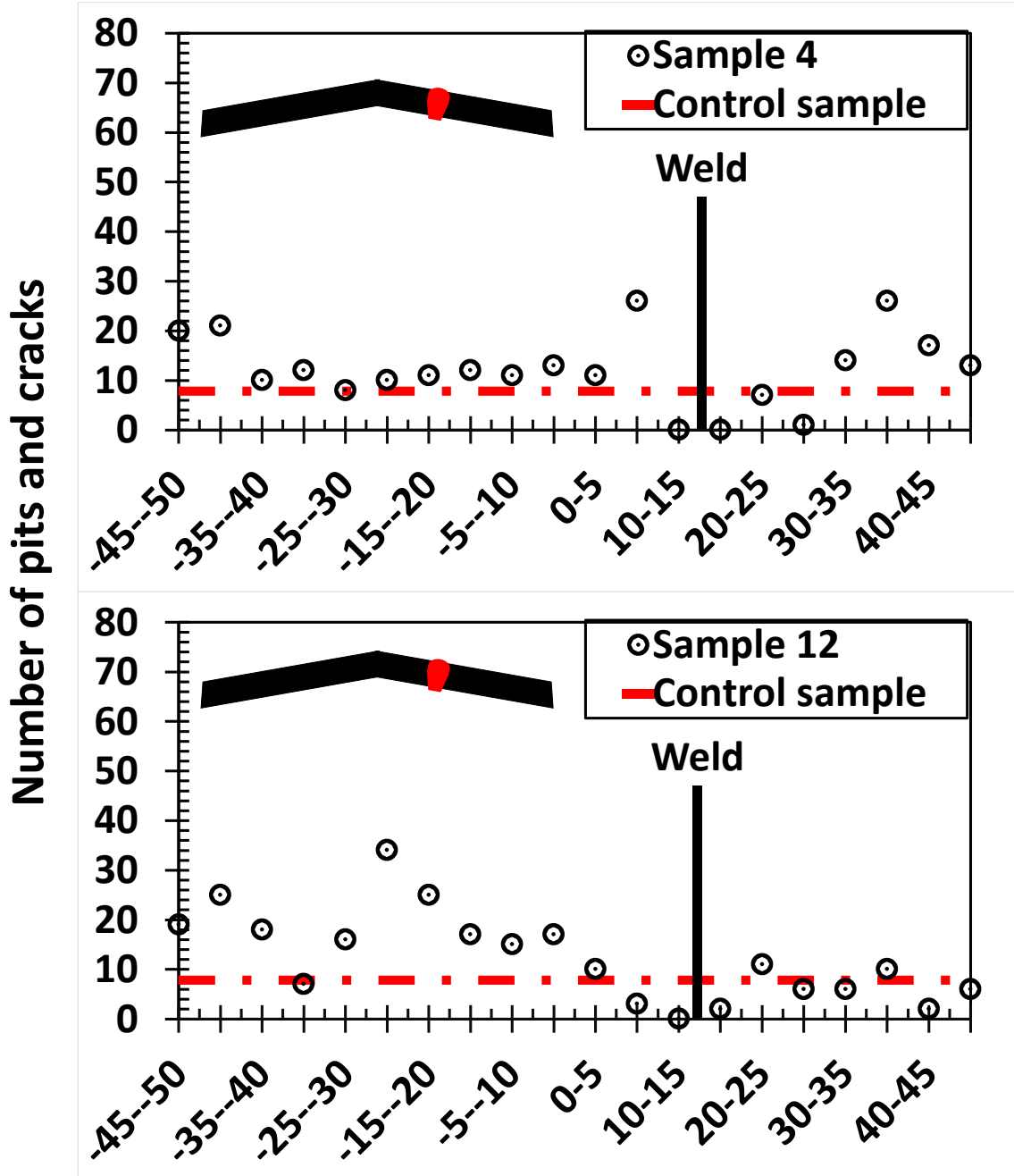


Figure 4.14 Schematics of Sample 4 & 12 as well as the cross-sectional surface morphologies of the samples. a) BSD image of sample 4 near the center of the bend, b)

magnified BSD image of corrosion pit with a crack-like feature near the center of the bend of sample 4, c) OM image of a colony of shallow pits found in the area way from the center of the bend of sample 4, d) BSD image of remaining mill scale covering the surface of sample 12 near the center of the ben, e)BSD image of a coarsened corrosion pit with sharp tips near the center of the bend of sample 12, and f) BSD image of a widened corrosion pit in the area away from the center of the bend of sample 12.

As seen in Figure 4.14 a), the mill scale layer at the center of the bend is thin and partially removed. Notably, a few crack-like features are observed at the center of the bend, one of which is visible in Figure 4.15 b). Furthermore, several small pits are observed away from the center of the bend, as shown in Figure 4.14 c). This indicates the mill scale layer at the said region was removed in the C2 solution. The cross-sectional surface morphologies of sample 12 (150 days) are visible in Figure 4.14 d) to f). As seen in Figure 4.14 d), the mill scale layer at the center of the bend is still intact. However, several cracks on the mill scale and crevice corrosion at the bottom of pre-existing pits are observable. This might have occurred because of the infiltration of the C2 solution at the bottom of the pits through the cracks formed by mechanical bending. Just as in sample 4, a few crack-like features, one shown in Figure 4.14 e), were observed. Furthermore, exfoliation of the mill scale layer away from the center of the bend was observed and is visible in Figure 4.14 f), just as observed in sample 4.

Figure 4.15 a) shows the comparison in terms of the distribution of pits and cracks over the length of samples 4, 12, and control samples.



Distance from the center of the bend (mm)

(a)

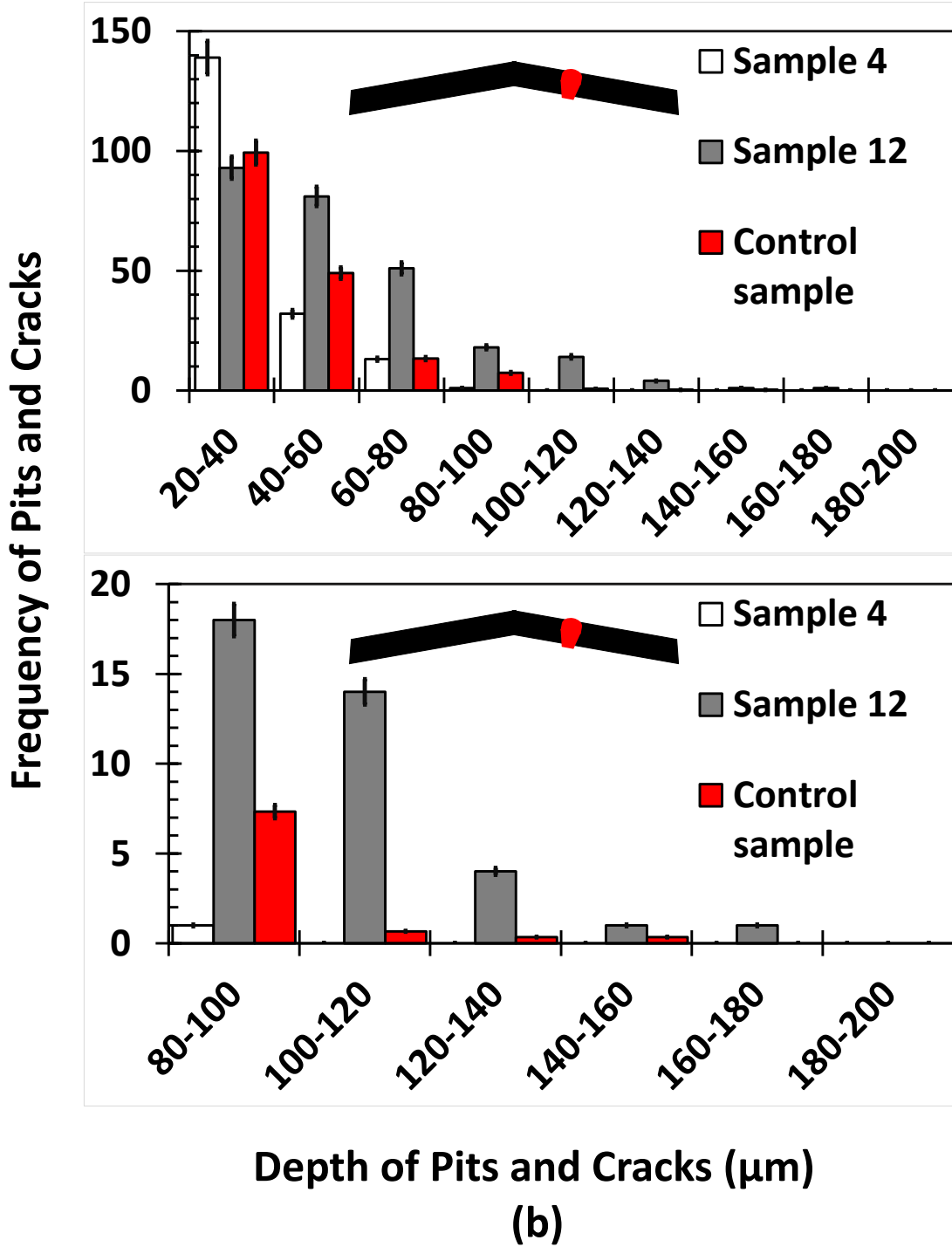


Figure 4.15 a) Distribution and b) frequency of pits and cracks in samples 4 (90 days) & 12(150 days) and control samples.

As can be seen, the peaks in sample 4 are observed at $x = 10$ mm and 40 mm, whereas the peak in sample 12 is at $x = -45$ mm. Both samples agree that the peaks are observable away from the center of the bend. Furthermore, the distribution in sample 2 is comparable to that in sample 4 and the control samples, despite the difference in the duration of the static test. Figure 4.15 b) shows the comparison between the said samples regarding the frequencies of pits and cracks with different depths. Sample 4 exhibits the highest frequency of shallow pits and cracks (< 40 μm), corresponding to the surface morphologies mentioned above. On the other hand, the highest frequency of pits and cracks deeper than 40 μm is exhibited by Sample 12, followed by the control samples.

4.2.5 Samples bent in compression with tensile residual stress on the surface ($d = 0$ mm)

Error! Reference source not found. a) to e) shows cross-sectional morphologies of samples 5 (90 days) and 13 (150 days).

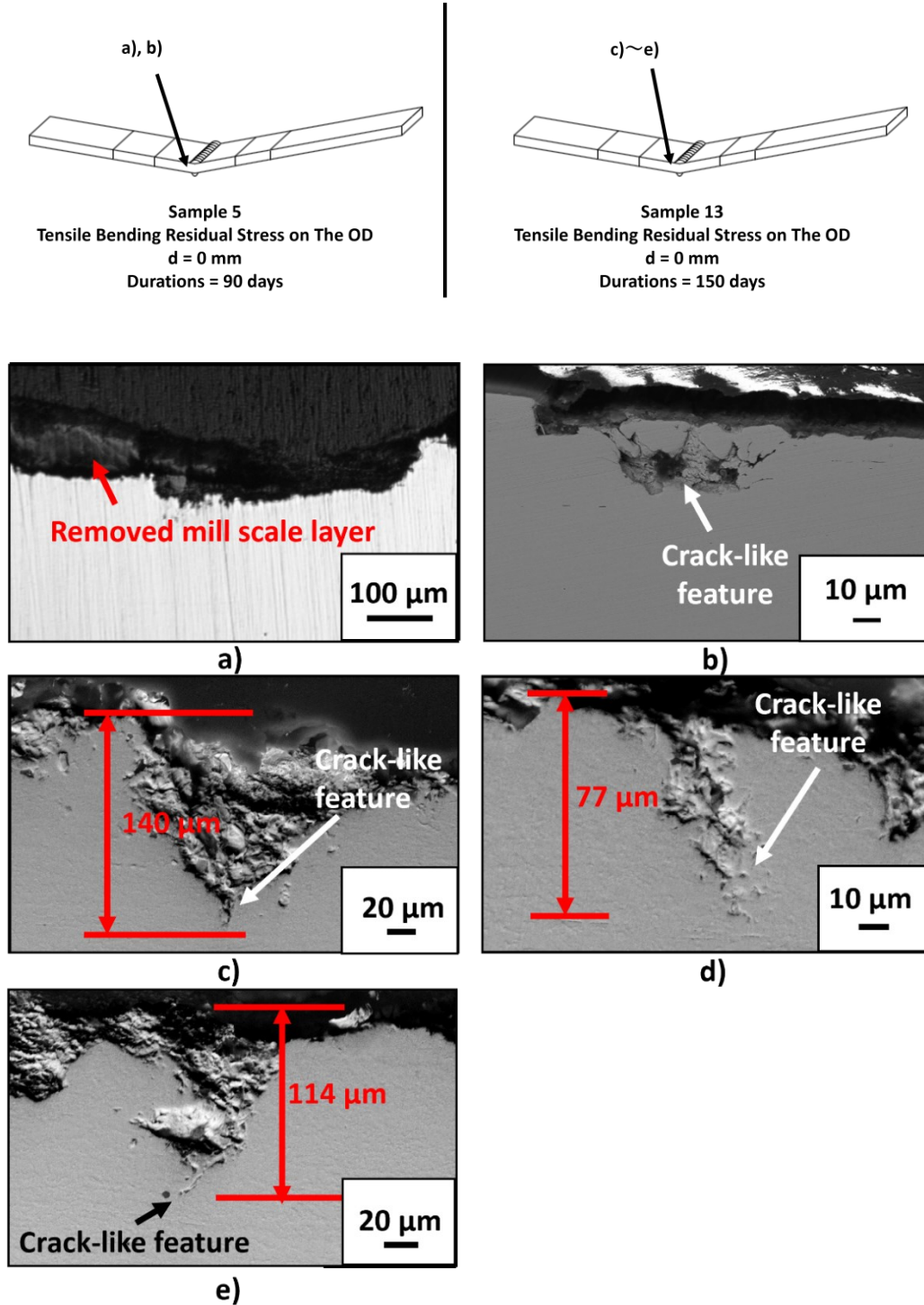
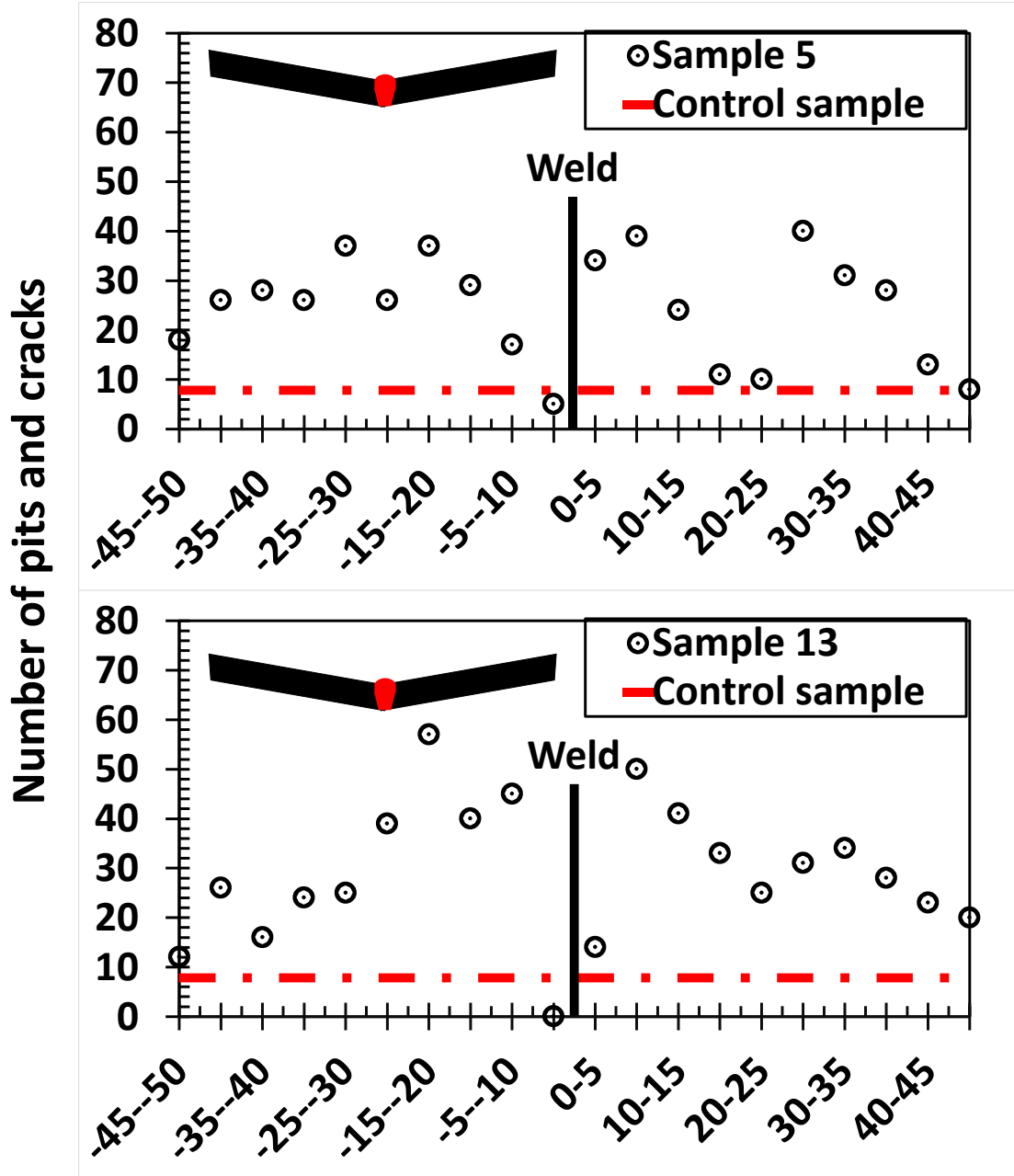


Figure 4.16 Schematics of Sample 5 & 13 as well as the cross-sectional surface morphologies of the samples; a) OM image of corrosion pits with exfoliated mill scale layer

near the center of the bend of sample 5, b) BSD image of cracks coalesced into a balloon-like pits near the center of the bend of sample 5, c) magnified BSD image of a large corrosion pit with sharp tip near the center of the bend of sample 13, d) magnified BSD image of a branched crack near the center of the bend of sample 13, and e) magnified BSD image of a crack-like feature propagated from a sharp corrosion pit in the area away from the center of the bend of sample 13.

Partial or complete exfoliation of the mill scale layer near and away from the center of the bend is observed, as shown in **Error! Reference source not found. a)**. Although the sample is symmetric, the morphologies of the mill scale layer and pits differ on both sides, as observed in the control samples. Several deep pits and cracks are observed near the center of the bend, as visible in **Error! Reference source not found. b)**. Sample 13 also exhibits several deep pits, ranging from around 70 to 140 μm , with crack-like features at the bottom, as shown in **Error! Reference source not found. c) to e)**. Figure 4.17 a) compares the distribution of pits and cracks relative to the center of the bend between samples 5 and 13, and control samples.



Distance from the center of the bend (mm)

(a)

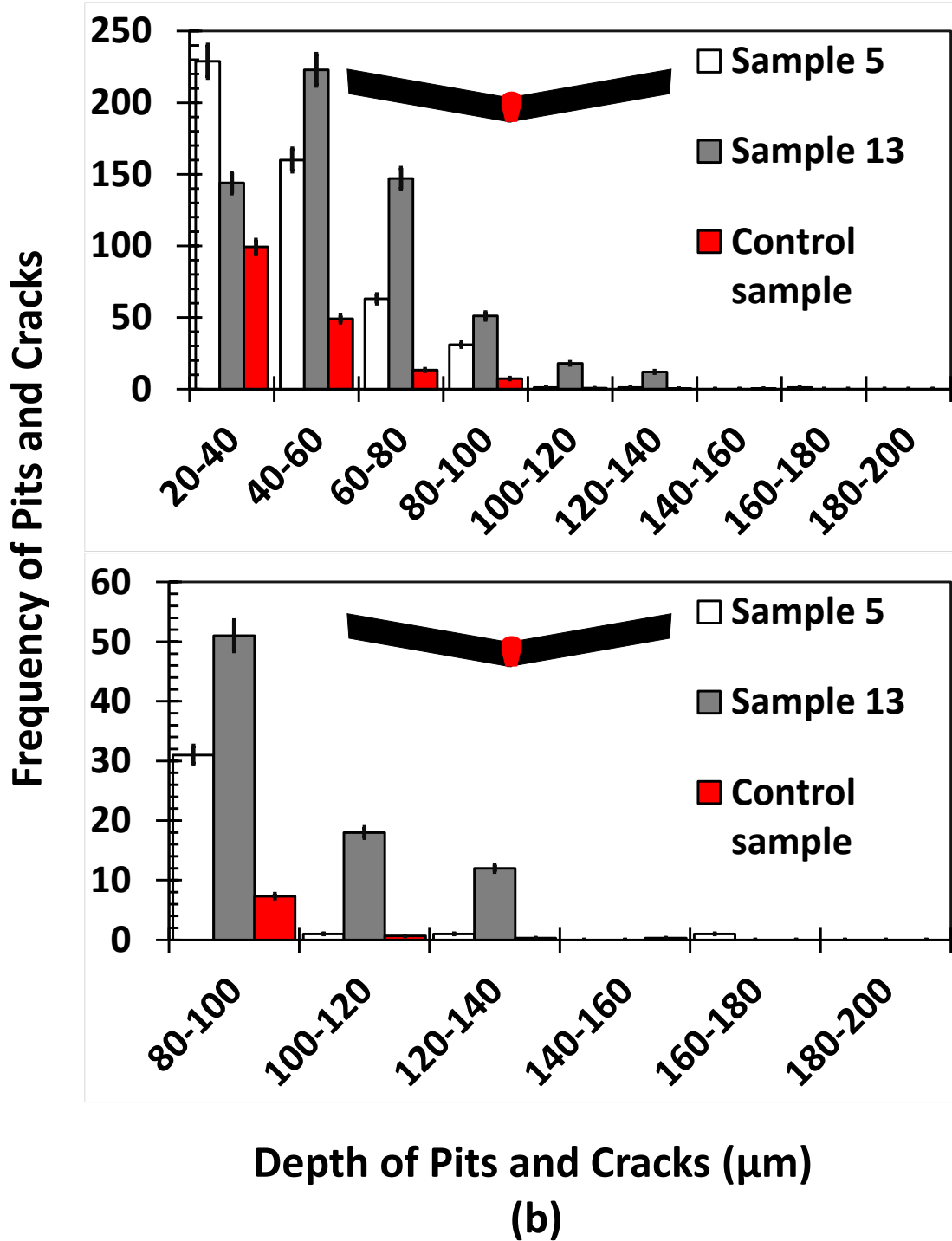


Figure 4.17 a) Distribution and b) frequency of pits and cracks in Sample 5 (90 days) & 13 (150 days) and control samples

As can be seen, the distributions of sample 13 are somewhat symmetric, and peaks are observed at $|x| = 20$ mm, whereas those of sample 5 are asymmetric and show peaks at $x = 10$ mm and $x = 30$ mm, which are higher than sample 13 at the exact same locations. Figure 4.17 b) shows the frequencies of pits and cracks with different depths in the above samples. As can be seen, sample 5 exhibits higher frequencies of shallow pits ($< 40 \mu\text{m}$), with the frequencies of deeper pits lower than those in sample 13. This indicates that the number of pits shown in Figure 4.17 a) are primarily shallow pits.

4.2.6 Samples bent in compression with tensile residual stress on the surface ($d = N/A$)

As mentioned in Chapter 3, samples with no girth welds were fabricated and characterized to compare the results with those in the samples with a weldment. Figure 4.18 a) to b) shows the cross-sectional surface morphologies of sample 6 (90 days).

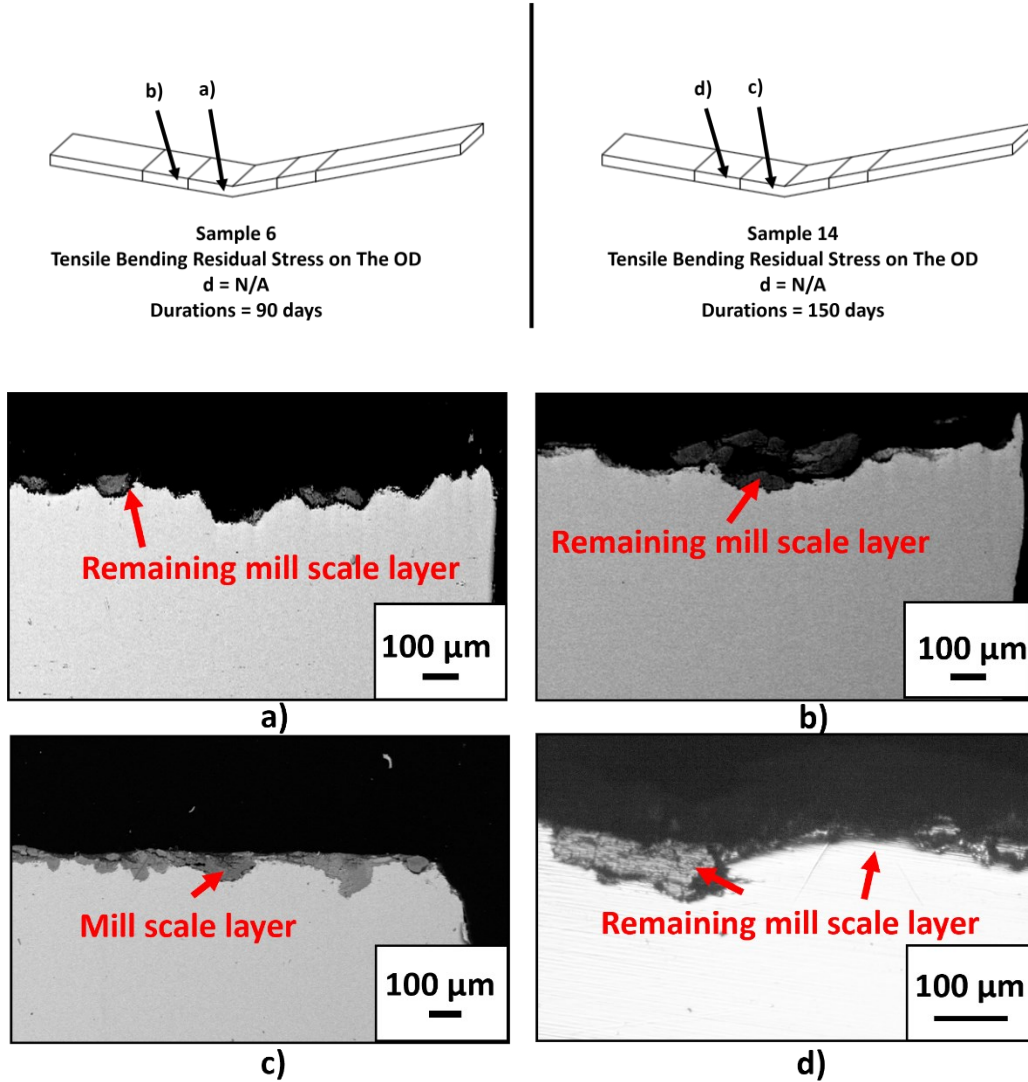
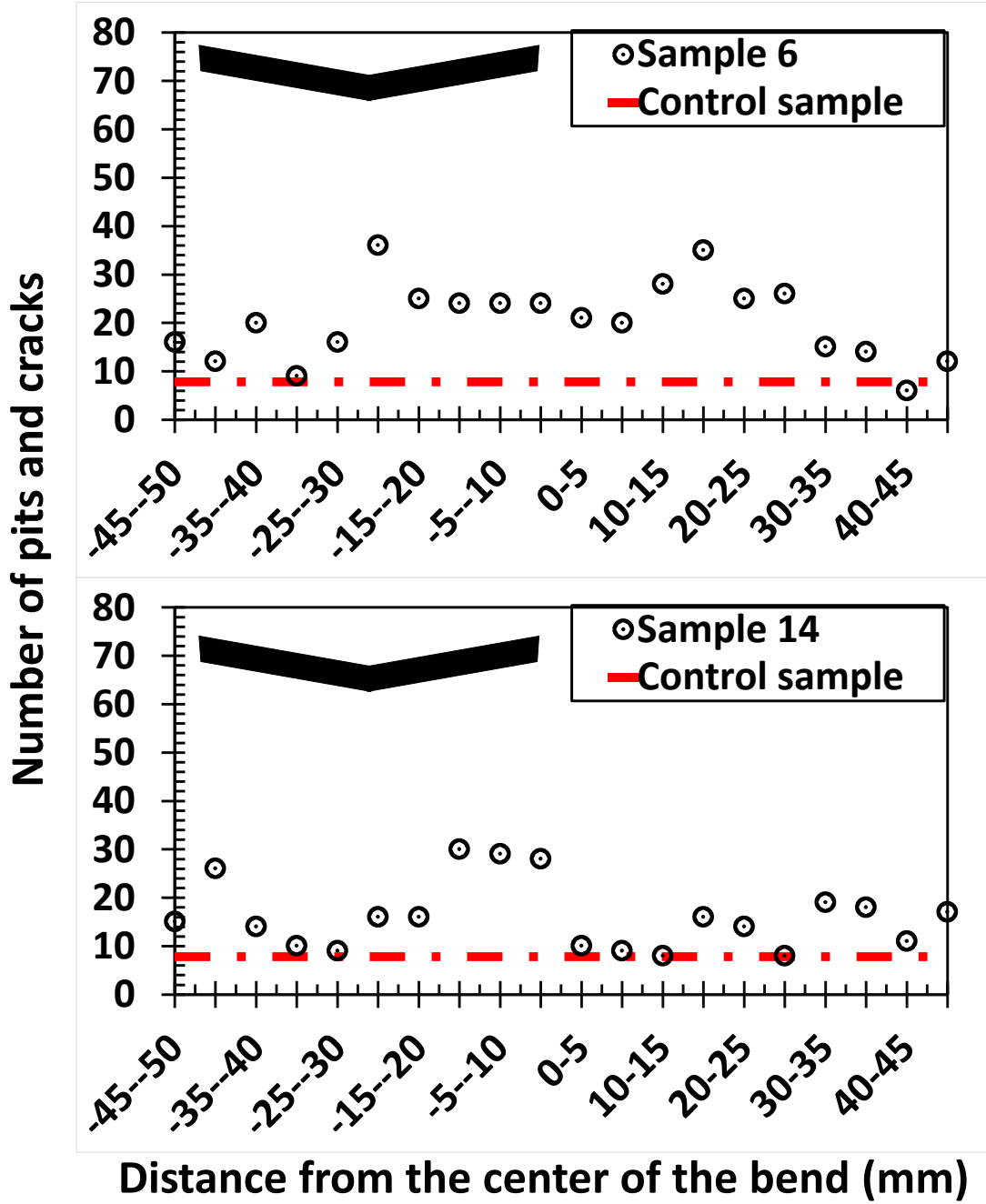


Figure 4.18 Schematics of Sample 6 & 14 as well as the cross-sectional surface morphologies of the samples; a) BSD image of sample 6 surface with partially exfoliated mill scale layer near the center of the bend and b) in the area away from the center of the bend, c) BSD image of thick mill scale layer covering the surface of sample 14 near the center of the bend, and d) OM image of partially dissolved mill scale covering the surface of sample 14 in the area away from the center of the bend.

As can be seen, compared to the control samples, the mill scale layer is largely exfoliated, regardless of the distances from the center of the bend. On the other hand, sample 14 (150 days) exhibits the surfaces covered with a mill scale layer, as visible in Figure 4.18 c) and d), despite its long exposure in the NNpH environment. This observation may be because of the difference in the initial conditions of the mill scale on the surface of the samples; that is, the mill scale layer on sample 6 might have been cracked and/or partially exfoliated before the static corrosion test, leading to the rapid dissolution of mill scale and the sample surface in the NNpH environment, whereas the mill scale layer on sample 14 was relatively thicker than that on sample 6 and exhibited less defects. Figure 4.19 a) shows the distribution of pits and cracks versus the distance relative to the center of the bend.



(a)

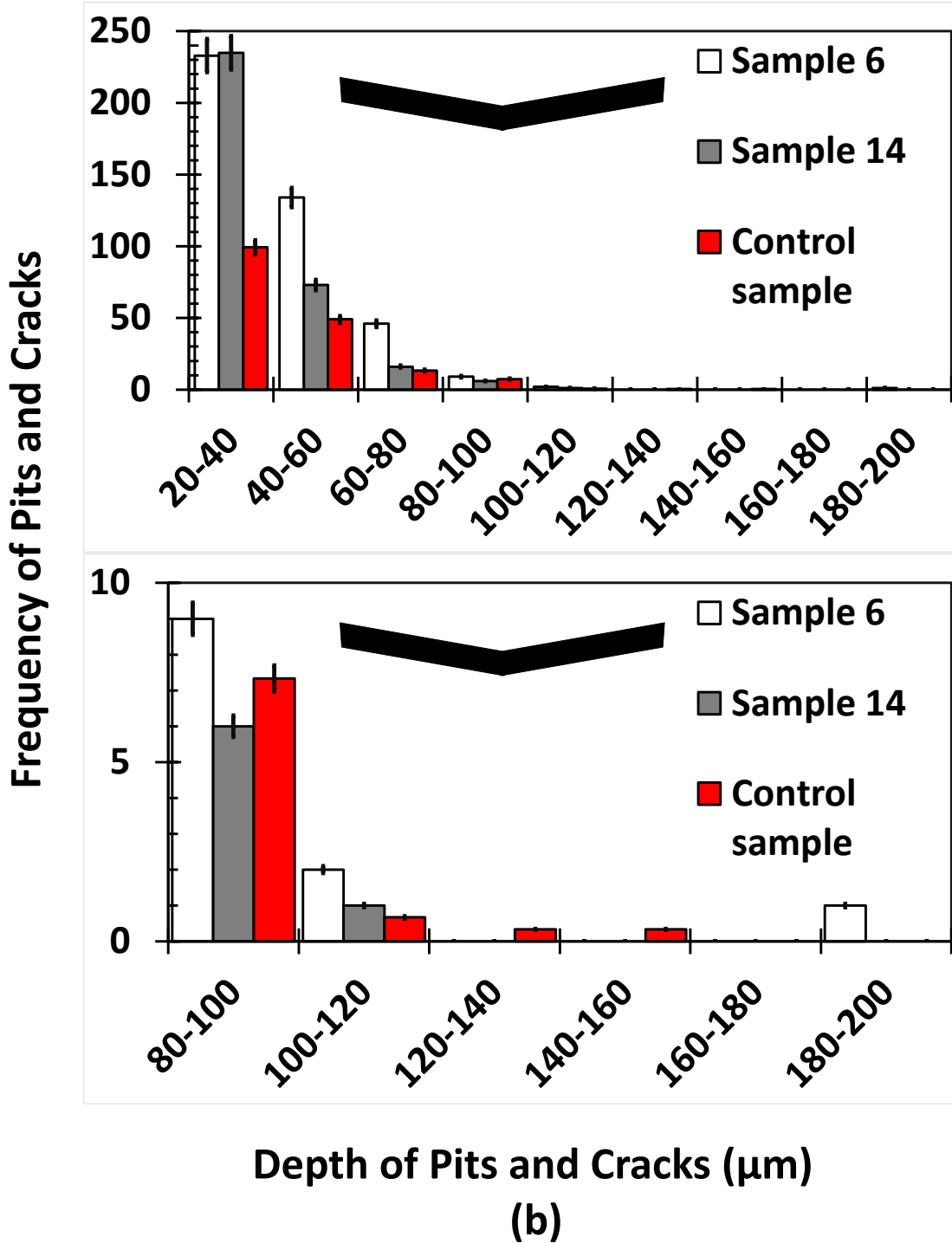


Figure 4.19 a) Distribution and b) frequency of pits and cracks in samples 6 (90 days) & 14 (150 days) and control samples.

As can be seen, the number of pits and cracks observed in sample 6 is overall higher than those in sample 14 at $x = 25$ mm. It must also be noted that the distribution in sample 6 is somewhat symmetric, while that in sample 14 shows no such tendency, particularly around $x = 20$ mm. Figure 4.19 b) shows the frequencies of pits and cracks with different depths. As can be seen, the overall frequencies in sample 6 are higher in sample 14, while the frequencies of 20-40 μm are comparable. Notably, the frequencies of pits and cracks deeper than 80 μm in samples 6 and 14 are comparable to those in control samples.

4.2.7 Samples bent in tension with compressive residual stress on the surface ($d = 0$ mm)

Cross-sectional surface morphologies of samples 7 (90 days) and 15 (150 days) are visible in Figure 4.20 a) to e).

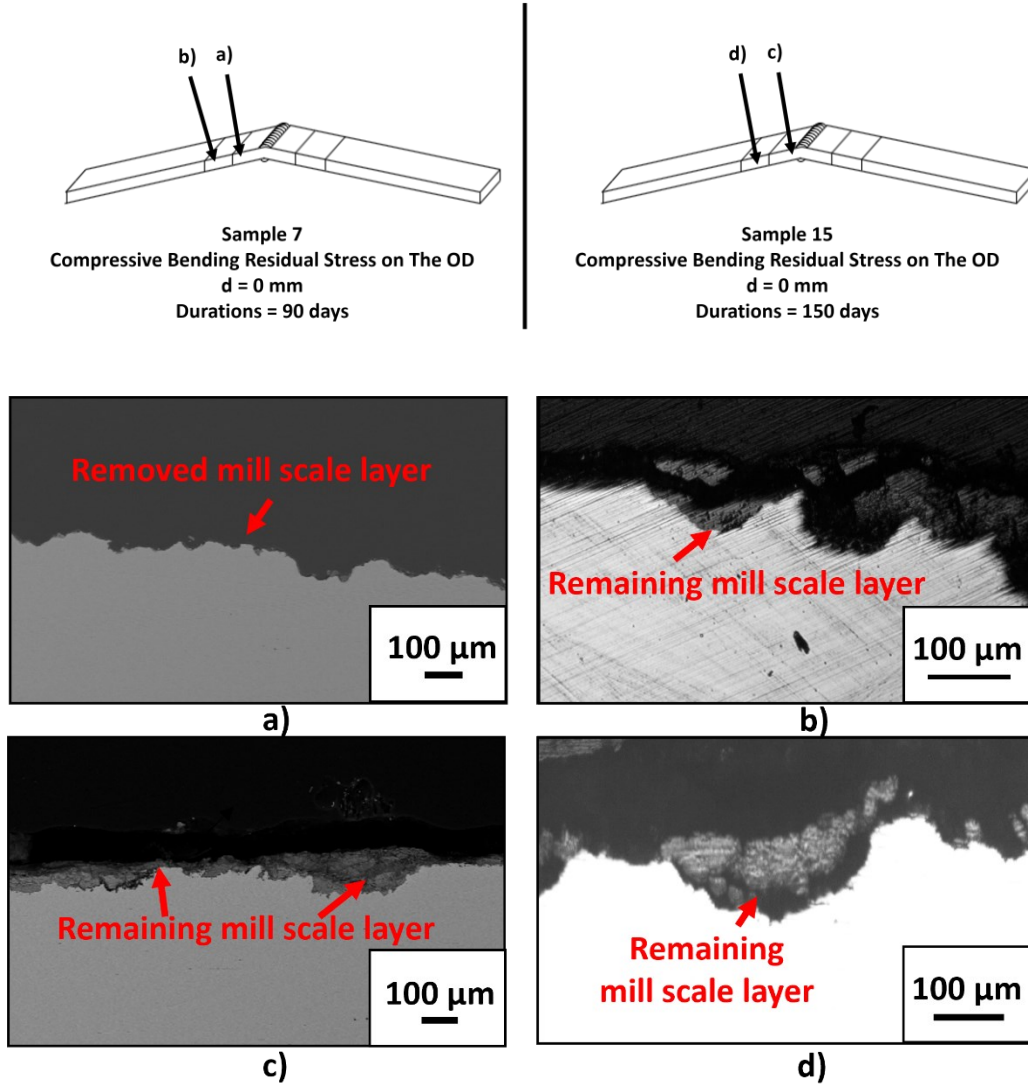
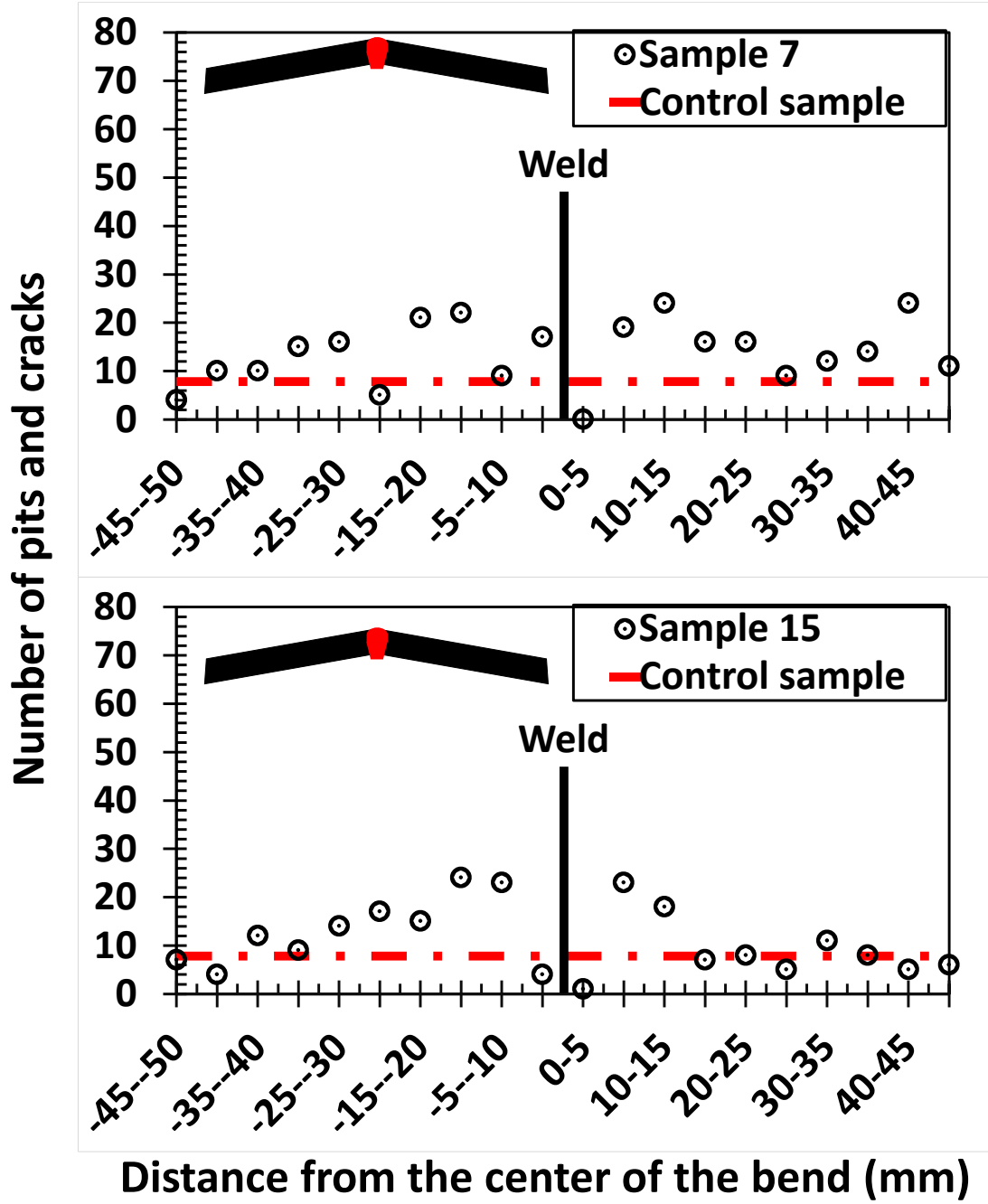


Figure 4.20 Schematics of Sample 7 & 15 as well as the cross-sectional surface morphologies of the samples; a) BSD image of a colony of corrosion pits with exfoliated mill scale layer on the surface of sample 7 near the center of the bend, b) OM image of the surface of sample 7 with largely exfoliated mill scale layer in the area away from the center of the bend, c) BSD image of the surface of sample 15 covered with mill scale layer near the center of the bend, and d) OM image of the surface of sample 15 with largely remaining mill scale in the area away from the center of the bend.

As shown in Figure 4.20 a), the mill scale layer's complete exfoliation is observable at the bend's center. Exfoliation of the mill scale is also observable away from the center of the bend, as shown in Figure 4.20 b), although most of the mill scale is still intact. Similar features are observed in sample 15, as shown in Figure 4.20 c) and d). The distribution of pits and cracks relative to the center of the bend, visible in Figure 4.21 a), shows that sample 15 exhibits overall higher distributions than sample 7 and the control samples.



(a)

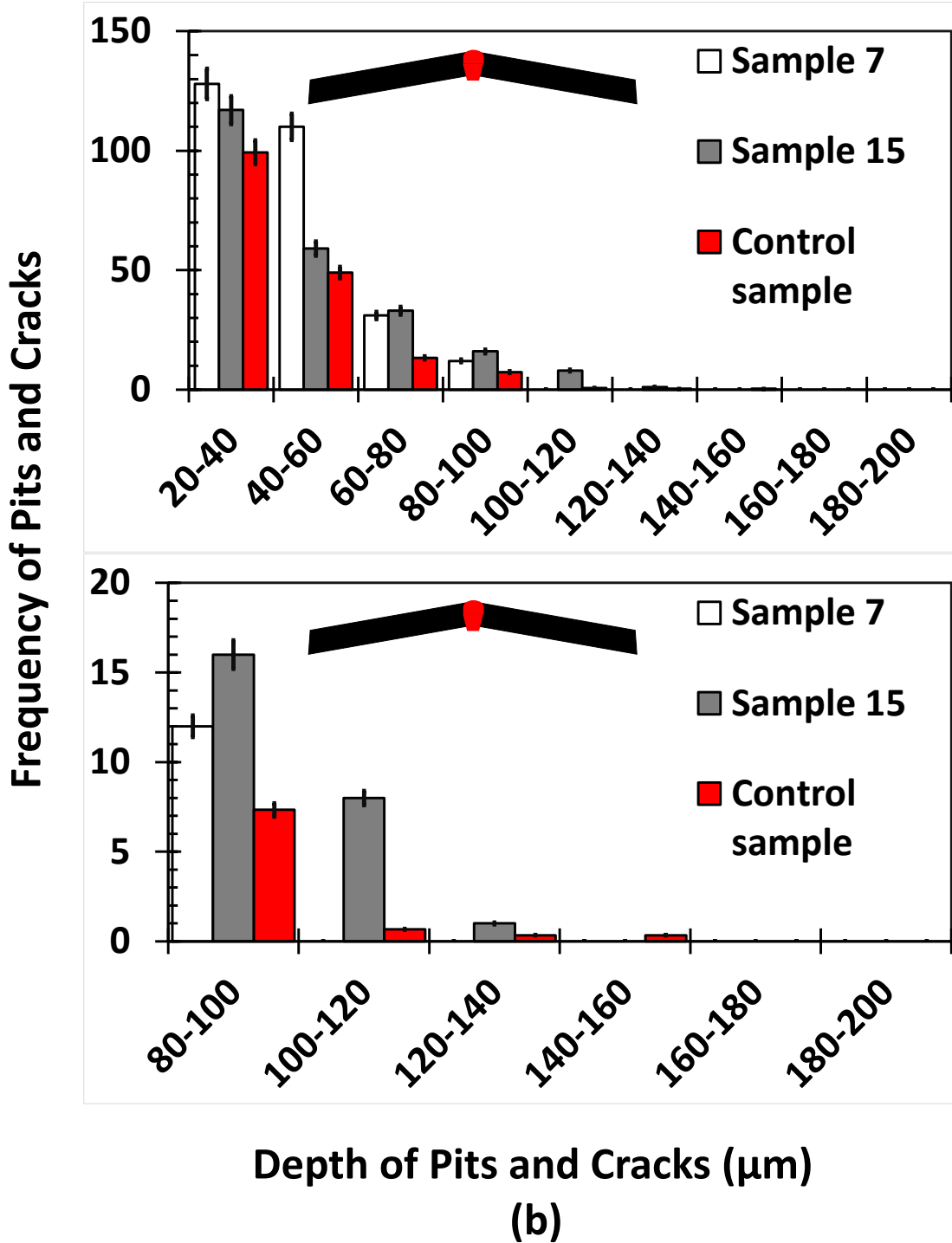


Figure 4.21 Distribution and frequency of pits and cracks in Samples 7 (90 days) & 15 (150 days) and control samples.

The frequencies of pits and cracks with different depths in Figure 4.21 b) also show the increase in the number of pits and cracks in samples 7 and 15 compared to the control samples. Comparison between samples 7 and 15 shows the increase in shallow pits ($< 60 \mu\text{m}$) after more prolonged exposure to the C2 environment. However, sample 15 exhibits higher frequencies of pits and cracks deeper than $60 \mu\text{m}$ than sample 7, particularly between $100\text{-}120 \mu\text{m}$.

4.2.8 Samples bent in tension with compressive residual stress on the surface ($d = \text{N/A}$)

Figure 4.22 a) to d) shows the cross-sectional surface morphologies of samples 8 (90 days) and 16 (150 days).

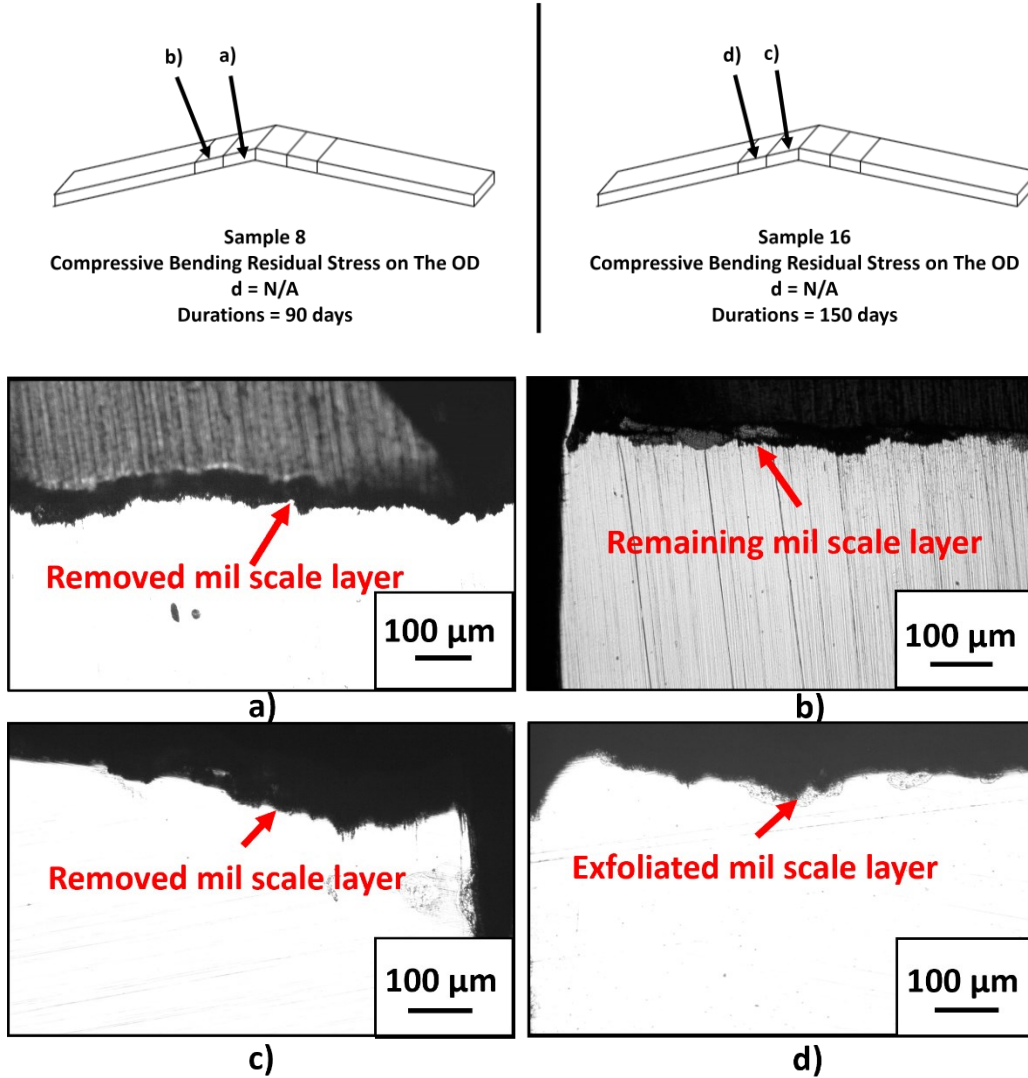
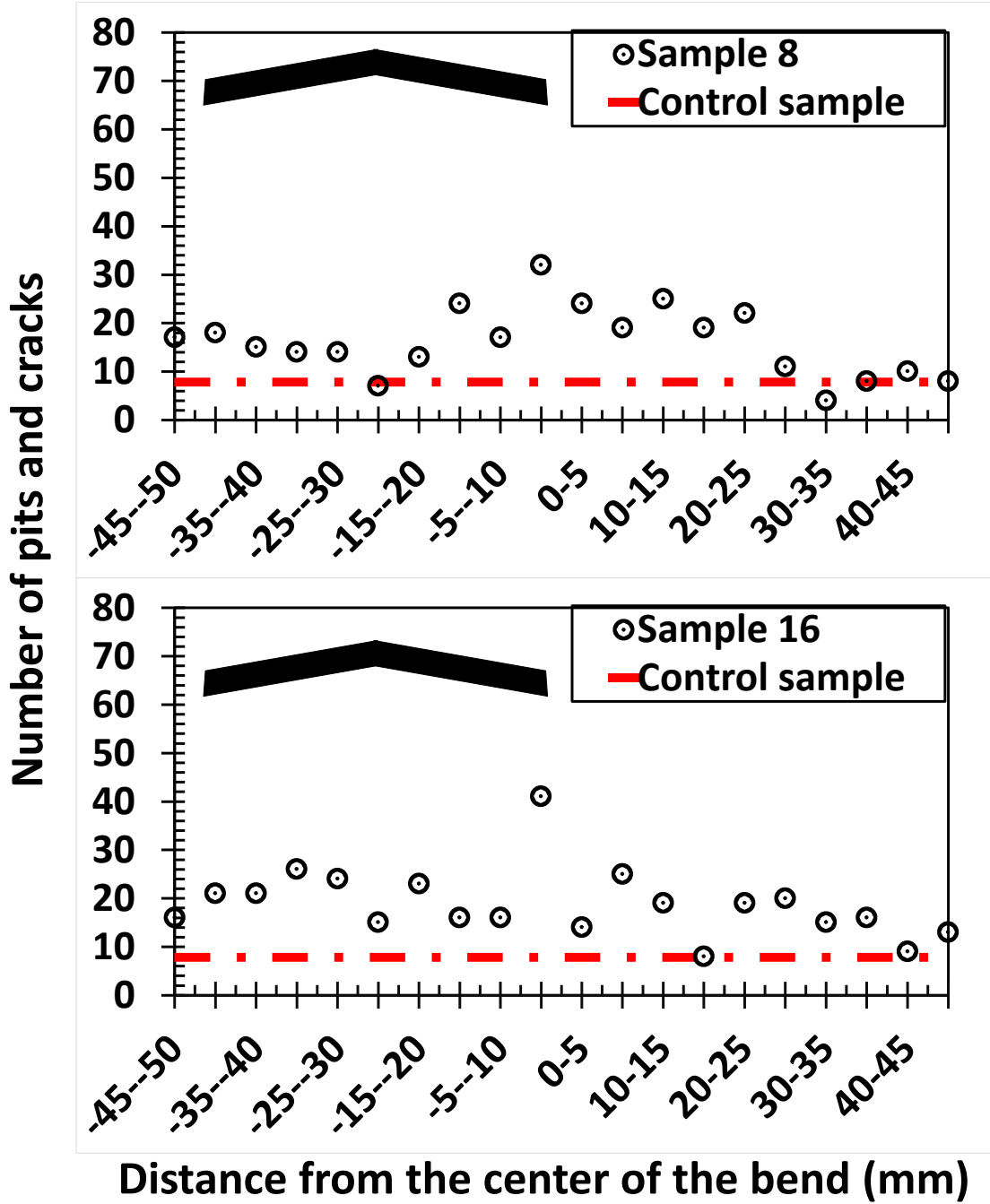


Figure 4.22 Schematics of Sample 8 & 16 as well as the cross-sectional surface morphologies of the samples; a) OM image of the surface of sample 8 with exfoliated mill scale near the center of the bend, b) OM image of the surface of sample 8 with partially exfoliated mill scale in the area away from the center of the bend, c) OM image of the surface of sample 16 with exfoliated mill scale near the center of the bend, and d) OM image of sample 16 surface with exfoliated mill scale in the area away from the center of the bend.

Sample 8 exhibits the colonies of small pits around the center of the bend, as shown in Figure 4.22 a) and b). Both samples 8 and 16 show complete exfoliation of the mill scale layer at the center of the bend, as visible in Figure 4.22 a) and b). Furthermore, as shown in Figure 4.22 c) and d), the exfoliation of the mill scale layer in the regions away from the center of the bend was confirmed in both samples 8 and 16, showing no significant differences. Figure 4.23 a) shows the distribution of pits and cracks in the samples and control samples.



(a)

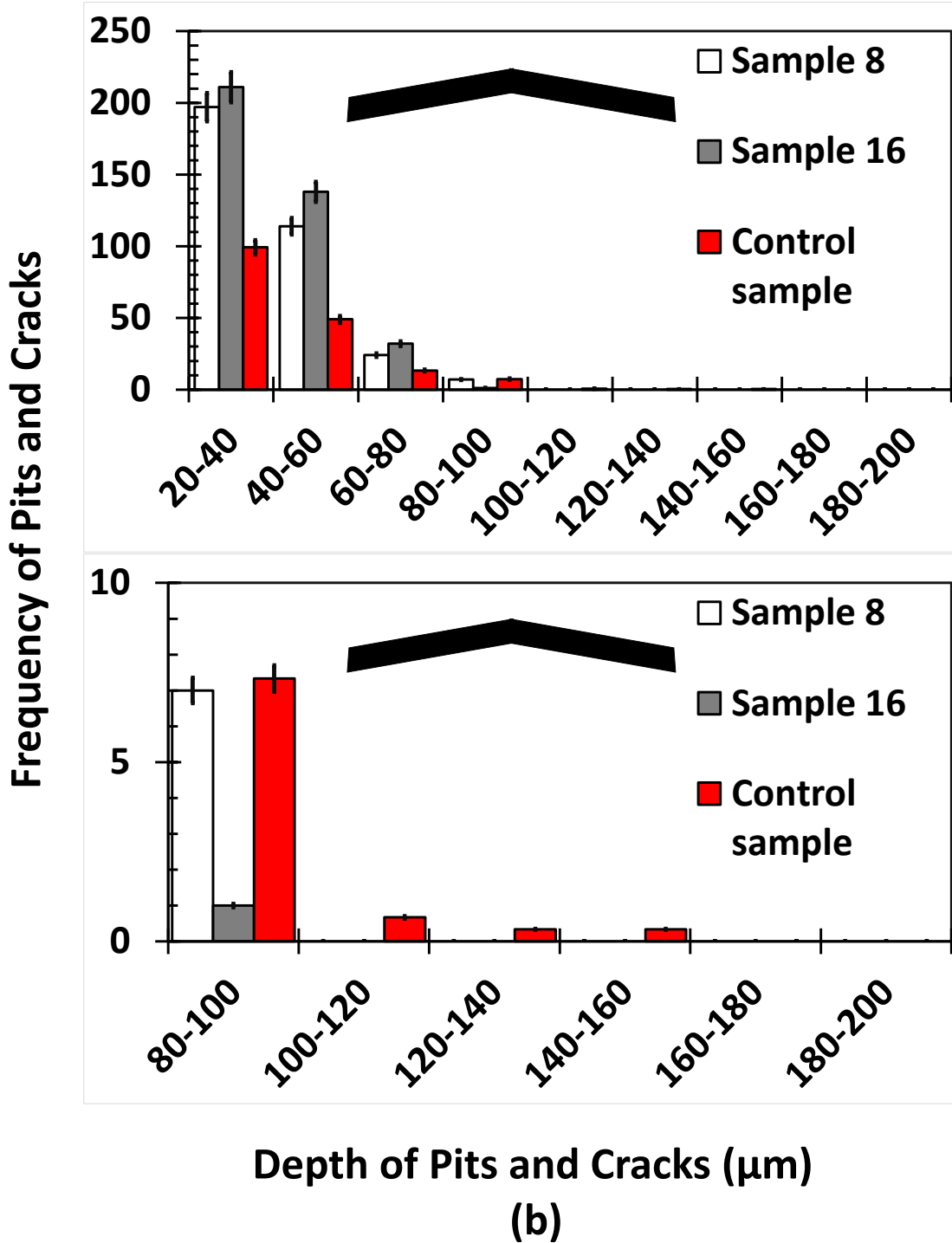


Figure 4.23 a) Distribution and b) frequency of pits and cracks in samples 8 & 16 and control samples.

The number of pits and cracks observed in samples 8 and 16 are overall higher than the control samples, although the numbers are somewhat comparable. While the distributions in sample 16 at $x < 0$ mm are higher than in sample 8, the opposite tendency is observed at $x > 0$ mm. Figure 4.23 b) shows the frequencies in the above samples with different depths. As can be seen, the overall frequencies in sample 16 are higher than in sample 8 and the control samples, which is consistent with the theory. However, the frequency of pits and cracks deeper than $80\ \mu\text{m}$ in samples 8 and 16 are comparable to the control samples, with sample 8 showing a higher frequency than sample 16. This indicates that the growth of pits and cracks under the conditions mentioned above was limited to $80\ \mu\text{m}$.

Chapter 5 : Discussion

While the initiation and early growth of C-NNpHSCC were observed in some of the corroded samples, the presence of mill scale heavily affected the results of static corrosion tests. As such, the accuracy of the data used for discussions and conclusions may be variable because of the variation in mill scale.

The mechanism of initiation and Stage I growth of NNpHSCC is, as explained in section 2.5.1, the anodic dissolution and crack transition from the tip of localized corrosion sites with the help of residual and applied stresses. Since there is no applied stress in this experiment, only the localized corrosion and residual stresses induced by girth weld and bending contribute to corrosion and pitting, which is further diversified because of the bend angles and the distance between the center of the bend and WCL (d). As such, the higher number of deep defects indicates an ideal residual stress gradient in depth for the initiation and Stage I growth, thereby determining the most susceptible combination of bend angle and d . Hence, the criteria for evaluating the significance of the initiation and Stage I growth of C-NNpHSCC are the number of deep pits and cracks ($> 80 \mu\text{m}$) on the samples. This is because the samples exhibiting a high number of deep defects in the same duration of static corrosion test will likely experience the early transition to Stage II growth of C-NNpHSCC if the necessary factors, such as cyclic loading, are provided. Indeed, the deep defects on the samples may have existed under the mill scale layer before the static corrosion tests. As such, the overall distribution of defects over the length of samples is also considered to minimize the errors. Although the significance of shallow defects ($< 80 \mu\text{m}$) is lower than the deep defects formed over the same durations, the discussion on small defects is also

briefly mentioned in this chapter, as the crack initiation and growth from shallow defects on the surface of the pipe is possible in the realistic environment[50].

This chapter discusses the effect of axial welding residual stress distribution on the OD with respect to WCL and its effect on C-NNpHSCC. Second, the effect of tensile and compressive bending residual stress on the OD on C-NNpHSCC and welding residual stress is discussed. Finally, the effect of durations of static corrosion tests on surface morphologies on the corroded samples is discussed.

5.1 Effect of Welding Residual Stress on Pits & Cracks Morphologies and Distributions

As mentioned in the previous sections, this research aims to investigate the interaction between bending residual stress and welding residual stress and its effect on C-NNpHSCC. While the typical welding axial residual stress distribution caused by the girth weld is well known and shown in section 2.3, the effect of several external factors, such as the stress relaxation because of the applied loading in service and sectioning, must not be ignored. As such, estimating the residual stress distribution of the lab-scale samples is essential.

Figure 5.1 a) and b) show the distributions of pits and cracks relative to the center of the bend with a) tensile bending residual stress and b) compressive residual stress on the OD with varying d . The frequency of pits and cracks in different depths on the corroded samples are visible in Figure 5.2 a) and b).

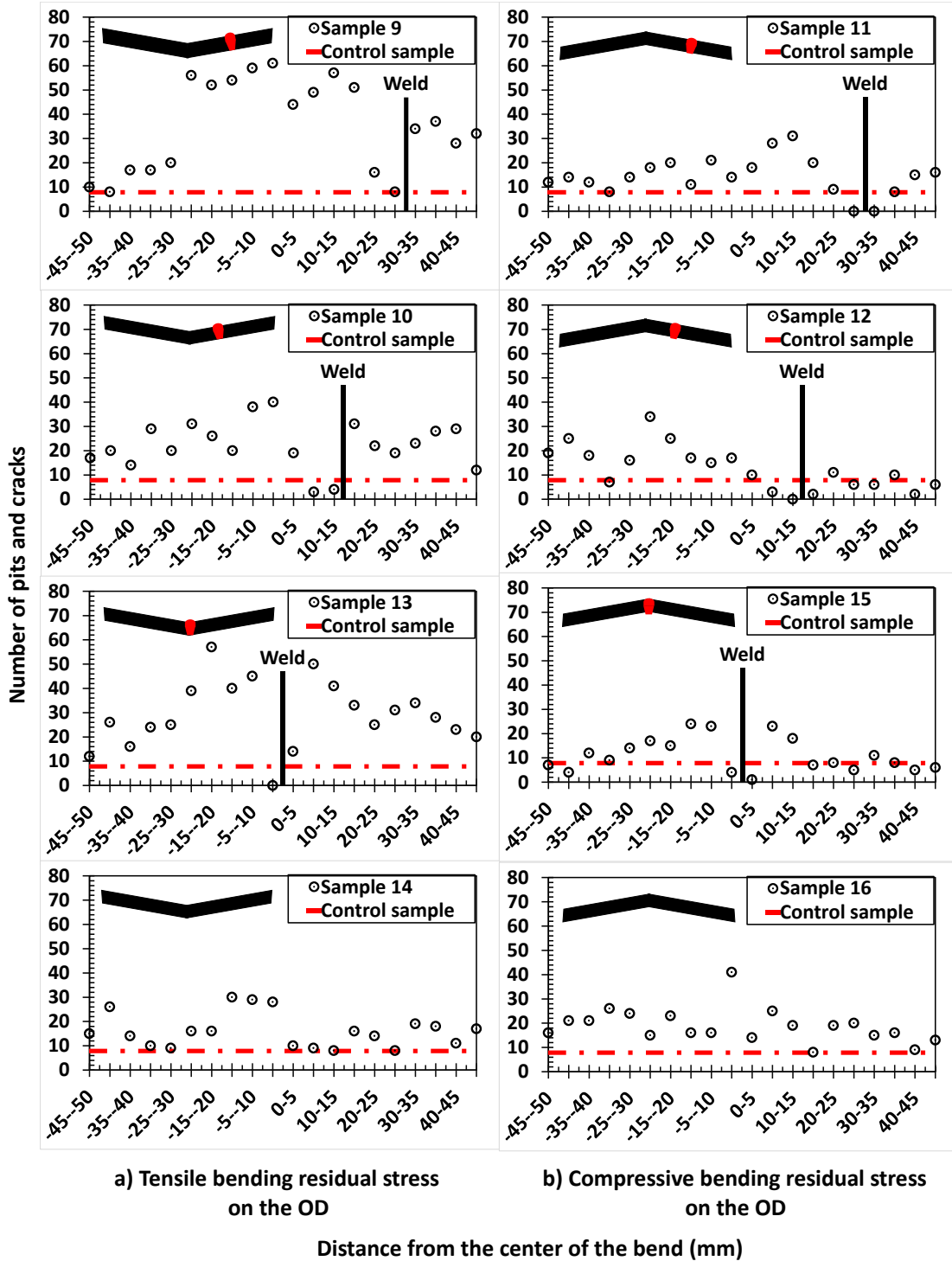


Figure 5.1 Distribution of pits and cracks over the length of samples corroded for 150 days

with (a) tensile bending residual stress on the OD and b) compressive bending residual stress on the OD.

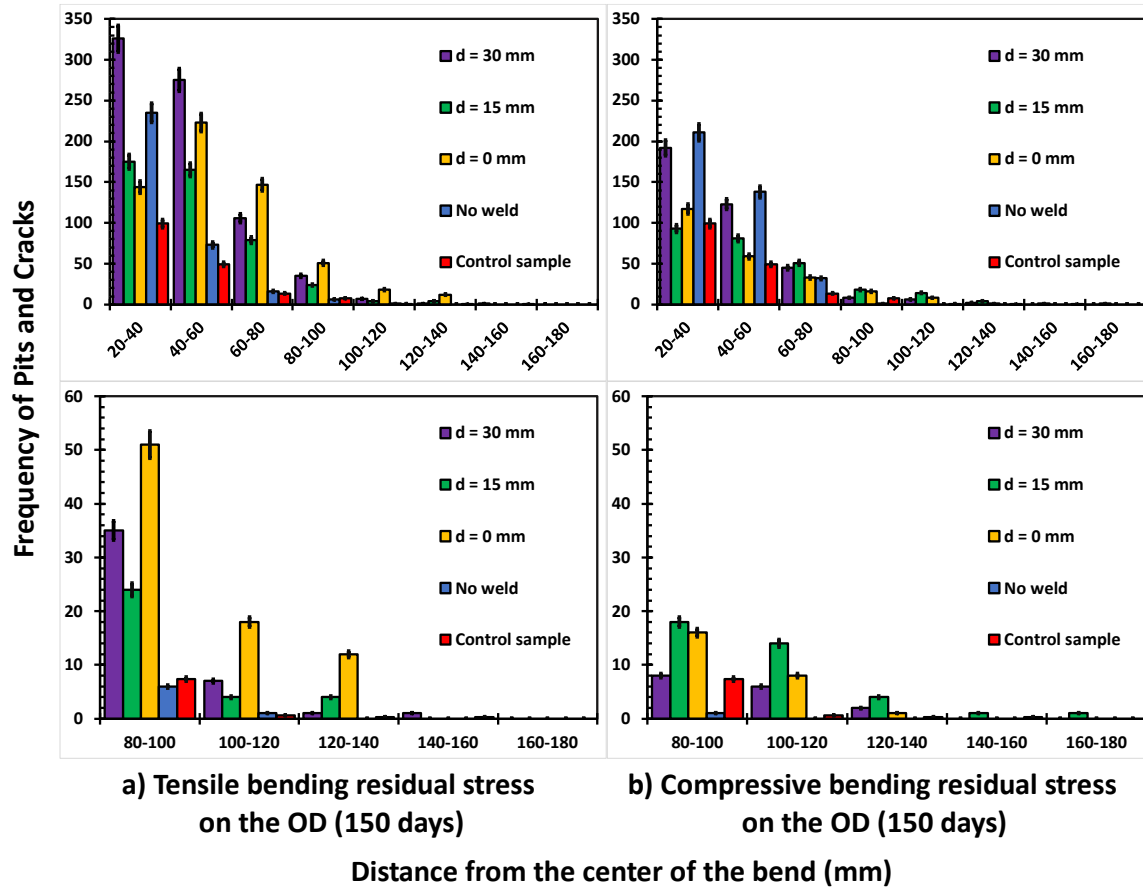


Figure 5.2 Frequencies of pits and cracks in different depths on the samples corroded for 150 days with a) tensile bending residual stress on the OD and b) compressive bending residual stress on the OD.

Because of the significant effect of mill scale on the pits and cracks morphologies on the samples corroded for 90 days (samples 1 to 8), only the samples corroded for 150 days (samples 9 to 16) were selected for the discussion. The details of the effect of the mill scale on the samples corroded for 90 days are discussed in the later section.

As shown in Figure 5.1 a) and b), a significant increase in the number of defects from control samples to those corroded for 150 days is observed. Corresponding to this observation, the increase in the frequency of defects from control and corroded samples is also observed, particularly at $> 60 \mu\text{m}$. These results indicate that the corrosion in the NNpH environment increased the number and depth of defects, regardless of the bend angles and the distance between the center of the bend and the weld centerline. However, the samples with no weld, samples 14 & 16, exhibit comparable results to those of control samples. This indicates that the welding residual axial stress was critical in anodic dissolution, crack initiation, and Stage I crack growth in the NNpH environment.

Furthermore, in addition to welding residual stress, the initial thickness of the mill scale could have contributed to the difference in the morphologies of defects in the samples with a girth weld and those without the weld. As mentioned in Chapter 4, the mill scale layer observed on the surfaces of the samples with no girth weld was significantly thinner than those with the girth weld. Naturally, the thinner the mill scale layer is, the more difficult it is to flake. As such, it is possible that the non-flaked mill scale layer protected the surface of the samples as intended, leading to the results mentioned above.

Comparison between Figure 5.1 a) to b) shows that the peak values are observed at $5 \text{ mm} < |x| < 20 \text{ mm}$, illustrating the effective range of bending residual stress. It is also seen that the distributions around the WCL tend to be lower than those in the other areas. As explained in Chapter 4, the weld metal and toes were covered with a thick oxide layer that remained even after 150 days. As such, these observations likely resulted from the oxide layer protecting the metal surfaces from NNpH corrosion. Another possibility is the

residual stress around the weld metal, which may be acting as an additional factor. As mentioned in section 2.3, welding axial residual stress near the weld metal on the OD is generally compressive. Although the stress relaxation after sectioning changes residual stress distribution, the significance of this effect on those samples is unknown. If the residual stress around the weld metal remains compressive after sectioning, the possibility of crack initiation is unlikely.

The distributions of pits and cracks in the samples with compressive bending residual stress on the OD with varying d (distance between the center of the bend and the WCL) are illustrated in Figure 5.1 b). As can be seen, the samples with compressive bending residual stress on the OD also show peaks at $5 \text{ mm} < |x| < 25 \text{ mm}$. This is because of the formation of galvanic cells between the area with compressive residual stress on the OD and surrounding area. The difference in the distribution between the samples with compressive bending residual stress on the OD is not as significant as that observed in the samples with tensile bending residual stress on the OD. However, the notable difference between the sample with no girth weld and those with the girth weld is still observable. This effect could be attributed to the electrochemical potential difference between weld metal and base metal because of the difference in composition and microstructure, as explained in section 2.4. However, as shown in Figure 5.1 a), the correlation between the number of pits and cracks and the distance from WCL is not observed. Furthermore, as shown in section 4.2.6 and 4.2.8, the surface of samples 14 ($d = \text{N/A}$) and 16 were mostly covered by the mill scale, preventing corrosion in the NNpH environment. As such, the effect of galvanic cells

between weld metal and base metal is insignificant. However, exploring the significance of this effect on different samples may be recommended for future work.

Comparisons regarding the frequencies of pits and cracks with different depths were conducted and are visible in Figure 5.2. Comparing the samples with tensile bending residual stress on the OD shows that the highest frequencies of pits and cracks $> 80 \mu\text{m}$ are observed in sample 13 ($d = 0 \text{ mm}$), followed by samples 9 ($d = 30 \text{ mm}$), 10 ($d = 15 \text{ mm}$), and 14 ($d = \text{N/A}$). It is also observed that the frequencies in sample 14 are overall lower than the samples with the girth weld, which is discussed in the later section. The same comparisons above were conducted on the samples with compressive bending residual stress on the OD. The highest frequencies of pits and cracks deeper than $80 \mu\text{m}$ are exhibited by sample 12 ($d = 15 \text{ mm}$), followed by sample 15 ($d = 0 \text{ mm}$).

Based on the comparisons in terms of both distributions and frequencies of pits and cracks, it can be estimated that the samples with $d = 30 \text{ mm}$ have the highest frequencies of $< 80 \mu\text{m}$ pits and cracks, regardless of the type of bending residual stress on the OD. This result is consistent with the numerous shallow pits and cracks observed around the center of the bend in samples 9 and 11. However, these results disagree with those of the other samples; a low number of pits and cracks are observed around the area 30 mm away from WCL. These results imply that external factors such as mill scale might have enhanced galvanic corrosion, resulting in the vast colonies of localized corrosion sites.

On the other hand, $> 80 \mu\text{m}$ pits and cracks were frequently observed in the samples with $d = 0 \text{ mm}$ and 15 mm . These observations are also evidenced by the cross-sectional surface morphologies of corresponding samples mentioned in section 4.2, as apparent crack-like

features were seen around the center of the bend of those samples. These observations and the distributions show that the stress corrosion cell was formed at $5 \text{ mm} < |x| < 20 \text{ mm}$ and that the significance of this cell changes with d . Based on the frequencies of deep pits and cracks, it is summarized that the significance of initiation and stage I growth of C-NNpHSCC changes with d in order of $d = 0 \text{ mm}$, $d = 15 \text{ mm}$, and $d = 30 \text{ mm}$, from the highest to the lowest. This indicates that the welding residual stress distribution in depth favourable to crack initiation and Stage I growth is observed near the girth weld and diminishes with an increase in the distance between the center of the bend and the weld centerline. However, it is possible that the higher bending stress applied on the samples with $d = 0 \text{ mm}$ than the others contributed to these morphologies, which are discussed in the next section.

Based on the distribution of pits and cracks observed over the length of the samples, a rough plot of axial residual stress from WCL was plotted and is shown in Figure 5.3.

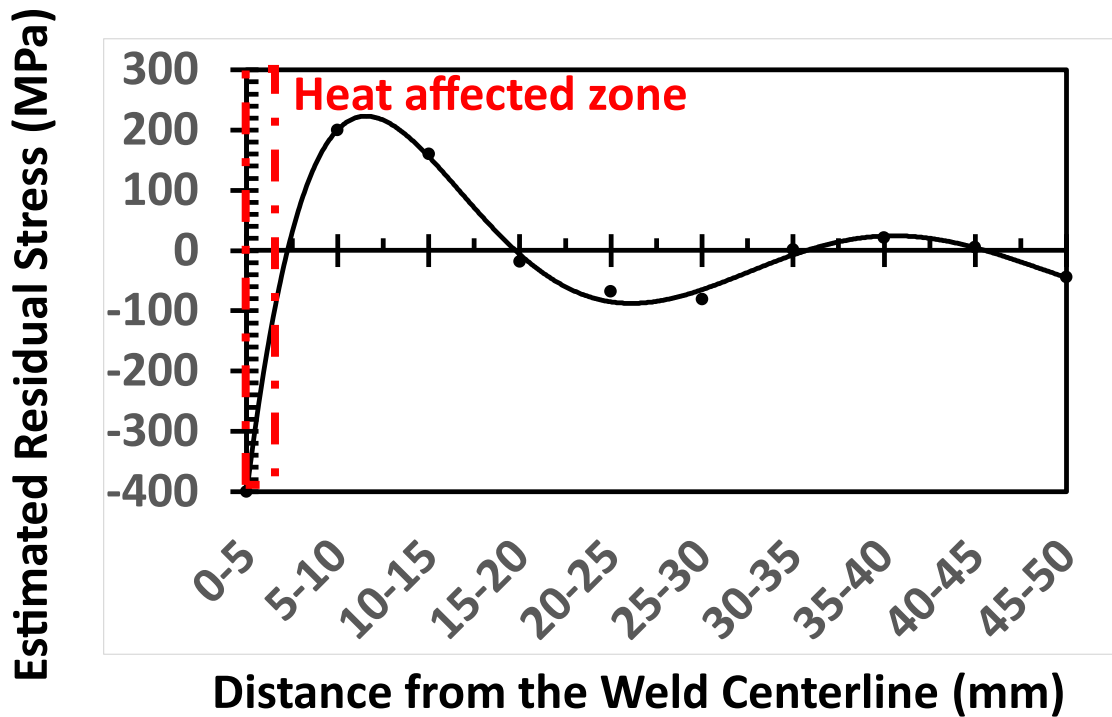


Figure 5.3 Estimated axial residual stress from WCL on the outer surface of the corroded samples.

Studies show that the maximum axial compressive stress induced by the girth weld on the OD ranges from -600 to -400 MPa, whereas the maximum tensile axial stress on the OD is around 200 MPa[31]–[34]. As such, these values are selected as boundary conditions for estimating axial residual stress. As can be seen in Figure 5.3, axial residual stress at the weld toe is compressive, which is consistent with previous research [31]–[34]. Tensile residual stress peaks at $x = 10$ mm and diminishes until $x = 25$ mm. Although the distribution of the axial tensile stress zone does not correspond to that in whole pipes, the shift of the tensile zone toward the weld toe is analogous to residual stress redistribution because of sectioning observed by Hempel *et al.* [31]. This indicates that, as expected, the

stress relief because of sectioning changed the residual stress distribution. It must be kept in mind that the significance of initiation and Stage I growth of C-NNpHSCC is not necessarily proportional to the magnitude of tensile residual stress on the OD, as explained in section 2.3. According to Chen *et al.*, the area with moderate residual stress on the OD (~150 MPa) exhibits the highest number of cracks in the NNpH environment [22]. Based on the estimated residual stress in Figure 5.3, such areas may be observed at $5 \text{ mm} < x < 10 \text{ mm}$ and $15 \text{ mm} < x < 20 \text{ mm}$, in the range of bending residual stress applied on samples 13 and 15 that exhibit the highest frequencies of deep pits and cracks.

5.2 Effect of Bending Residual Stress on Pits & Cracks Morphologies and Distributions

The previous section explained the change in the statistical number of pits and cracks and the surface morphologies of corroded samples with varying d . However, the interaction between bending and welding residual stress must also be discussed. As such, each pair of samples with the same d but different bend angles were compared to investigate the effect of the combination of bending and welding residual stresses.

As shown in Figure 5.1, the samples with tensile bending residual stress on the OD exhibit higher distributions of defects than those with compressive bending residual stress, aside from the pair with $d = N/A$. It is also shown that the significant differences in the distributions are observed at $5 \text{ mm} < |x| < 10 \text{ mm}$, and the distributions somewhat converge at $|x| = 45 \text{ mm}$. These observations also indicate that the peak bending residual stress is observed at $5 \text{ mm} < |x| < 10 \text{ mm}$ and diminishes with an increase in $|x|$. On the other hand, the pair of samples with $d = N/A$ shows identical distributions. The frequencies of pits and cracks on the samples with tensile bending residual stress on the OD are also higher than

those with compressive bending residual stress, as visible in Figure 5.2. This indicates that the interaction between tensile bending residual stress and welding residual stress generally increased the number of pits and cracks. However, sample 12 shows higher frequencies of pits and cracks deeper than 100 μm compared to sample 10. The surface morphologies of samples 10 and 12 discussed in Chapter 4 show that both samples exhibited partial exfoliation of the mill scale layer with several crevice corrosion sites. It is possible that the exposure of pre-existing deep pits in sample 12 served as outliers and caused this discrepancy.

The distribution of pits and cracks deeper than 80 μm on each sample is plotted and visible in Figure 5.4 a) and b).

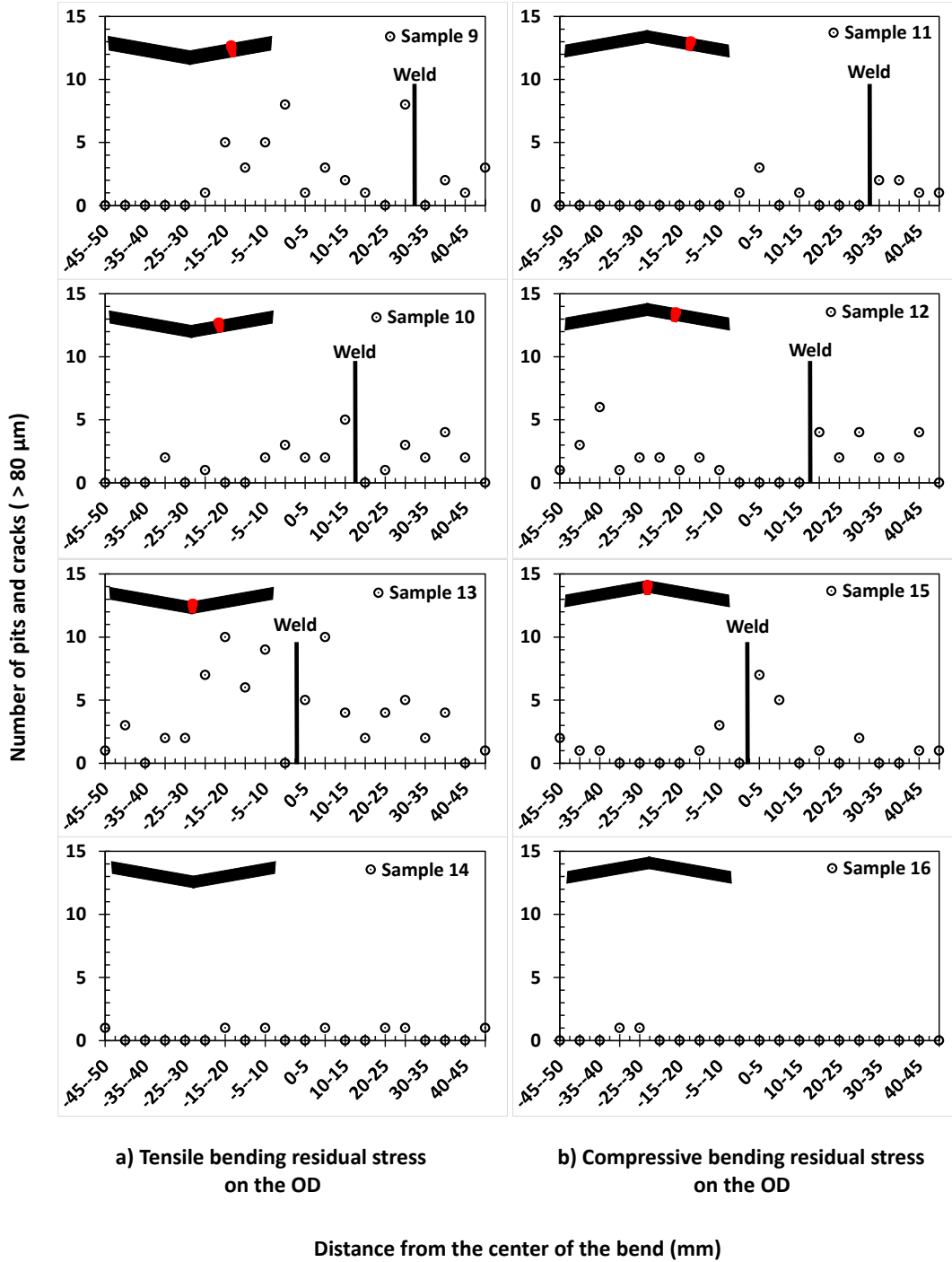


Figure 5.4 Distribution of pits and cracks deeper than 80 μm over the length of samples

corroded for 150 days with (a tensile bending residual stress and b) compressive bending residual stress on the OD.

As shown in Figure 5.4 a), the highest number of deep defects in the samples with tensile bending residual stress on the OD is mostly observable at $5 \text{ mm} < |x| < 20 \text{ mm}$. This somewhat agrees with the estimated range of bending residual stress mentioned above.

While this tendency is also observed in the samples with compressive bending residual stress on the OD, as shown in Figure 5.4 b), the difference in the number compared to those with tensile bending residual stress on the OD is mostly significant. It must also be noted that the overall number of deep defects are generally higher in the samples in Figure 5.4 a) than those in Figure 5.4 b), aside from sample 10 and 12 ($d = 15 \text{ mm}$). Since the discrepancy between samples 10 and 12 is observed at $|x| > 35 \text{ mm}$, it is possible that the aforementioned outlier is the cause of this observation.

Based on the observations mentioned above, it is evident that the addition of bending residual stress on the samples significantly affected the morphologies of localized corrosion sites, particularly on samples 13 (tensile residual bending stress on the OD, $d = 0 \text{ mm}$, 150 days) and 15 (compressive residual bending stress on the OD). This result simply indicates that tensile bending residual stress contributed to faster crack initiation and Stage I growth in the NNpH environment than compressive bending residual stress, even though both stresses form galvanic cell and enhances anodic dissolution. As explained in section 2.3, surface tensile residual stress and tensile stress gradient in depth largely contribute to crack growth. As such, it can be estimated that the deep defects observed near the center of the bend of the corroded samples, such as those shown in Figure 4.17 c) to e), are the result of

crack initiation, crack growth, and crack tip coarsening with the support of welding and bending tensile residual stresses.

As for the higher number of deep defects observed in samples 13 and 15, this result could be because of the enhanced galvanic effect near the girth weld and residual stress gradient in depth. Since the specimens with $d = 0$ mm have a girth weld at the center of the bend, the actual bending residual stress could have been applied to the end of the girth weld and the area adjacent to the weld toes because of the high resistance to bending at the girth weld. Furthermore, this high resistance might have increased the load required to bend the specimens at desired angles, thereby increasing the magnitude of residual stress after springback. Additionally, the effective range of bending residual stress on the corroded samples with $d = 0$ mm includes HAZ, which is generally susceptible to corrosion. This might have further enhanced galvanic corrosion and crack initiation in the area mentioned above. However, the significance of this effect is unknown. It must also be noted that because of the presence of the girth weld, both samples 13 and 15 exhibited a more rounded curve than the other samples, which indicates that the results may not be comparable. The contribution of mill scale must also not be ignored. As shown in Chapter 4, the samples with outward bending exhibited almost full removal of the mill scale layer around the center of the bend, whereas the remaining mill scale was observed near the center of the bend of inwardly bent samples. Furthermore, as shown in Figure 5.4, the changes in the number of deep defects with different bend angles are most apparent at $|x| > 15$ mm, where exfoliation of the mill scale was frequently observed. These observations indicate that the remaining mill scale on inwardly bent samples also took part in the growth of deep defects,

likely as cathodes that formed galvanic cells with surface metal and accelerated the cycle of crack initiation to crack tip coarsening.

The other samples with the girth weld showed a difference in distribution and frequencies of pits and cracks, depending on the bending residual stress added to the OD. However, since many deep pits and cracks were found on samples 13 and 15, it can be concluded that the addition of bending residual stress on the OD at WCL increases the number of deep defects that are detrimental to the life of the pipe.

Since the addition of tensile bending residual stress on the OD yielded an overall higher number of pits and cracks, as well as higher frequencies of pits and cracks deeper than 80 μm than those with compressive bending residual stress on the OD, the total residual stress can be considered as the simple sum of bending residual stress and welding residual stress. However, it is possible that localized stress relaxation occurred because of the lack of data required to conclude that the contribution of stress relaxation to the surface morphologies of the corroded sample is unknown.

5.3 Effect of Static Corrosion Durations on Pits & Cracks Morphologies and Distributions

As explained in Chapter 4, the comparisons between the pairs of samples 1 (tensile bending residual stress on the OD, $d = 30$ mm for 90 days) and sample 9 (150 days), and samples 2 ($d = 15$ mm for 90 days) and sample 10 (150 days) show that samples 1 and 2 exhibit a significantly lower number of pits and cracks than in sample 9 and 10. Furthermore, the cross-sectional surfaces of samples 1 and 2 were covered with a thick mill scale layer with little to no evidence of crevice corrosion, evidenced by the frequencies of defects comparable to those of control samples. In contrast, the dissolution of the mill scale was

apparent in both samples 9 and 10. The pairs of Samples 3 (compressive bending residual stress on the OD, $d = 30$ mm for 90 days) and 11 (150 days), and sample 8 (compressive bending residual stress on the OD, $d = \text{N/A}$ for 90 days) and 16 (150 days) show similar trends to the abovementioned samples. However, exfoliation of the mill scale layer from the surface was confirmed in both samples. Furthermore, the difference in the distribution and frequency of pits and cracks is not as significant as the pair of samples 1 and 2.

A comparison between sample 4 (compressive bending residual stress on the OD, $d = 15$ mm for 90 days) and sample 12 (150 days) shows a significantly higher number of pits and cracks no deeper than $20 \mu\text{m}$ in sample 4 than in sample 12. Indeed, the colonies of shallow pits were more frequently observed in samples 4 and 5 than in samples 12 and 13, as mentioned in Chapter 4. The crack coalescence may account for these observations because of the faster crack growth in the length directions. The same tendencies are visible in that pair of samples 5 (tensile bending residual stress on the OD, $d = 0$ mm for 90 days) and 13 (150 days), and sample 7 (compressive bending residual stress on the OD, $d = 0$ mm for 90 days) and sample 15 (150 days). Partial or complete removal of the mill scale layer was observed in all of the samples mentioned above. Overall, the surface morphologies and distribution of pits and cracks observed in these pairs of samples agree with the typical mechanisms of initiation and Stage I growth of NNpHSCC.

On the other hand, the comparison between sample 6 (tensile bending residual stress on the OD, $d = \text{N/A}$ for 90 days) and sample 14 (150 days) shows that sample 6 exhibits an overall higher number of pits and cracks at any depth than in sample 14, despite its shorter durations in NNpH environment. The surface morphologies show more frequent mill scale

exfoliations and crevice corrosion sites in samples 6 than in sample 14, particularly around the center of the bend. These observations are precisely opposite to those seen in samples 1 and 9. Based on the observation of the samples, it is evident that the frequencies of defects are closely tied to the morphologies of the mill scale layer. As described in section 2.2.3, the mill scale may act as a barrier that prevents the surface metal from exposure to a corrosive environment or as a cathode that forms a galvanic cell between the anodic surface metal. Naturally, welding and bending residual stresses do not have a significant role in the initiation and Stage I growth of NNpHSCC so long as the reaction between the surface metal and NNpH solution does not occur. Since 5 out of 8 pairs of the samples with different durations show deviated results from the expected results, such as those shown in samples 5 and 13, it can be concluded that the morphologies of pits and cracks on the samples corroded for 90 days were significantly affected by the initial condition and morphologies of mill scale compared to those corroded for 150 days. This suggests that the observation of change in morphologies of defects and mill scale may require a longer duration than 90 days.

Chapter 6 : Conclusions

This research aimed to determine the effects of welding residual stress, bending residual stress, and mill scale on initiation and Stage I growth of near-neutral pH circumferential stress corrosion cracking (C-NNpHSCC). In total, 16 corroded samples and three control samples were characterized by the destructive method. The conclusions of this study are as follows:

- 1) Deep cracks ($> 80 \mu\text{m}$) were observed where welding and bending residual stresses were present in all cases. The results indicate that both factors significantly influence the initiation and Stage I growth of C-NNpHSCC, leading to the earlier transition to Stage II growth.
- 2) The addition of tensile bending residual stress on the OD surface of the pipeline increases the number and depth of corrosion pits and cracks compared to the samples with compressive bending residual stress on the OD. This is likely because of the contribution of tensile residual stress gradient on the crack growth cycle and partial exfoliation of the mill scale layer that formed a severely corrosive environment.
- 3) From the frequencies of pits and cracks deeper than $80 \mu\text{m}$, the most optimized combination of bending residual stress and welding residual stress was observed at $d = 0 \text{ mm}$, followed by $d = 15 \text{ mm}$ and 30 mm . The high susceptibility of the samples with $d = 0 \text{ mm}$ to C-NNpHSCC may be because of the residual stress from welding and high resistance to bending at the girth weld. This, in turn, leads to a

higher bending stress required to achieve the desired bend angle, resulting in an increase in bending residual stress that shifts toward HAZ. This contributes to the rapid initiation and Stage I growth of C-NNpHSCC.

- 4) The morphology of pits and cracks on samples corroded for 90 days was significantly affected by the initial condition and morphology of the mill scale compared to those corroded for 150 days. Longer durations may be required to observe changes in morphologies.

6.1 Recommendations for Future Work

- 1) This research investigates the effect of weld residual stress on the initiation and Stage I growth of C-NNpHSCC. However, the results have been heavily influenced by the initial condition of samples, specifically pre-existing pits covered with thick layers of mill scale. Although these factors have a significant role in C-NNpHSCC in the field, the effect of residual stress might have been undermined. As such, the removal of the mill scale from the surface before the experiments is recommended solely for the future investigation of the correlation between residual stress and C-NNpHSCC.
- 2) The samples used in this research were cut off a pipe with a girth weld. However, it has been reported that the growth of C-NNpHSCC adjacent to a spiral weld was also confirmed. Although the residual stress distribution induced by spiral weld is more complicated than that by girth weld, investigation of the effect of spiral weld should be considered for future experiments. Applying static or cyclic loading to the

samples in the C2 solution is also recommended as stress relaxation because external stresses must be considered.

- 3) As described in the previous section, the duration of the static corrosion test is recommended to be longer than 90 days. Since the samples corroded for 150 days show the significant dissolution of mill scale, a comparison between the samples corroded for 150 days and those corroded for a longer duration may be ideal.
- 4) As mentioned in section 5.1, it is possible that the galvanic couple formed between the weld metal and base metal may affect the morphologies of pits and cracks in the NNpH environment. As such, a detailed investigation of this effect, such as by measuring the corrosion potential during the static corrosion test, is highly recommended.
- 5) The criteria for counting corrosion pits and cracks formed in the NNpH environment shown in section 4.1 is imperfect. For more accurate differentiation of the aforementioned defects from pre-existing defects on the pipeline surface, further documentation on the characteristics of those defects is recommended.

Bibliography

- [1] B. James and A. Hudgins, "Failure analysis of oil and gas transmission pipelines," in *Handbook of Materials Failure Analysis with Case Studies from the Oil and Gas Industry*, Elsevier, 2015, pp. 1–38. doi: 10.1016/B978-0-08-100117-2.00001-7.
- [2] J. Beavers and T. A. Bubenik, "Stress corrosion cracking," in *Trends in Oil and Gas Corrosion Research and Technologies: Production and Transmission*, Elsevier Inc., 2017, pp. 295–314. doi: 10.1016/B978-0-08-101105-8.00012-7.
- [3] Canada. National Energy Board., *Public inquiry concerning stress corrosion cracking on Canadian oil and gas pipelines : report of the inquiry*. National Energy Board, 1996.
- [4] W. Chen, "An Overview of Near-Neutral pH Stress Corrosion Cracking in Pipelines and Mitigation Strategies for Its Initiation and Growth," *Corrosion*, vol. 72, no. 7, pp. 962–977, Jul. 2016, doi: 10.5006/1967.
- [5] B. Fang *et al.*, "THE INFLUENCE OF WELD HEAT-AFFECTED ZONE ON STRESS CORROSION CRACKING OF PIPELINE STEEL IN NEAR-NEUTRAL PH ENVIRONMENT." [Online]. Available: <http://onepetro.org/NACECORR/proceedings-pdf/CORR08/All-CORR08/NACE-08500/1806536/nace-08500.pdf/1>
- [6] B. Lu, J. L. Luo, and D. G. Ivey, "Near-neutral pH stress corrosion cracking susceptibility of plastically prestrained X70 steel weldment," *Metall Mater Trans A Phys Metall Mater Sci*, vol. 41, no. 10, pp. 2538–2547, Oct. 2010, doi: 10.1007/s11661-010-0283-6.
- [7] G. Van Boven, W. Chen, and R. Rogge, "The role of residual stress in neutral pH stress corrosion cracking of pipeline steels. Part I: Pitting and cracking occurrence," *Acta Mater*, vol. 55, no. 1, pp. 29–42, Jan. 2007, doi: 10.1016/j.actamat.2006.08.037.
- [8] Z. Shirband, "Understanding the Effects of Hydrogen, Hydrostatic testing and Mill-scale on SCC of Pipelines in Near-Neutral pH Environments."
- [9] S. Wang, L. Lamborn, K. Chevil, E. Gamboa, and W. Chen, "Near-neutral pH corrosion of mill-scaled X-65 pipeline steel with paint primer," *J Mater Sci Technol*, vol. 49, pp. 166–178, Jul. 2020, doi: 10.1016/j.jmst.2020.01.016.
- [10] "Stress Corrosion Cracking," 2007. [Online]. Available: www.cepa.com
- [11] "CEPA Recommended Practices for Managing Near-neutral pH Stress Corrosion Cracking 3rd edition MAY 2015 PREPARED BY: CEPA PIPELINE INTEGRITY WORKING GROUP NOTICE OF COPYRIGHT," 2015.
- [12] M. Baker Jr, "TTO Number 8 Integrity Management Program Delivery Order DTRS56-02-D-70036 Stress Corrosion Cracking Study FINAL REPORT OPS TTO8-Stress Corrosion Cracking Study."

- [13] W. Chen, R. L. Eadie, and R. L. Sutherby, "Environmental effects on near-neutral pH stress corrosion cracking in pipelines."
- [14] F. Song, "Overall Mechanisms of High pH and Near-Neutral pH SCC, Models for Forecasting SCC Susceptible Locations, and Simple Algorithms for Predicting High pH SCC Crack Growth Rates." [Online]. Available: <http://onepetro.org/NACECORR/proceedings-pdf/CORR08/All-CORR08/NACE-08129/1805709/nace-08129.pdf/1>
- [15] A. Eslami, W. Chen, R. Worthingham, R. Kania, and J. Been, "Effect of CO₂ on Near-Neutral pH Stress Corrosion Cracking Initiation of Pipeline Steel." [Online]. Available: <http://onepetro.org/NACECORR/proceedings-pdf/CORR10/All-CORR10/1718239/nace-10300.pdf>
- [16] J. J. Knechtel, "FULL-SCALE INVESTIGATION OF CRACK GROWTH BEHAVIOUR UNDER VARIABLE PRESSURE FLUCTUATIONS IN NEAR-NEUTRAL PH ENVIRONMENTS."
- [17] R. R. Fessler, "CHARACTERISTICS, CAUSES, AND MANAGEMENT OF CIRCUMFERENTIAL STRESS-CORROSION CRACKING," 2014. [Online]. Available: <http://asmedigitalcollection.asme.org/IPC/proceedings-pdf/IPC2014/46117/V002T06A066/2509367/v002t06a066-ipc2014-33059.pdf>
- [18] D. Bayliss and D. Deacon, *Steelwork Corrosion Control*. 2002. doi: 10.4324/noe0415261012.
- [19] M. C. Bagatini, V. Zymła, E. Osório, A. Cezar, and F. Vilela, "Characterization and Reduction Behavior of Mill Scale," 2011.
- [20] "External Corrosion of Oil and Natural Gas Pipelines," in *Corrosion: Environments and Industries*, ASM International, 2018, pp. 1015–1025. doi: 10.31399/asm.hb.v13c.a0004213.
- [21] L. Bai, K. Jiang, and L. Gao, "The influence and mechanism of residual stress on the corrosion behavior of welded structures," *Materials Research*, vol. 21, no. 5, 2018, doi: 10.1590/1980-5373-MR-2018-01660.
- [22] W. Chen, G. Van Boven, and R. Rogge, "The role of residual stress in neutral pH stress corrosion cracking of pipeline steels - Part II: Crack dormancy," *Acta Mater*, vol. 55, no. 1, pp. 43–53, Jan. 2007, doi: 10.1016/j.actamat.2006.07.021.
- [23] P. Prevéy and D. Hornbach, "Residual Stress in Pipelines," in *Oil and Gas Pipelines: Integrity and Safety Handbook*, Wiley, 2015, pp. 73–98. doi: 10.1002/9781119019213.ch07.
- [24] R. Eadie *et al.*, "IPC02-27118 LONG SEAM WELDS IN GAS AND LIQUIDS PIPELINES AND NEAR-NEUTRAL PH STRESS CORROSION CRACKING AND CORROSION FATIGUE." [Online]. Available: http://asmedigitalcollection.asme.org/IPC/proceedings-pdf/IPC2002/36207/1629/4549684/1629_1.pdf
- [25] W. Zang, J. Gunnars, P. Dong, and J. K. Hong, "Improvement and Validation of Weld Residual Stress Modelling Procedure 2009:15 Title: Improvement and Validation of Weld

Residual Stress Modelling Procedure,” 2009, [Online]. Available:
www.stralsakerhetsmyndigheten.se

- [26] P. Dong, “Length scale of secondary stresses in fracture and fatigue,” *International Journal of Pressure Vessels and Piping*, vol. 85, no. 3, pp. 128–143, Mar. 2008, doi: 10.1016/j.ijpvp.2007.10.005.
- [27] J. H. P Dong, “ON THE RESIDUAL STRESS PROFILES IN NEW API 579/ASME FFS-1 APPENDIX E,” *Welding in the World*, vol. 51, pp. 119–127, 2007.
- [28] P. Dong, S. Song, and X. Pei, “An IIW residual stress profile estimation scheme for girth welds in pressure vessel and piping components,” *Welding in the World*, vol. 60, no. 2, pp. 283–298, Feb. 2016, doi: 10.1007/s40194-015-0286-4.
- [29] P. Dong, S. Song, and J. Zhang, “ASSESSMENT OF RESIDUAL STRESS PROFILES FOR FITNESS FOR SERVICE ASSESSMENT OF PIPE GIRTH WELDS,” 2014. [Online]. Available: <http://asmedigitalcollection.asme.org/PVP/proceedings-pdf/PVP2014/46049/V06BT06A057/4437540/v06bt06a057-pvp2014-28217.pdf>
- [30] S. Song, P. Dong, and J. Zhang, “A full-field residual stress profile estimation scheme for pipe girth welds,” in *American Society of Mechanical Engineers, Pressure Vessels and Piping Division (Publication) PVP*, 2012, pp. 109–120. doi: 10.1115/PVP2012-78560.
- [31] N. Hempel, T. Nitschke-Pagel, and K. Dilger, “Study on the near-surface residual stress state in butt-welded pipes of austenitic steel using X-ray diffraction,” *Welding in the World*, vol. 60, no. 6, pp. 1169–1179, Nov. 2016, doi: 10.1007/s40194-016-0378-9.
- [32] M. Sabokrouh and M. Farahani, “Experimental Study of the Residual Stresses in Girth Weld of Natural Gas Transmission Pipeline,” *Applied and Computational Mechanics*, vol. 5, pp. 199–206, 2019, [Online]. Available: <https://api.semanticscholar.org/CorpusID:106395054>
- [33] M. Perić, I. Garašić, N. Gubelj, Z. Tonković, S. Nižetić, and K. Osman, “Numerical Simulation and Experimental Measurement of Residual Stresses in a Thick-Walled Buried-Arc Welded Pipe Structure,” *Metals (Basel)*, vol. 12, no. 7, 2022, doi: 10.3390/met12071102.
- [34] T. Neeraj, T. Gnäupel-Herold, H. J. Prask, and R. Ayer, “Residual stresses in girth welds of carbon steel pipes: Neutron diffraction analysis,” *Science and Technology of Welding and Joining*, vol. 16, no. 3, pp. 249–253, Apr. 2011, doi: 10.1179/1362171810Y.0000000028.
- [35] N. Hempel, J. R. Bunn, T. Nitschke-Pagel, E. A. Payzant, and K. Dilger, “Study on the residual stress relaxation in girth-welded steel pipes under bending load using diffraction methods,” *Materials Science and Engineering: A*, vol. 688, pp. 289–300, Mar. 2017, doi: 10.1016/j.msea.2017.02.005.

- [36] J. A. Beavers, J. T. Johnson, and R. L. Sutherby, "MATERIALS FACTORS INFLUENCING THE INITIATION OF NEAR-NEUTRAL pH SCC ON UNDERGROUND PIPELINES," 2000. [Online]. Available: <http://offshoremechanics.asmedigitalcollection.asme.org/IPC/proceedings-pdf/IPC2000/40252/V002T06A041/2507801/v002t06a041-ipc2000-221.pdf>
- [37] *CSA Z662:23, Oil and gas pipeline systems.*
- [38] H. Shirazi, R. Eadie, and W. Chen, "A review on current understanding of pipeline circumferential stress corrosion cracking in near-neutral PH environment," *Engineering Failure Analysis*, vol. 148. Elsevier Ltd, Jun. 01, 2023. doi: 10.1016/j.engfailanal.2023.107215.
- [39] D. Abdulhameed, S. Adeeb, and R. Cheng, "THE INFLUENCE OF THE BOURDON EFFECT ON PIPE ELBOW." [Online]. Available: <http://asmedigitalcollection.asme.org/IPC/proceedings-pdf/IPC2016/50275/V003T05A037/2510617/v003t05a037-ipc2016-64659.pdf>
- [40] T. Kushida *et al.*, "EFFECTS OF METALLURGICAL FACTORS AND TEST CONDITIONS ON NEAR NEUTRAL pH SCC OF PIPELINE STEELS." [Online]. Available: <http://onepetro.org/NACECORR/proceedings-pdf/CORR01/All-CORR01/1891563/nace-01213.pdf>
- [41] R. Chu, W. Chen, S.-H. Wang, F. King, T. R. Jack, and R. R. Fessler, "Microstructure Dependence of Stress Corrosion Cracking Initiation in X-65 Pipeline Steel Exposed to a Near-Neutral pH Soil Environment," 2004.
- [42] Z. Y. Liu, X. G. Li, C. W. Du, L. Lu, Y. R. Zhang, and Y. F. Cheng, "Effect of inclusions on initiation of stress corrosion cracks in X70 pipeline steel in an acidic soil environment," *Corros Sci*, vol. 51, no. 4, pp. 895–900, Apr. 2009, doi: 10.1016/j.corsci.2009.01.007.
- [43] J. Zhao *et al.*, "Crack Growth Modeling and Life Prediction of Pipeline Steels Exposed to Near-Neutral pH Environments: Dissolution Crack Growth and Occurrence of Crack Dormancy in Stage I," *Metall Mater Trans A Phys Metall Mater Sci*, vol. 48, no. 4, pp. 1629–1640, Apr. 2017, doi: 10.1007/s11661-016-3951-3.
- [44] "2 Fundamentals of Stress Corrosion Cracking 2.1 DEFINITION OF STRESS CORROSION CRACKING," 2013.
- [45] "Integrity of Pipelines Transporting Hydrocarbons." [Online]. Available: <http://www.nato.int/science>
- [46] W. Chen, R. Kania, R. Worthingham, and G. Van Boven, "Transgranular crack growth in the pipeline steels exposed to near-neutral pH soil aqueous solutions: The role of hydrogen," *Acta Mater*, vol. 57, no. 20, pp. 6200–6214, Dec. 2009, doi: 10.1016/j.actamat.2009.08.047.

- [47] A. Egbewande *et al.*, "Transgranular crack growth in the pipeline steels exposed to near-neutral pH soil aqueous solutions: Discontinuous crack growth mechanism," *Corros Sci*, vol. 83, pp. 343–354, 2014, doi: 10.1016/j.corsci.2014.02.032.
- [48] W. Chen and R. L. Sutherby, "Crack growth behavior of pipeline steel in near-neutral pH soil environments," *Metall Mater Trans A Phys Metall Mater Sci*, vol. 38, no. 6, pp. 1260–1268, Jun. 2007, doi: 10.1007/s11661-007-9184-8.
- [49] M. Yu, W. Chen, R. Kania, G. Van Boven, and J. Been, "Depressurization-Induced Crack Growth Enhancement for Pipeline Steels Exposed to Near-Neutral pH Environments," 2014. [Online]. Available: <http://asmedigitalcollection.asme.org/IPC/proceedings-pdf/IPC2014/46117/V002T06A076/2509405/v002t06a076-ipc2014-33282.pdf>
- [50] C. Zhang, M. Ran, Y. Wang, and W. Zheng, "Microstructural Effects in the Development of Near-Neutral pH Stress Corrosion Cracks in Pipelines," *Materials*, vol. 15, no. 13, Jul. 2022, doi: 10.3390/ma15134372.